TECHNISCHE UNIVERSITÄT MÜNCHEN

Wavelength Shifting and Photon Detection of Scintillation Light from Liquid Argon

Gabriela Rodrigues Araujo

supervised by Tina Pollmann and Stefan Schönert

Master's Thesis

E15: Chair for Experimental and Astroparticle Physics - Physics Department

March 2019

Abstract

Liquid argon (LAr) as a target medium in particle detectors has many desirable properties. Particles interacting in LAr cause flashes of VUV light, which has to be shifted to longer wavelengths before it can be detected by commercial photodetectors. This is achieved through the use of dedicated wavelength shifting materials, such as TPB. Other materials, usually not considered as sources of detectable photons, can also shift UV photons toward longer wavelengths. Acrylic (PMMA) and PTFE, which are commonly used in the cryostats that contain the LAr, have been reported to fluoresce or phosphoresce at a low-level when excited with UV light. In an experiment looking for rare events at low energies, this low-level photoluminescence can be a concern, since a small change to the amount or time structure of detected light can complicate the data analysis or even cause a background event.

In this thesis, I investigate the photoluminescence response of acrylic (PMMA) and PTFE to VUV and UV photons (from 130 nm to 380 nm). The investigated samples of these materials stem from running dark matter detectors, and their wavelength shifting efficiency (WLSE) is measured in comparison to that of TPB, which is extensively characterized in the literature. The photoluminescence response of these plastics to wavelengths below 220 nm is reported here for the first time. At the sensitivity of the setup used for this work, no photoluminescence was detected. Limits were set on the WLSE of these plastics, relative to TPB, at a level better than 1%. All samples were characterized at room temperature. Acrylic was additionally studied at the cryogenic temperatures the particle detectors have during operation. At these temperatures, WLSE limits were set at the level of 1%.

In this work, I also study the WLSE of the polymer PEN, which has been proposed as a replacement for TPB in upcoming experiments that use LAr. The WLSE of PEN is compared to that of TPB and the results suggest that pristine PEN presents over 50% of the efficiency of TPB in shifting VUV photons to the visible spectral range.

Acknowledgements

I would like to express my deepest gratitude to my thesis advisor Tina Pollmann. I am very grateful for her guidance, patience, motivation, and willingness to share her expertise. I am also grateful to Professor Stefan Schönert and professor Andreas Ulrich, who also advised me during this work.

I am thankful for the guidance I received at Queen's University from professor Philippe di Stefano and Peter Skensved.

I would like to thank the DEAP collaborators who helped me with useful information and discussions throughout this work.

I also would like to express my gratitude to professor Ivone Albuquerque from the University of São Paulo, who was my supervisor in the beginning of my master's studies, and to CAPES (Brazilian Higher Education Institution), which provided me with a scholarship from March 2017 until November 2017.

Finally, I would like to thank Tobi, for all his love and support.

Contents

Abstract **i**

Acknowledgements **ii**

0.1 List of Abbreviations vi

1 Introduction **1**
1.1 Overview 1
1.2 Dark matter: evidence and candidates 4
1.3 Neutrinos 9
1.4 Liquid Argon: properties, mechanisms of light emission, and scintillation photon detection 10
1.5 Liquid argon in dark matter and neutrino experiments 14
1.5.1 DUNE 14
1.5.2 GERDA 15
1.5.3 DEAP-3600 16
1.6 Nuisance photoluminescence in plastics and its impact on rare event search experiments 18

2 Photoluminescence response of acrylic (PMMA) and PTFE to UV light at room temperature **23**
2.1 Sensitivity goal 23
2.2 Samples 24
2.3 Measurements with VUV and middle-UV excitation light 26
2.3.1 Setup 27
2.3.2 Sources of background in fluorescence setups 29
2.3.3 Stability and calibration measurements 30
2.3.3.1 Stability of the excitation light and photodetector 30
2.3.3.2 Calibration of the spectral response of the Ocean Optics QE65000 spectrometer 32
2.3.3.3 Slit width and energy resolution 34
2.3.4 Procedures 34
2.3.5 Stray light and background fluorescence investigation 36
2.3.6 Data analysis and discussion 39
2.3.6.1 Spectrometer measurements 39
2.3.6.2 Wavelength-integrated measurements 40

2.3.7 Results: Upper limits on the wavelength shifting of acrylic and PTFE relative to TPB . . . 45
2.3.8 Conclusion . . . 47
2.4 Measurements of acrylic with UV light above 190 nm . . . 49
2.4.1 Setup . . . 49
2.4.2 Procedures . . . 49
2.4.2.1 Stray light and background fluorescence investigation . . . 51
2.4.2.2 Relation between slit width and light yield . . . 55
2.4.3 Data analysis and discussion . . . 56
2.4.3.1 Fluorescence emission spectra . . . 56
2.4.3.2 Relative photon yield . . . 61
2.4.4 Results . . . 63

3 Fluorescence response of acrylic (PMMA) to UV light at temperatures from 300 K to 4 K. 65
3.1 Setup . . . 65
3.2 Procedures . . . 68
3.2.1 Samples . . . 70
3.3 Data analysis . . . 71
3.3.1 Baseline noise investigation . . . 72
3.3.2 Integration window . . . 74
3.3.3 Relative photon yield . . . 76
3.4 Results . . . 81
3.5 Conclusion and discussion . . . 82

4 Relative wavelength shifting efficiency of polyethylene naphthalate 84
4.1 Samples . . . 85
4.2 Procedures and data analysis . . . 86
4.3 Results and discussion . . . 87
4.4 Conclusion . . . 89

5 Simulation of a setup for in-situ attenuation length measurements of LAr scintillation photons 91
5.1 Attenuation length: overview and literature . . . 91
5.2 TUM Liquid Argon Test Stand . . . 92
5.3 Selecting a source for attenuation length measurements in LAr . . . 94
5.3.1 Characterization of the americium source . . . 96
5.4 Triggered detection of scintillation light from liquid argon with an americium source . . . 96
5.4.1 Detection of scintillation photons from LAr with SiPMs . . . 98
5.4.2 Simulation of the production and detection of scintillation photons in LAr . . . 99
5.5 Summary . . . 105

6 Summary and outlook 106

A Appendix to the Chapter 2 109
A.1 Stability measurements and dead time estimation . . . 109

A.2 Calibration measurements and cross-checks 111

B Appendix to the Chapter 3 **113**
B.1 PMT and DAQ settings 113
B.2 Systematics, pulses and cuts 115

C Appendix to the Chapter 5 **120**
C.1 Americium source characterization 120
C.2 Active volume and threshold 128
C.3 Next Steps 130

Bibliography **131**

0.1 List of Abbreviations

AV acrylic vessel (here referring to the acrylic vessel of the DEAP-3600 experiment)

Bis-MSB 1,4-Bis(2-methylstyryl)benzene

BPC before plasma cleaning

LAr liquid argon

LG light guides (here referring to the acrylic light guides of the DEAP-3600 experiment)

LXe liquid xenon

MACHO massive compact halo object

PEN polyethylene naphthalate

PMMA Poly(methyl methacrylate)

PMT photomultiplier tube

PSD pulse shape discrimination

PTFE polytetrafluoroethylene

QE quantum efficiency

ROI Region of interest

RPT Reynolds Polymer Technology, the manufacturer of the AV type of acrylic

RT room temperature

SiPM silicon photomultiplier

TPB tetraphenyl butadiene

TPC time projection chamber

UV ultraviolet

UVA ultraviolet-absorbing

VUV vacuum ultraviolet

WIMP weakly interacting particles

WLSE wavelength shifting efficiency

WLS wavelength shifter

Chapter 1

Introduction

1.1 Overview

The night sky was our first window to the cosmos. Astronomers started gazing at the stars and classifying celestial objects millennia ago. With the advance of the telescope, they looked deeper into what seemed to be the darkness of the sky and found very distant galaxies, such as the one in Figure 1.1. As evidenced by this galaxy, we are now able to see the light emitted by far away objects billion of years ago.

FIGURE 1.1: GN-z11 is the most distant known galaxy, at a proper distance of 32 billion light-years and a light-travel distance of 13.39 Gly [1]. The light seen in this picture was emitted more than 13 billion years ago, when the universe was at its early stages. Credits: NASA/ESA/P.Oesch et al.

Telescopes advanced beyond visible light, reaching shorter and longer wavelengths and mapping our galaxy and the universe in different frequencies, as shown in Figure 1.2. These telescopes, operating across the electromagnetic spectrum, have given us a new view of the sky, but they have not allowed us to see everything that is out there in the universe: What

about the cosmic particles that do not interact through the electromagnetic force? For instance, billions of neutrinos go through our body each second and dark matter floods our galaxy. How can we observe them?

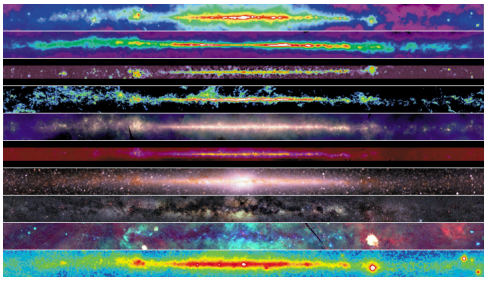

FIGURE 1.2: The milky way seen in different frequencies. From top to bottom: radio, infrared, optical, x-ray and gamma ray wavelengths. Figure from [2]. Credits: NASA/Mr. Jay Friedlander et al.

To detect the neutrinos, astrophysicists have developed state of the art detectors, which opened a new window to the sky: neutrino astronomy. By burying strings of photo detectors deep in the ice of the south pole, the neutrino observatory IceCube (Figure 1.3), for example, has defied common assumptions of how a telescope looks and has made great discoveries [3, 4]. Yet, the revolution of neutrino observatories and detectors has not solved the neutrino puzzle. We still do not know what type of particle the neutrino is[1]. Experiments that try to answer this question, such as the GERDA experiment, will be discussed later in this chapter.

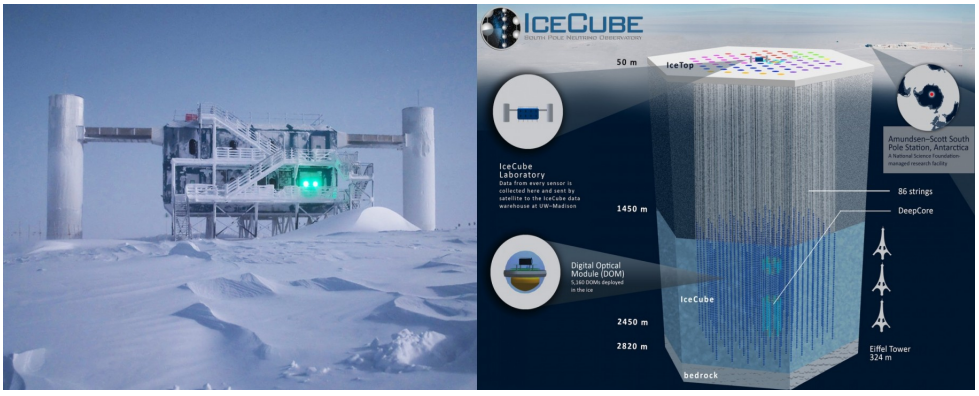

FIGURE 1.3: Left: Picture of the IceCube laboratory (E. Jacobi/NSF). Right: Full schematic of the IceCube Experiment, showing the laboratory at the top and the strings of photodetectors buried 1.5 km away from the top and covering 1 cubic kilometer of ice. (Figure from IceCube MasterClass)

What about the dark matter problem? Despite convincing evidence for the existence of dark matter, we still do not know its nature. There are many candidates and many experiments looking for them, especially for the weakly interacting massive particle (WIMP), but no detection has been made[2].

[1] It is not yet known if neutrinos are Majorana or Dirac particles.

[2] The DAMA/LIBRA experiment claims the detection of WIMPs [5] but other experiments [6] have already ruled out their results.

What is so special about these elusive particles and why is the hunt worthwhile? These particles together make up approximately 85% of the matter content of the universe, being therefore five times more abundant than the matter that makes up our bodies, the planets, and stars. That is, we have seen objects from the early time of our universe, such as the galaxy in Figure 1.1, but we still do not fully understand these million of particles that cross our bodies all the time.

Trying to understand and hunting these particles is not only exciting, but also challenging. The difficulty with detection lies in their weak interaction with other particles and in the background noise produced by other sources. In this thesis, I will focus on the light detection and background noise in dark matter experiments that use liquid noble gases, especially liquid argon (LAr), which is also used in neutrino detectors.

The working principle of these liquid noble gas detectors is comparable to fluorescent lamps. While the latter are filled with a gas[3] that is excited by an electric current, these detectors are filled with a liquid noble gas (usually xenon or argon), which is excited by particles colliding with it and causing a recoil. In both cases, as shown in Figure 1.4, the excitation produces ultraviolet light, which is later converted to visible light. In the lamp, the tube is coated with fluorescent powders that absorb the ultraviolet light and emit visible light. The same is true for a liquid argon detector: a fluorescent powder coating the detector shifts the ultraviolet scintillation light to longer wavelengths, so that it can be detected by commercial light detectors, such as photo multipliers tubes (PMTs) or silicon photo multipliers (SiPMs). We call these fluorescent powders wavelength shifters (WLSs). The investigation of the efficiency of the wavelength shifter polyethylene naphthalate (PEN) is one of the topics of this thesis.

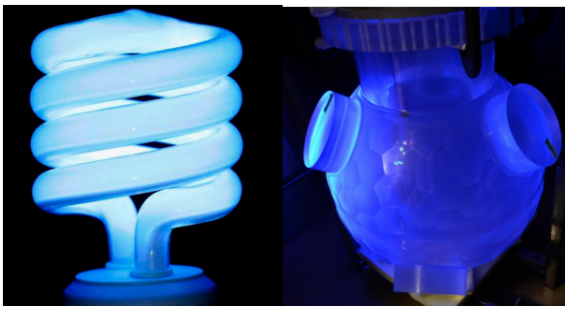

FIGURE 1.4: Left: Compact fluorescent lamp. Figure from [7]. Right: Small scale DEAP-test vessel coated with the wavelength shifter tetraphenyl butadiene (TPB) is lit with a 265 nm ultraviolet (non-visible) LED. Figure from [8].

Comparing these liquid noble gas detectors to fluorescent lamps makes the search for elusive particles seem easy, but it is a difficult task. WIMPs, for example, are expected to interact weakly with the target. Their expected interaction rate with liquid argon is very low, at the

[3] Usually mercury, argon, xenon, neon or krypton.

level of one interaction per year per ton of target material (depending on the WIMP's mass and cross section). These detectors must thus be very sensitive. This high sensitivity also has a drawback: they detect much more than the searched interaction. They detect particles coming from cosmic rays colliding with our atmosphere and also decays of radioactive elements in the target and surroundings. All these interactions are backgrounds to the dark matter signal.

Experiments deal with this background through shielding, vetoing, material screening, and event discrimination. Event discrimination is based on an analysis that classifies recorded events as signal or background based on event characteristics such as the distribution of detected light. In this thesis, acrylic and PTFE samples are tested for nuisance fluorescence that could lead to misclassification of events. These materials are commonly used in dark matter and neutrino experiments.

Another challenge of rare event search experiments is to detect the scintillation light from LAr (or from the corresponding target) efficiently. This involves not only the efficiency of the light detector (including the efficiency of WLSs, investigated in Chapter 4), but also the optical properties of the target, such as its transparency. Liquid argon itself is transparent to its light, but impurities can contribute to the attenuation of its photons, making the target medium less transparent to the light produced by the searched interactions. A draft of a setup (its source characterization and simulations) for the measurement of the attenuation length of liquid argon is presented in Chapter 5.

The next sections of this chapter discuss further the motivation for the search of dark matter and neutrinos, and present a broad view of the experiments that look for them.

1.2 Dark matter: evidence and candidates

The dark matter puzzle has been intriguing astrophysicists since the beginning of the last century. In 1933, the astrophysicist Fritz Zwicky inferred for the first time the existence of a massive type of matter that does not emit light. He used the virial theorem to calculate the mass of the Coma Cluster, then compared it to the mass inferred by its luminosity and found that there must be some non-visible matter to account for the difference in mass. He named this non-visible mass component "dark matter." Since then, there has been more evidence of its existence, such as the galaxy rotation curves, gravitational lensing, and the cosmic microwave background radiation. These observations showed that dark matter (DM) accounts for approximately 85% of the mass of galaxies and large structures. However, what type of matter is it?

Some theories try to explain the dark matter observations without introducing a new type of matter but rather with modifications in gravity. The best known of the modified gravity theories, the **modified Newtonian dynamics (MOND)**, has already been ruled out by the Bullet Cluster observation[4], which was the collision of two clusters [10]. In this collision, an offset between the luminous (visible and x-ray) matter peak and the mass peak inferred by gravitational lensing was observed. This offset could not be explained by MOND and provided further evidence for dark matter as a collisionless type of particle, putting limits on its self-interaction cross section [11].

Some other modified gravity theories were ruled out by the observations of both gravitational waves and the electromagnetic component of the merger of a binary neutron star [12]. These theories predicted a delay longer than the observed delay between the arrival of gravitational waves and photons [12].

Besides the modified gravity theories, another explanation to this "missing dark mass", which does not introduce a new type of particle, would be if dark matter was non-luminous or faint baryonic matter. Examples of non-luminous or faint objects are black holes, rogue planets and brown dwarfs. These objects make a class of dark matter candidates called **massive astrophysical compact halo objects (MACHOs)**, which can only make part of the dark matter content, since the search by the EROS experiment for gravitational lensing caused by MACHOs in the Magellanic clouds have put strong constraints on it [13]. However, these constraints (combined with other cosmological observations) had left a very small window in which a particular range of stellar-mass black holes were not excluded (see gap between dark blue and green line in Figure 1.5). After the detection of the merger of two $30M_{\odot}$ black holes by LIGO, the question as to whether dark matter could be composed of primordial black holes (PBHs) was raised again [14]. A search for these objects using the gravitational lensing of type Ia supernovae has recently constrained the possibility that PBHs make up more than 37.2% of the dark matter [15](Figure 1.5), ruling out PBHs and other MACHOs as the main dark matter candidates[5].

As baryonic matter has been most likely excluded as the dominant form of dark matter, astrophysicists are currently focusing on physics beyond the standard model and searching for non-baryonic candidates. These candidates present a wide range of masses (10^{-22} eV to 10^{15} GeV), as shown in Figure 1.6.

One of the lightest candidates are the **axions**, with a mass between 10^{-6} eV and 10^{-3} eV. These hypothetical particles result from a field that is introduced to explain the strong CP problem. The strong CP problem is the fine tuning necessary to explain why QCD does

[4]Some studies claim that MOND is able to explain observations of the Bullet Cluster [9].

[5]Some articles claim that these results do not fully rule out PBHs. Ref [16], for example, "[..] critically reviews these constraints and find several caveats on the analysis [of ref [15]]."

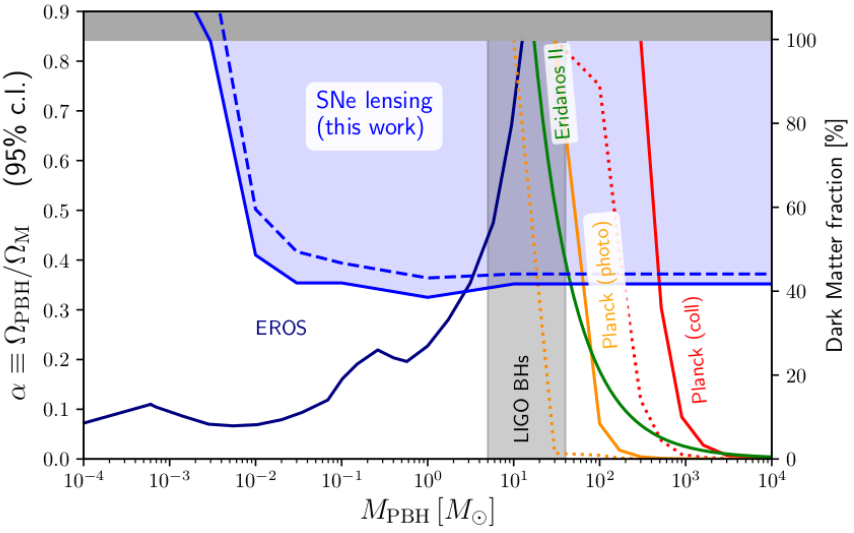

FIGURE 1.5: Figure from [15]: Limits on the abundance of PBHs relative to the dark matter content as a function of the mass (95% CL). The area in blue and dashed line shows the recent constraints set by [15], which closes the window that allowed for PBHs to account for DM. The dark blue line shows the limits set by the EROS experiment [13].

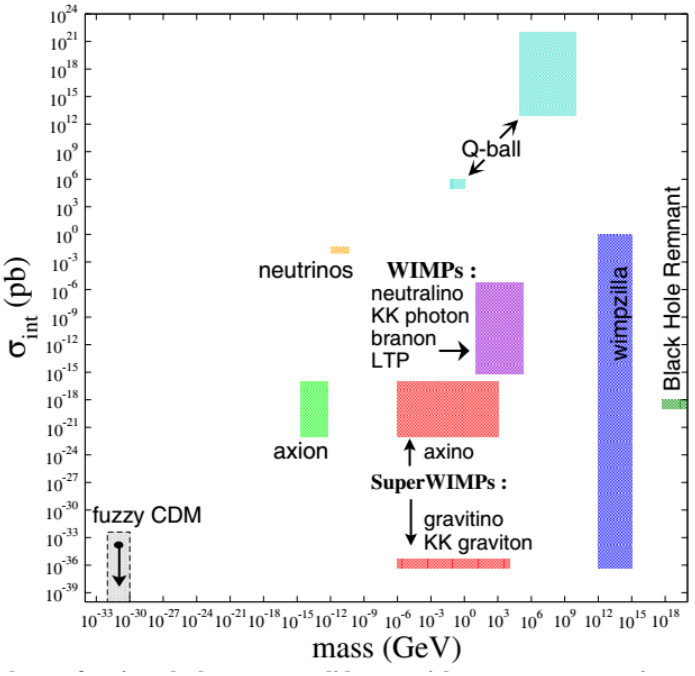

FIGURE 1.6: Parameter space (cross section in pb and mass in GeV) of some dark matter candidates. Figure from [17].

not violate CP-symmetry[6]. In order to make QCD non-CP-violating, its violating term would have to be abnormally small. The Peccei-Quinn mechanism was proposed to solve this problem by promoting the CP-violating term to a field, which can naturally relax to zero, explaining its small value. From this field arises the axion, which is a cold dark matter (CDM) candidate.

Even though axions are very light particles, they do not constitute what is called "hot dark matter"(HDM). HDM is excluded by large scale structure (LSS) observations, since fast-moving particles (hot) would smear out large structures rather than clumping, favoring an "upside down" scenario, in which big structures (such as galaxy clusters) form before smaller ones (such as galaxies).

Axions are, despite their lightness, slow-moving particles because they are not thermally produced, such as other DM candidates.

Neutrinos (the next in the mass scale in Figure 1.6), for example, are already ruled out because they would be hot dark matter. On the other hand, **sterile neutrinos** (hypothetical right-handed version of the neutrino) are still DM candidates, since they could be more massive than their left-handed counterparts. The heaviness of the sterile neutrino not only makes it a good dark matter candidate but it is also a natural way to explain the lightness of the active SM neutrinos through the seesaw mechanism.

Furthermore, sterile neutrinos in the keV range would constitute warm dark matter (WDM), solving the core cusp problem, which is the discrepancy between the simulated density profiles of CDM (cuspy) in dwarf galaxies and the observed density profiles (core). Another motivation for a keV sterile neutrino as a DM candidate is the 3.5 keV X-ray line observed by the XMM-Newton observatory [18], which might indicate the decay of sterile neutrinos. Figure 1.6 shows other candidates that could have mass in the keV range: **axinos** and **gravitinos**, which would be supersymmetric particles of the axions and gravitons.

The next candidate in this figure are the **weakly interacting massive particles (WIMPs)**. These particles have masses between approximately 100 GeV and 1 TeV and make a class of candidates that are expected to interact through the weak force. The popularity of the WIMPs as a DM candidate is because these particles are predicted in different theories (supersymmetry and extra dimensions) and just happen to be able to solve the dark matter puzzle. They could be the lightest supersymmetric particle or the lightest Kaluza-Klein particle and if they interact through the weak force, their abundance naturally agrees with the observed DM abundance. As CDM candidates, their properties agree with most of the dark matter observations.

[6]This non violation is observed in the lack of (or very tiny) electric dipole moment of the neutron.

WIMPs are CDM because they are slow moving particles, due to their large masses. WIMPs were theoretically produced in the early universe and were in a thermal bath together with other particles, being produced and annihilated. When the temperature dropped below the energy necessary to produce particle-antiparticle pairs of WIMPs, their production ceased, but their annihilation continued until its rate became lower than the expansion rate of the universe. This point in time is called freeze-out and the dark matter abundance remained approximately constant since then.

The search for dark matter (and especially WIMPs) is divided into direct, indirect and production. The null production of supersymmetric particles in the large hadron collider (LHC) and the null results from WIMP direct detection experiments have already set constraints on the parameter space of WIMPs and thus on their existence, as shown in Figure 1.7.

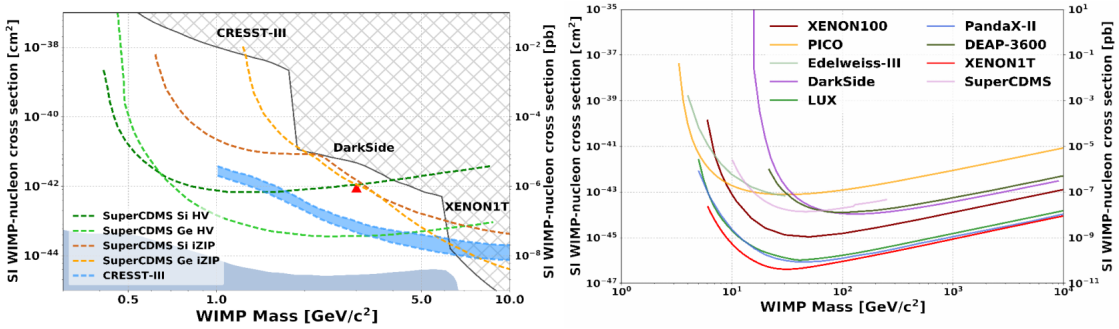

FIGURE 1.7: Recent results from dark matter direct detection experiments. Left: Limits on low mass dark matter. Right: limits on WIMPs. Figure from [19].

As current direct detection experiments have already excluded some expected mass and cross section values of WIMPs, they are expanding their search region and setting limits on "low-mass dark matter" (a few GeV) [20] and light dark matter (sub-GeV) [21, 22]. This mass range is motivated by some theoretical DM models, such as **asymmetric DM** [23], which relates the abundance of dark matter to the baryon-antibaryon asymmetry. This results in the mass of asymmetric dark matter being approximately 5 times the mass of the proton, that is, approximately 5 GeV.

Candidate particles more massive than WIMPs are **Q-balls** and **WIMPzillas**. Q-balls are hypothetical stable blobs of particles that, according to supersymmetric extensions of the SM, might have been produced in the early universe [24]. WIMPzillas are super-weakly interacting and superheavy particles which might have been produced by thermal freeze-in rather than freeze-out like normal WIMPs [25].

In this thesis, I will focus on experiments that use liquid argon and: i) aim the direct detection of WIMPs (some of which are also sensitive to few-GeV/sub-GeV dark matter) or ii) use LAr as main target or veto to investigate the nature of neutrinos. The motivation for neutrino detection is given in the next section.

1.3 Neutrinos

Neutrinos are particles with physical properties that are both a blessing and curse. As weakly interacting particles, neutrinos allow us to probe regions of the cosmos that we would otherwise not have access to. On the other hand, on their weak interaction lies also the challenge of their detection.

The first neutrinos were detected only some decades after their prediction. Then, there was a problem: The calculated flux from solar neutrinos did not agree with the observed one. The "solar neutrino problem" was solved only 4 decades later with the discovery of neutrino oscillation, which showed that neutrinos were not massless. This discovery implied physics beyond the standard model and excited the scientific community.

Currently, there is a large number of neutrino experiments (a list with more than 100 experiments is shown in [26]). Each experiment is designed to be sensitive to one (or more) flavors of neutrinos (ν_e, ν_μ, ν_τ) from different sources, such as from the sun [27, 28], reactors [28, 29], atmosphere [30], beamlines [31], supernovae [28, 29, 31] or from many sources combined. Some of the purposes of these experiments are to obtain the information about neutrinos' oscillation parameters [31], mass hierarchy [29], coherent scattering [32] and detect them as an early supernova warning [33]. Another less common proposed goal is their use for communication in "unusual circumstances", as demonstrated by [34].

The study and detection of neutrinos are important in many areas in physics and touch many of its unsolved problems. Neutrino astronomy, for instance, plays a key role in the understanding of dense regions in the universe and in multi-messenger astronomy, since neutrinos can easily penetrate very condensed regions and bring earlier (or additional) information about an event. With the help of neutrinos, we can now not only understand better the core of our sun [27] but also know where to look, in case a supernova happens in our galaxy, hours before the electromagnetic radiation from the event arrives on Earth. An example of a multi-messenger event involving neutrinos is the recent detection by IceCube of a high-energy neutrino from a blazar in coincidence with enhanced gamma-ray activity detected by Fermi LAT [3].

Neutrinos can also help us to understand physics beyond the standard model (BSM). Large beamline experiments, such as DUNE [31] (discussed in Subsection 1.5.1), aim to precisely measure some of the oscillations parameters, such as the neutrino mass hierarchy, mixing angles and CP violating phases, which may help us to understand the matter-antimatter asymmetry of the universe. Another open question related to neutrinos is whether they are their own antiparticles (known as Majorana particles) and differ from their anti counterparts only by their chirality. One experiment that aims to answer this question is the GERDA experiment [35], discussed in Subsection 1.5.2.

1.4 Liquid Argon: properties, mechanisms of light emission, and scintillation photon detection

Noble liquids are often used in rare event search experiments due to their scintillating properties. This scintillation combined with other techniques enables the measurement of the energy deposited by a particle in the scintillating target. The particle that interacts with the target producing scintillation and/or ionization can be: i) the searched rare event, such as the collision of a WIMP with the nucleus of the target or ii) radioactive decays and other background events, which can produce similar light signals in the detector.

Background discrimination through pulse shape analysis is a property of liquid argon that makes it more competitive in relation to other noble liquids. The discrimination between nuclear and electron recoils due to their different time profiles enables background discrimination in WIMP searches, for example.

WIMPs are expected to collide elastically at a very low rate[7] with the liquid argon nuclei of the detector. This type of interaction is called nuclear recoil because the nucleus of the target atom recoils after the collision. This interaction leads to both excitation and ionization of argon which can produce scintillation photons. The time profiles of the scintillation signal due to nuclear recoils is in general different than the one due to electron recoils, which are mainly caused by background events.

Most of the background events are electromagnetic: β and γ-decays, for instance. Since these particles collide with the electrons of the target atom, they lead to electron recoils.

In electron recoils, the energy of the electron or charged particle is transferred to other electrons. In nuclear recoils, the energy of the neutron or WIMP is lost to the recoiling of the nucleus of the target, which transfers its energy to other argon atoms nearby. This transferred energy goes either to the recoiling of other nuclei (which might dissipate their energy in heat) or to the excitation or ionization of other atoms, as shown in Figure 1.8.

The excited atoms (excitons) combine with other ground state atoms forming excited dimers (excimers) that emit scintillation photons when they deexcite. The ions can also combine with other ground state atoms and form ionized molecules. These ionized molecules can recombine with electrons and form excimers, similar to the one formed by excitons. These excited dimers undergo the same deexcitation process and emit scintillation photons.

There are two possible states for these excimers: a singlet and a triplet state. Each of them has a different decay time. The singlet state decays faster (6.7ns) than the triplet

[7]The expected collision rate depends on the WIMP mass and cross section, as shown in Figure 2 of [36].

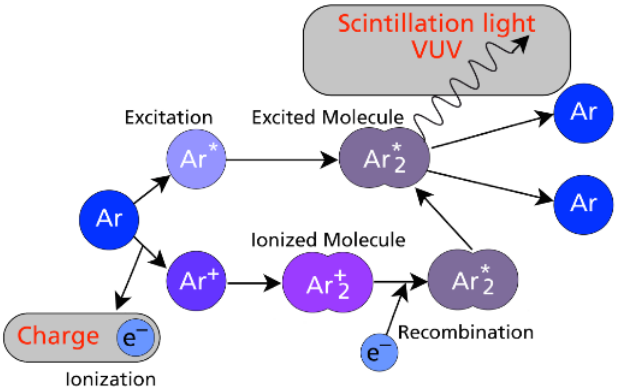

FIGURE 1.8: Scintillation and ionization mechanism of liquid argon. See text for more details. Figure from [37].

one (1500ns)[38]. The amount of singlet and triplet states is different for electron (ER) and nuclear recoils (NR).

Therefore, the time profile of the scintillation signal is different for NR and ER, as shown in Figure 1.9. This results in a pulse shape discrimination (PSD) power of the order of 10^8 [39]. In the DarkSide Experiment, a parameter called f_{90} is used as a pulse shape discriminator. This parameter represents the fraction of the signal that was detected within 90 ns. A background free WIMP search of DarkSide-50 using this PSD parameter is shown in Figure 1.10. In DEAP-3600, a similar parameter called F_{prompt} is used for pulse shape discrimination (PSD).

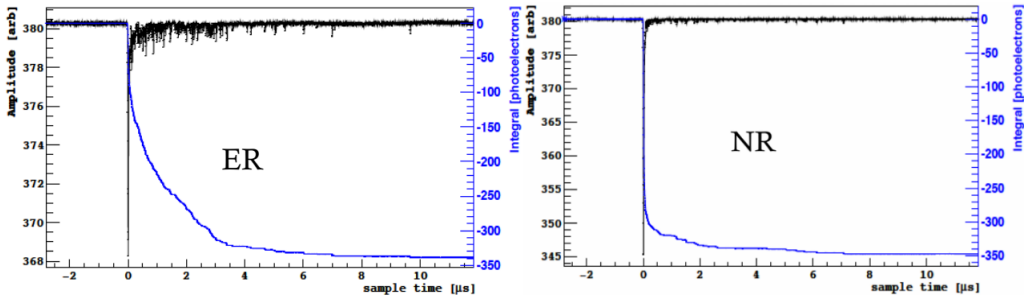

FIGURE 1.9: Sample time in microseconds versus amplitude and charge integral shown in blue. Figure adapted from [40]. There, referenced as [39].

PSD plays an important role in experiments that use LAr not only in the discrimination of external backgrounds (from the detector's surroundings, for instance), but mainly in the discrimination of decays of argon's radioactive isotope, ^{39}Ar. The radioactivity of ^{39}Ar and other properties of LAr are show in Table 1.1.

The wavelength of the scintillation light emitted by LAr is approximately 128 nm [42], which is in the vacuum ultraviolet (VUV) spectral region. Light in this wavelength range is not transmitted through common glasses. The glass of the windows of commercial PMTs, for instance, is opaque to 128 nm light. The photons from LAr scintillation must be thus shifted

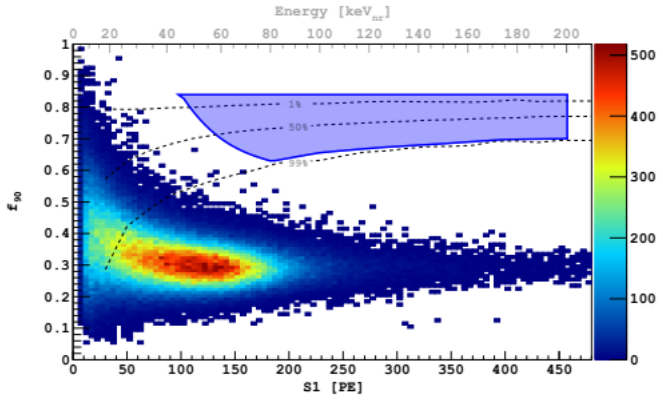

FIGURE 1.10: Number of photoelectrons from scintillation signal versus f_{90} discrimination parameter. Only electron recoils events are shown, since no nuclear recoil was observed in the region of interest. The dark matter search region is shown in blue. Figure from [41].

TABLE 1.1: Atomic, physical and optical properties of liquid argon

atomic and physical properties	main isotope	^{40}Ar
	atomic number	18
	melting point (at 1 atm)	83.81 K
	boiling point (at 1 atm)	87.3 K
	density (at b.p.)	1.3954 g/cm^3
optical properties	photon yield	40 ph/keV [38]
	emission wavelength	128 nm [42]
	attenuation length	50 cm [43], 66 cm [44], >110 cm [45]
radioactive isotopes	^{39}Ar	1 Bq/kg (atmospheric Ar) [46]
	^{85}Kr	6.5 mBq/kg (underground Ar) [47]
		approximately 10 $^{-1}$ Bq/kg [46]

to higher wavelengths, in order to go through the windows of the PMTs and be detected. For this purpose, the interface (glass window, acrylic vessel, etc) between the LAr target and the photo detector is coated with a wavelength shifter (WLS).

Wavelength shifters are compounds that absorb photons and re-emit them at an equal or larger wavelength. They are key elements in liquid argon experiments. Tetraphenyl Butadiene (TPB) is the WLS mostly used in LAr-based experiments [41, 48–53]. TPB presents a high quantum efficiency in converting VUV light into blue visible light [54, 55]. Figure 1.11-a shows the light emitted by LAr and the re-emission spectrum of TPB, which matches the acrylic transmittance of the DEAP acrylic vessel and the quantum efficiency of the DEAP PMT, shown in Figure 1.11-b.

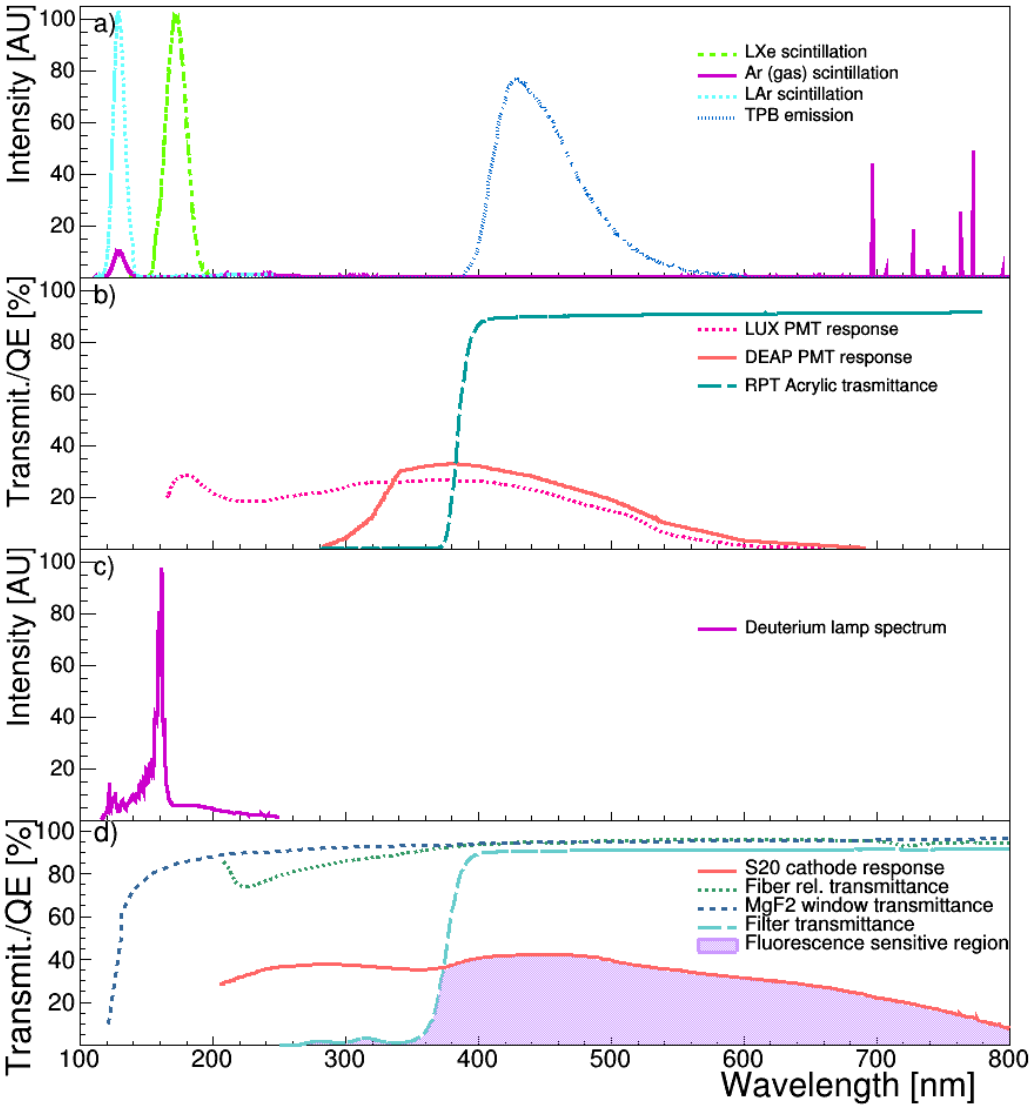

FIGURE 1.11: a) Emission spectra of: liquid xenon (LXe) [56], liquid argon (LAr) [42], Ar gas [42], and TPB. The emission spectrum of TPB was measured with the spectrometer described in Subsection 2.3.1 and is shown here without correction. The corrected spectrum is shown in Subsection 2.3.3.2. b) Quantum efficiency of the Hamamatsu R8778 PMT used in LUX [57]; quantum efficiency of the Hamamatsu R5912-HQE PMT used in DEAP-3600 [58] and transmittance of a 110 mm thick sample of RPT acrylic used in the acrylic vessel of DEAP [59]. c) Spectrum of the deuterium lamp used in the setup described in Subsection 2.3.1. d) Response of the S20 cathode of the PMT used in the same setup. Transmittance of: the optical fiber [60], the MgF_2 window of the PMT, and the acrylic filter. The transmittance of the lens is flat above 200 nm and is not shown here. Also shown is a shaded area to indicate the wavelength region the setup (Subsection 2.3.1) is sensitive to.

1.5 Liquid argon in dark matter and neutrino experiments

Because liquid argon has many advantageous properties, such as high photon yield (40 ph/keV [38]) and time structure allowing for pulse shape discrimination, several rare event search experiments use (or plan to use) LAr as the primary target, such as in ArDM [48], DarkSide [41], DEAP [58], MicroBooNE [50], ProtoDUNE [52] and DUNE [31]. Besides being used as the primary target, LAr can serve as a scintillator and shielding medium of a veto system, such as in GERDA [35].

LAr detectors are usually classified into: i) single-phase or dual-phase detectors, depending on whether only a liquid phase or also a gaseous phase of argon is used for detection; ii) time projection chambers (TPCs) or calorimeters, depending on whether the electrons from the ionization of the target are detected or only scintillation is detected.

In TPCs, the electrons from the ionization of LAr are drifted by a strong electric field before they recombine. These electrons produce a second (late) signal. This signal allows for a better position reconstruction, additional background discrimination and the possibility to search for low-mass or sub-GeV dark matter (in addition to common WIMPs). The disadvantage of a TPC is that they need high voltage for the electric field. The DarkSide-20K, which is the future LAr-based experiment of the joint collaboration of DarkSide-50 and DEAP-3600, will be a dual-phase TPC.

TPCs can also be single-phase, such as in Icarus or MicroBooNE [50]. The ProtoDUNE experiment includes both single-phase and double-phase LAr detectors as testing and development for the DUNE experiment, which is described below.

1.5.1 DUNE

DUNE is the Deep Underground Neutrino Experiment planned to be constructed in the U.S. by a collaboration from 30 countries. DUNE will be composed of two neutrino detectors: a near one, located close to the neutrino source at Fermilab, and a very large far detector, which will receive a beam of neutrinos 1300 km away from Fermilab. These detectors, with a total mass of approximately 70k ton of LAr, will be the largest LAr detectors ever constructed. The construction of DUNE involves not only the effort of building the far and near detectors, but also of upgrading the accelerator of Fermilab, to produce the "world's highest-intensity neutrino beam" [31].

The physical goals of DUNE are to study neutrinos and proton decays. The detectors will be LAr TPCs, which will detect the electrons and VUV scintillation produced by an event in liquid argon. The VUV scintillation detection design is still under development. The

characterization of a possible WLS for the VUV light detection in DUNE was done as part of this thesis and is described in Chapter 4.

1.5.2 GERDA

The Germanium Detector Array (GERDA) is an experiment located at the Gran Sasso National Laboratory (LNGS) that searches for a signal from neutrinoless double beta decay ($0\nu\beta\beta$) of the isotope ^{76}Ge. The observation (or non-observation) of neutrinoless double beta decay is crucial in understanding whether neutrinos are Majorana particles and if lepton number violation occurs. If neutrinos are Majorana particles, their masses can be naturally explained through the seesaw mechanism. Furthermore, lepton number violation could explain the observed matter-antimatter asymmetry.

The advantage of searching for ($0\nu\beta\beta$) in germanium is that both detector and medium are the same. Another advantage of germanium detectors is their good energy resolution, which enables enhanced background suppression. The germanium crystals must be, however, enriched: The detectors used in the phase II of GERDA were enriched from 7.8% to approximately 87% [35].

GERDA (phase II) presented recently a background free search [35]. The experiment claims to be the first ($0\nu\beta\beta$) experiment "that will be background-free up to its design exposure." In addition to the background suppression due to its good energy resolution, GERDA relies on both pulse shape discrimination and a veto system to suppress background. The veto system and the germanium crystals inside it are shown in Figure 1.12. The veto and the assembly of the detectors are described below.

The germanium detectors make an array of seven strings individually covered by nylon and immersed in liquid argon, which is used as a both passive and active veto[8]: The LAr volume shields the detectors from decays happening on the walls of the cryostat and LAr scintillates when a particle has enough energy to excite it. This scintillation light is detected by two light detection systems that form a cylindrical volume around the array (shown in Figure 1.12): i) a curtain of wavelength shifting fibers coupled to silicon photomultipliers (SiPMs) and ii) PMTS placed at the top and bottom of the cylindrical volume[9].

Both light detection systems are coated with TPB to shift the VUV light from LAr to the visible region; also the nylon covers are coated. If a particle produces a signal in both crystals and LAr, the event is vetoed, since a neutrinoless double beta decay should create a signal only in the crystals. The expected signal is a monoenergetic peak at 2039 keV [35].

[8] In addition to cooling the detectors to their working temperature, below 87 K.

[9] The PMTs are placed a bit further away so that their radioactive decays do not reach the crystals.

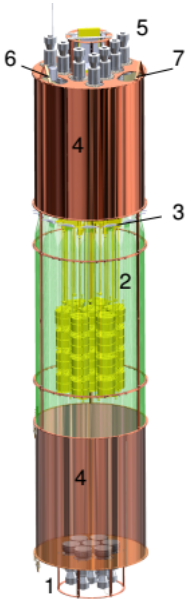

FIGURE 1.12: LAr veto system from the GERDA experiment. The numbers indicate: (1) the PMTs, (2) the wavelength shifting fibers, (3) the SiPMs, (4) two thin copper cylinders (with their inner surface covered by reflectors), and (6-7) two slots for calibration sources. Figure from [35].

In this thesis, a material for improvements in vetoing and wavelength shifting in GERDA (as proposed by [61]) or LEGEND was investigated in Chapter 4. Furthermore, a draft of a setup (its source characterization and simulations) for the measurement of the attenuation length of liquid argon in the test stand at TUM (used for tests for GERDA) is presented in Chapter 5.

1.5.3 DEAP-3600

DEAP-3600 is a single-phase liquid argon detector located approximately 2 km underground at SNOLAB. The experiment was designed to detect the spin-independent scattering of WIMPs on argon nucleons with a cross section sensitivity of $10^{-46}\,\mathrm{cm}^2$ (projected sensitivity for a $100\,\mathrm{GeV/c}^2$ WIMP mass with an exposure of 3 tonne-years [58]). DEAP stands for "Dark matter Experiment using Argon Pulseshape discrimination". In DEAP, WIMPs are expected to interact with the LAr target and produce a nuclear recoil signal, which can be discriminated from other background events by the pulse shape discriminator F_{prompt} described in Section 1.4.

The DEAP detector currently contains approximately 3300 kg of liquid argon inside a spherical acrylic cryostat. The spherical acrylic vessel (AV) is shown during construction in Figure 1.13. Its inner surface was sanded and coated with TPB to shift the VUV scintillation

light from liquid argon to the blue spectral region (similarly to the prototype shown in Figure 1.4). The wavelengths involved are shown in Figure 1.11-a. The neck, which gives access to the inside of the cryostat, was not coated with TPB.

FIGURE 1.13: Left: Spherical acrylic vessel (85 cm of diameter and 5 cm thick). Right: 45-cm-long cylindrical light guides attached to the acrylic vessel.)

Cylindrical acrylic light guides (LG) are attached to the spherical AV (as shown in Figure 1.13). These 45-cm-long LGs give the 255 PMTs access to viewing the target. The LGs were produced by Spartech and its acrylic was chosen by its superior transmittance. The AV was produced by Reynolds Polymer Technologies (RPT) from custom made ultra-low-radioactivity acrylic. The acrylic (poly(methyl methacrylate), also known as PMMA) used in both LGs and AV is of type UVA (ultraviolet absorbing). The transmittance of the RPT acrylic used in the AV is shown in Figure 1.11-b, together with the quantum efficiency (QE) of the Hamamatsu R5912-HQE PMTs used in DEAP. In this figure, we see that most of the light wavelength shifted by the TPB can be transmitted through the acrylic, but none of the light emitted directly by liquid argon can be transmitted.

Figure 1.14 shows a cross section of the experiment. The acrylic vessel, light guides, the PMTs that look the target and neck veto are shown inside the steel shell, which is inside a water tank used as muon veto (not shown in the figure). The approximately 3300 kg of LAr is shown inside the spherical part of the AV, which is coated with TPB. The acrylic flow guides that cool the LAr are shown inside the neck. Both the flow guides and neck are not coated with TPB. Since the AV is not completely filled with LAr, the bare acrylic of the neck and flow guides are in contact with argon gas and droplets of argon that condensates on their surface.

Watching the detector's target through an acrylic vessel had already been proven to be successful by the Sudbury Neutrino Observatory (SNO) Experiment [62]. One of the greatest advantages of acrylic lies on the combination of its optical and thermal properties: After

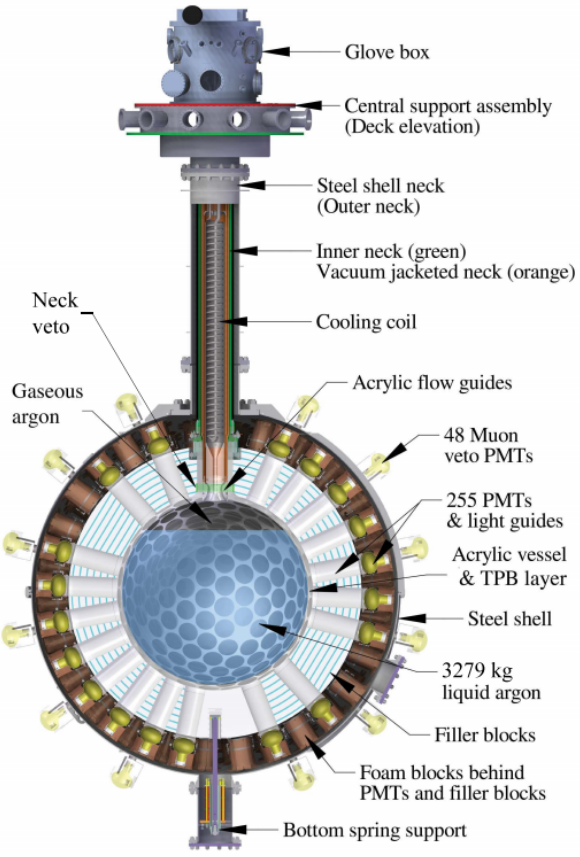

FIGURE 1.14: Cross section of the DEAP-3600 detector components. Figure from [49].

approximately 50 cm of acrylic, the combined transmittance of the LGs and the AV is still above 90% and the thermal gradient is large enough to enable the operation of the PMTs at approximately 270 K [58], while the inner part of the cryostat is at LAr temperature. Furthermore, acrylic is a good neutron shield and can be produced with high radiopurity levels [58].

One drawback of acrylic is Cherenkov light being produced in it. To minimize the amount of this light seen by the PMTs, the type of acrylic chosen was the UVA one, which contains additives to absorb UV light. The main focus of this thesis is to investigate whether this additive or any other additives or impurities in the acrylic used in DEAP fluoresce when excited by UV light.

1.6 Nuisance photoluminescence in plastics and its impact on rare event search experiments

Many rare event search experiments surround their scintillating target with plastics, such as acrylic (PMMA) [58, 62, 63] or polytetrafluoroethylene (PTFE) [41, 48, 64, 65], materials that

have been reported to photoluminesce at a low level when excited by UV or visible light [66–75, 75–81]. This nuisance photoluminescence[10] was described as background fluorescence in different contexts [66, 67, 71, 72] and has become now a concern in dark matter experiments.

In the DEAP detector, the fluorescence of acrylic would mainly affect two types of events that produce UV light: i) radioactive decays that happen in droplets of LAr on the inner surface of the neck, which produce VUV light that reaches the bare (without TPB coating) acrylic of the neck and ii) Cherenkov light (UV-Vis) produced in acrylic by particles from radioactive decays in or close to the AV and LGs.

In both cases, there is some evidence that acrylic is wavelength shifting some of this UV light to the visible range. For instance, the neck veto of the AV (shown in Figure 1.15) is triggered more than expected from simulation (since the neck is not coated with TPB[11]) .

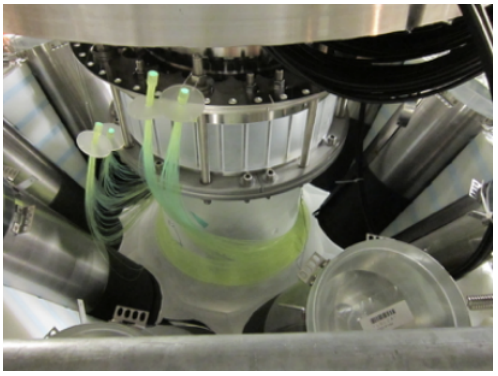

FIGURE 1.15: The neck veto wavelength shifting fibers are shown surrounding the AV neck before being coupled to R7600-300 PMTs and covered by filler blocks. Figure from [58].

One way to explain this excess would be if acrylic shifted some of the VUV scintillation light (produced by decays in droplets of LAr in the neck) to a wavelength range where the acrylic is transparent, so that the light could reach the neck veto.

Another example is the energy spectrum of Cherenkov events in the acrylic. The observed spectrum is shifted to higher energies than predicted by simulation, indicating that more of the Cherenkov spectrum is visible to the PMTs than expected. If acrylic fluoresces, it could shift part of the non visible Cherenkov light to the visible range. The Cherenkov spectra produced in acrylic by electrons with energies from 200 keV to 300 keV was calculated by [75] and is show in Figure 1.16.

[10] Photoluminescence is classified as fluorescence or phosphorescence, depending on the types of the excited states (singlet or triplet), which have different time decays (short - ns scale - or long).

[11] The neck veto was originally designed to tag events that happen in the neck and that could have a degraded light collection due to the geometry of the neck. However, the neck was not coated with TPB. Instead, the geometry of the flow guides inside the neck was optimized so that the reconstruction of alpha decays in the neck was out of the region of interest for the WIMP search. The neck veto is therefore currently used to veto Cherenkov events that happen in the neck and have a visible light component

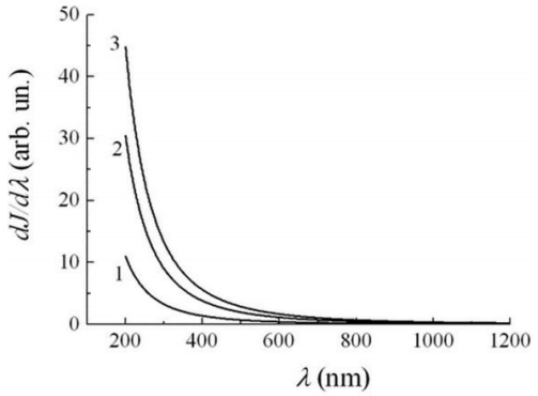

FIGURE 1.16: Calculated Cherenkov spectra in acrylic for electrons with energies from 200 (1), 250 (2) and 300 (3) keV. Figure from [75].

Only a small part of the Cherenkov light yield is in the visible region. This means that a small wavelength shift from the UV to the visible range could increase significantly the amount of the light yield in the DEAP sensitive region, shown in Figure 1.11-b.

The wavelength shifting of Cherenkov and UV light produced in acrylic has recently been reported by [75]. The authors investigated the luminescence of acrylic in the context of Cherenkov detectors for use in Tokamaks. They excited acrylic samples with both a run-away electron beam and a KrCl excilamp (222 nm light). In both cases, the UVA acrylic samples emitted blue light. The emission spectra presented two components: one peaked at approximately 400 nm and the other one at 490 nm.

To the best of my knowledge, no paper has reported the photoluminescence response of acrylic (or of PTFE) to wavelengths shorter than 222 nm (used in Ref. [75]). That is, the photoluminescence response of acrylic and PTFE to vacuum ultraviolet light (VUV), which is relevant for liquid noble experiments, has not yet been described in the literature. There is, however, a large number of papers that investigated the fluorescence of acrylic when excited by long-wave UV or visible light [66–73] (at room temperature).

In [66–72], they measured the fluorescence response of PMMA in order to determine which materials are most suitable for electrophoresis chips and chips for other lab devices. These papers refer to the fluorescence of PMMA as either autofluorescence or background fluorescence and compare it to the fluorescence of borosilicate glass (microscope slides or BoroFloat) or fused silica microscope slides. These glasses are used as references due to their low fluorescence background.

References [66, 67] show that PMMA autofluoresces more than the glass reference sample and that it is one of the less florescent plastics among the investigated ones. Reference [69] measured the fluorescence emission of PMMA excited by a 532 nm laser. The spectrum peaks at 630 nm and they were not sensitive to wavelengths lower than 600 nm. References [71, 72]

show that the autofluorescence of PMMA is comparable to the one of a glass microscope control. In [73], the authors measured the emission spectrum of pure PMMA for an excitation wavelength of 355 nm. The emission spectrum peaked at 450 nm.

The plethora of literature indicating the fluorescence of PMMA motivates the question whether the acrylic used in the vessel and light guides in DEAP fluoresces or not. No claim can be made based on literature data, though. Different manufacturers may use different processes to produce PMMA acrylic and this might result in different levels of fluorescence [67]. Reference [72], for instance, measured different levels of background fluorescence of acrylic within the same class of acrylic (same monomer unit PMMA). The authors stated that fluorescent plastics (polymers) usually have aromatic or double bonds conjugated structures, since fluorescence light is usually emitted as a result of $\pi \rightarrow \pi^*$ energy transitions. This means that polymers like ABS and PETG are expected to fluoresce more than PMMA, which has no aromatic structure or conjugated double bonds [72], as show in Figure 1.17.

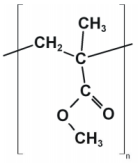

PMMA

FIGURE 1.17: Molecular structure of PMMA. Figure from [82]

Since the polymer matrix of PMMA is not supposed to fluoresce like other plastics, the fluorescence of acrylic could be due to impurities, additives, lab processes, defects, color centers, and surface contaminants. In order to understand the origin of fluorescence in acrylic, we can consider the fluorescence of optical glasses: Reference [83] states that "the fluorescence in optical glass is generated by point defects like color centers, which are known to be originated by rare earth elements, and certain impurities".

Color centers have been known to be produced in glasses by radiation damage [84]. The same is true for acrylic irradiated with ultrashort laser pulses [85]. Reference [85] shows that the color centers formed in acrylic (after exposure to ultrashort laser pulses) emit a broad spectrum of light (from 420 nm to 650 nm) when excited by a 443 nm laser. As the energy calibration of the DEAP detector is done with a pulsed LED and radioactive sources, it is important to determine if they could lead to color center production in the acrylic of the AV and LGs. If so, it is also necessary to understand whether these color centers could fluoresce enough to affect the light collected in DEAP. Data analysis of the number of events

triggering the neck veto before and after calibrations is still ongoing[12] and will try to answer this question.

The investigation of PTFE photoluminescence was done in the context of the Large Underground Xenon (LUX) dark matter experiment. The LUX detector is a TPC double-phase detector filled with liquid xenon (LXe). The inner part of the TPC is lined with PTFE panels. The PTFE used is type 8764 by Technetics [86]. The LXe scintillation photons (shown in Figure 1.11-a) are detected directly by VUV-sensitive PMTs immersed in the LXe (the PMT response function is shown in the same figure, in b).

The delayed photoluminescence of PTFE in liquid xenon detectors has been proposed by [87] as a way to explain the slower component of the "electron train" observed in XENON10 and ZEPLIN-III [87]. Reference [87] states that this slow component could be a background in the low-energy analysis of XENON1T and LUX experiments. The LUX detector also observed certain phenomena in the detector that could be attributed to the fluorescence of PTFE [88]. Furthermore, fluorescence or phosphorescence of PTFE has been observed by [76–81, 89]. If PTFE phosphoresces, that is, if it re-emits delayed light, this could complicate the analysis of noble liquid experiments that use PTFE, since the delay in the re-emitted light can make its correlation to the original event more difficult.

In this context, the main goal of this thesis is to test the photoluminescence of these plastics (PMMA and PTFE), with focus on the batches used in the DEAP and LUX experiments.

[12] As the analysis is still ongoing, no section of this thesis was dedicated for describing it.

Chapter 2

Photoluminescence response of acrylic (PMMA) and PTFE to UV light at room temperature

The objective of these measurements is to determine whether the acrylic (PMMA) and PTFE used in DEAP and LUX, respectively, shift UV light to the visible range (at RT) to the degree that it becomes an issue in these experiments.

2.1 Sensitivity goal

To create a background in the DEAP detector, the fluorescence of acrylic must be able to generate events in the energy region of interest (ROI). The events with the highest number of photons in the detector are alpha decays in the LAr, so even if the wavelength shifting efficiency of acrylic is very low, enough visible light could be created to place the event in the ROI. The energy ROI goes up to approximately 100 keV. If an 8.8-MeV alpha decay happens in a droplet of LAr in the neck of the AV, and if all the VUV light is shifted by acrylic (rather than by TPB), the wavelength shifting efficiency of acrylic must be on the order of 0.1/8.8 MeV (approximately 1%) relative to that of TPB to move this event into the ROI.

Therefore, the main goal of these measurements is to test, at room temperature (RT), the response of PMMA and PTFE to VUV light at the level of 1% (or less) of the fluorescence yield of TPB. This sensitivity target is also extended to the response to near and middle UV, since these plastics could also shift Cherenkov light, as discussed in Section 1.6. To quantify and set limits on the wavelength shifting efficiency of the specific batches of acrylic and PTFE, their light yield is compared to the fluorescence yield of a TPB sample.

2.2 Samples

As discussed in Section 1.6, even if the polymeric matrix of a plastic is not expected to fluoresce, a sample can still present a low level of photoluminescence due to impurities, additives, lab processes, defects, color centers and surface contaminants [67, 72, 79, 90]. Since the UV light does not penetrate far into the material, surface contamination can have a significant influence on the fluorescence measurement. Many common contaminants, such as oil from fingerprints, can fluoresce [91]. The investigated samples were therefore obtained out of the same batches used in the detectors, and cleaned using the same procedures. The measured samples and their cleaning procedures are described in this section.

Investigated samples:

- RPT acrylic: RPT stands for Reynolds Polymer Technologies, the manufacturer of this UVA acrylic (PMMA). The sample was cut from the same acrylic batch used to form the acrylic vessel of DEAP (shown in Figure 1.13). Samples with different surface finishings were tested and are listed below.
  - smooth: The surface was polished to optical quality and then cleaned by ultrasonic cleaning in ultra-pure water with Alconox detergent, followed by ultrasonic cleaning in just ultra-pure water. The fluorescence response was measured, then the samples were cleaned again in the following way: ultrasonical bath in distilled water with industrial detergent, then in distilled water, then air plasma cleaned.

  - rough: One of the clean smooth samples of RPT acrylic was sanded with the same sandpaper used in the resurfacing of the AV of DEAP. Both smooth and sanded samples are shown in Figure 2.1.
  - with bond: A rectangular prism piece of RPT acrylic with the same bond used to join the parts of the acrylic vessel of DEAP. This bond also consisted of PMMA. This sample has a different geometry than the RPT smooth and rough.

- Spartech acrylic: This acrylic is also type UVA and is produced by Spartech. This sample stems from the same acrylic batch from which the DEAP light guides are made (shown in Figure 1.13).
  - smooth: The surface polishing and cleaning procedures were the same used for the smooth RPT acrylic.
  - rough: Sanded Spartech acrylic using the same procedures described for RPT acrylic rough.
  - with bond: A rectangular prism piece of Spartech acrylic. See description of RPT with bond for more details.

- Sandpaper: A piece from the same batch of sandpaper used in the resurfacing of the AV of DEAP and also used to sand the samples investigated here.

- SNO acrylic: An acrylic sample from the vessel of the SNO experiment.

- PTFE: This PTFE is type 8764 of Technetics [86] and the sample stems from the same batch of material used in the reflector panels of LUX (shown in Figure 1.13). The sample was cleaned with pure acetone in an ultrasonic bath and then kept under vacuum for one day. The sample can be seen in Figure 2.4.

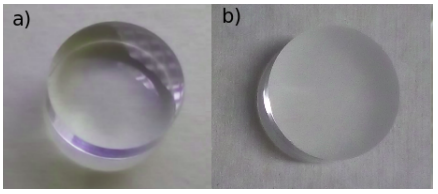

FIGURE 2.1: a) sample of RPT (UVA) acrylic (smooth). b) Sanded (rough) sample of RPT acrylic.

Reference samples

- TPB: A layer of TPB vacuum evaporated on glass. The glass used as the substrate was sonicated in isopropanol and dried with a nitrogen gun. The thickness of the sample was determined using a test sample (evaporated together with the original sample) and a profilometer. The thickness value is the average of three measurements done with the profilometer. The TPB sample is shown in Figure 2.2. The TPB thickness of the first sample (sample 1) was 1.93±0.03 µm. To ensure that the measurements were always done in comparison to a pristine TPB sample, a second sample with a 1.2±0.2 µm thick layer of TPB was later evaporated on glass (sample 2).

- Aluminium plate: This sample was cleaned in a plasma cleaner in order to remove surface impurities and oils that could fluoresce. This sample was measured before and after being plasma cleaned.

- Glass plate: Borosilicate microscope slide glass. This sample was sonicated in acetone and dried with a nitrogen gun.

- Stock acrylic: This sample was sonicated in isopropanol and dried with a nitrogen gun.

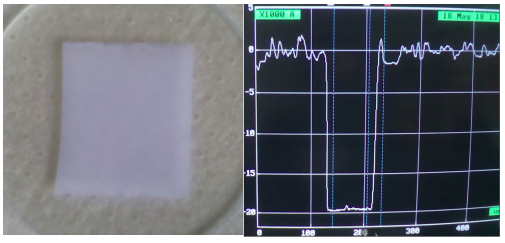

FIGURE 2.2: Left: A layer of TPB vacuum evaporated on glass. Right: Measurement of the thickness of TPB using a profilometer.

2.3 Measurements with VUV and middle-UV excitation light

If acrylic or PTFE fluoresces, its fluorescence level is expected to be low and commercial fluorescence setups are usually not sensitive enough to detect it. Furthermore, most of these devices do not provide VUV excitation light. The challenge in VUV measurements is due to the following factors: i) the vacuum level along the optical paths must be below 10^{-3} mbar, therefore optical components must be vacuum compatible, ii) all the optical components must transmit VUV light, which is absorbed by standard optical parts, iii) since the VUV light is

not visible to the human eye, alignment of components can be more difficult. Therefore, a VUV fluorescence setup was optimized for measuring low-intensity fluorescence in order to reach the target sensitivity. This setup is described in the next subsection.

2.3.1 Setup

The idea of this setup is to excite the samples with VUV to far UV light and measure the fluorescence response in the range from 360 nm to 800 nm, as shown in the "fluorescence sensitive region" of Figure 1.11-d. The fluorescence measurement setup is shown in Figure 2.3. It consists of a Cathodeon deuterium lamp, a VM-502 vacuum monochromator, a sample holder, and a light detection assembly.

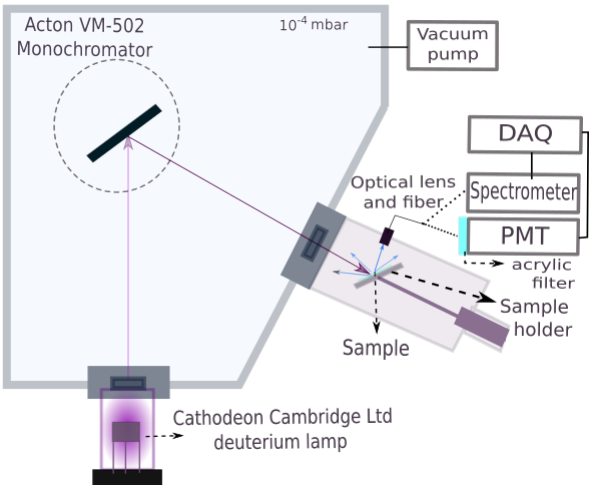

FIGURE 2.3: Scheme of the fluorescence measurement setup. Light from the deuterium lamp is directed through an entrance slit toward the monochromator, which reflects the desired wavelength toward an adjustable exit slit and onto the sample. An optical lens observes the sample and the optical fiber guides the photons to the photodetectors. The whole system is under vacuum.

The flange and sample holder were designed to maximize the light detection efficiency. The sample holder, shown in Figure 2.4, was built to accommodate the different dimensions of the samples[1] in such a way that the illuminated area on the surface of each sample was at the same position relative to the incoming beam and the lens. The sample holder head is adjustable such that the incidence angle can be varied. An adapter made of black plastic was placed behind the samples (without changing the relative geometry) in order to suppress the

[1] except for the rectangular prism samples. For these samples, an extra adapter was built.

light transmitted through the TPB and acrylic samples to be back-reflected by the aluminium sample-holder surface.

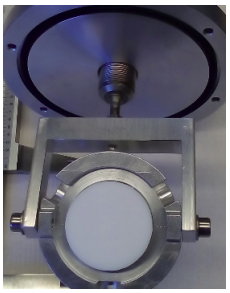

FIGURE 2.4: The PTFE sample placed in the movable sample holder.

The monochromator chamber is connected to a vacuum system composed of a prepump and a turbomolecular pump. A pressure gauge is connected to the monochromator chamber at the end of a tube. The gauge was installed in such a way that light possibly generated by it was unlikely to reach the sample. A pressure down to 10^{-5} mbar could be reached. The typical operating pressure was 10^{-4} mbar.

The cathodeon deuterium lamp provides light from 112 nm to 400 nm. The spectrum up to 250 nm is shown in Figure 1.11-c. The monochromator is used to select a specific wavelength from this spectrum and to guide it into the sample through an exit slit. The impact point of the photon beam on the sample is observed by a lens. If a sample fluoresces when excited by the incident light, part of the emitted photons will be collected by the optical lens. If their wavelengths match the transmittance of the fiber (shown in Figure 1.11-d), they are then transmitted through an optical fiber toward the light detector.

Two exchangeable photon detectors are in the light detection assembly: i) a QE65000 Ocean Optics spectrometer, and ii) a PMT with an S20 cathode. A thin acrylic window is used in front of the PMT to absorb light from reflections of the excitation beam. The PMT was operated in photon-counting mode. Figure 1.11-d shows the transmission and detection efficiencies of the components in the setup as a function of wavelength. The shaded area shows the fluorescence sensitive region of the setup.

The data aquisition system (DAQ) depends on the photodetector being used. The Spectra-Suite software from Ocean Optics was used to acquire the data from the spectrometer at a resolution of approximately 0.8 nm [92]. The data acquisition for the PMT consisted of

a Canberra 2128 constant fraction discriminator connected to a Wenzel Elektronik counter which outputs the number of pulses above the threshold.

2.3.2 Sources of background in fluorescence setups

When measuring low levels of fluorescence, stray light and fluorescence of components in the setup, other than the sample to be measured, can pose a strong constraint on how well the low level of fluorescence can be measured. One of the sources of stray light comes from the monochromator. Monochromators are known to transmit a small amount of light outside their narrow nominal bandwidth at a level of typically 0.1% of the transmittance of the narrow selected band [93]. In diffraction grating monochromators, this stray light usually arises from imperfections of the grating.

Stray light from the monochromator can be avoided by using filters. However, filters can also fluoresce at a low-level. Background fluorescence of filters is a source of noise in fluorescence microscopy [94], for instance. Another source of background fluorescence are the optical components of the light detection assembly, such as the optical lens and fiber. The low-level fluorescence of optical glasses is a known source of background in optical devices [83, 95]

If the setup has no room light immunity, background light can also add to the noise in the setup. This background light can be ambient light that reaches the optical components of the setup or devices that produce light inside the setup. In contrast to the aforementioned sources of noise, the background light can be easily dealt with[2] by taking a dark (background) measurement, which can be later subtracted from the total light yield in the measurement of a sample.

To check for stray light and sources of fluorescence other than from the sample, an investigation of stray light and background fluorescence was done for each set of measurements (Subsection 2.3.5 and Subsection 2.4.2.1).

[2] Assuming its level is low and constant.

2.3.3 Stability and calibration measurements

In this section, the systematic errors and the stability of the setup will be discussed, the energy resolution of the excitation light and the wavelength-dependent response of the spectrometer will be measured, and a correction for the spectra will be derived.

2.3.3.1 Stability of the excitation light and photodetector

PMTs have a dark count rate due to thermionic release of photoelectrons from the photocathode. This rate depends on the temperature of the PMT and on the bias voltage applied, as well as on the time since the PMT was turned on. To guarantee that the dark rate of the PMT is stable during the time of one run of measurements, the dependence of the dark rate of the PMT on time was measured. The details of the measurements are described in Appendix A, Section A.1. These measurements show that the PMT is stable within minutes after being turned on. Nevertheless, the warm-up time of the PMT was defined as one hour and a systematic error of the dark rate, σ_{syst}^{DR}=10%, was derived from the stability measurements, in order to conservatively account for any possible systematic effects.

The stability of the lamp and of the TPB sample were also investigated (see Section A.1 for more details). The lamp was found to be stable after 40 min. A systematic error of the intensity of the lamp, σ_{syst}^{Lamp}=1.4%, was also conservatively derived to account for any possible systematic effects. The degradation of TPB when exposed to the most intense VUV wavelength (160 nm) of the deuterium lamp was tested for 2.5 h. The sample did not degrade, showing that the sample does not degrade during the time the measurements take (1 h and the sample is exposed to the most intense wavelength only for 10 min).

An investigation of the dead time of the data acquisition is presented in Section A.1. The dead time is negligible for the measurements of the plastic samples and is higher for TPB, which has a bright fluorescence response. Here, the dead time varied, depending on the intensity of the light, between 0.03% and 14.2% (being mostly below 2% and reaching 14.2% at the peak of the intensity of the deuterium lamp, 160 nm).

To investigate how the vacuum level affects the intensity of the excitation light, I calculated the dependence of the intensities of light from 70 nm to 250 nm on the air pressure, p. First,

I calculated the linear attenuation coefficient, μ for values from 10 mbar to 1×10^{-5} mbar, as shown in Equation 2.1.

$$\mu(p) = \rho_{O_2}(p) \times \sigma_{abs} \times N_a / M_{O_2} \tag{2.1}$$

where ρ_{O_2}(p) is the pressure-dependent density of molecular oxygen in air (since nitrogen does not absorb VUV light), σ_{abs} is the absorption cross-section of molecular oxygen [96], N_a is the Avogadro number and M_{O_2} is the molar mass of molecular oxygen.

The intensity of the UV light (relative to the intensity without attenuation) at a distance d from the source is calculated by Equation 2.2 for each pressure p and shown in Figure 2.5 for different levels of vacuum and considering a distance between light source and sample of 20 cm .

$$\frac{I}{I_o} = e^{-\mu(p) \times d} \tag{2.2}$$

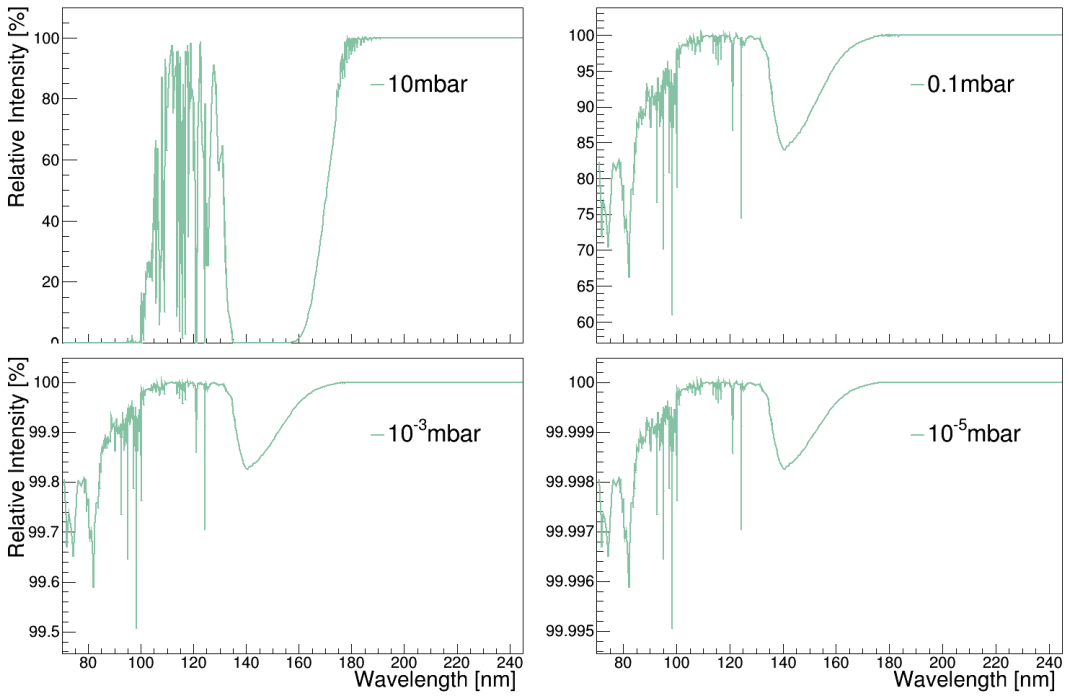

FIGURE 2.5: Relative intensity of the excitation light vs. wavelength for different values of pressure inside the chamber. The y axis are shown with different scales.

Figure 2.5 shows that the intensity of the excitation light is not strongly dependent on the vacuum level for values below 10^{-3}mbar. Therefore, the minimum vacuum level for the fluorescence measurements was set as 5×10^{-4}mbar.

2.3.3.2 Calibration of the spectral response of the Ocean Optics QE65000 spectrometer

A halogen lamp with absolutely calibrated intensity was used to measure the wavelength-dependent response of the Ocean Optics QE65000 spectrometer together with its optical fiber and lens. The spectrum of the lamp was measured with the spectrometer. The lens attached to the optical fiber of the spectrometer was at a distance of approximately 30 cm from the lamp. Four independent measurements were taken to build the average.

By comparing the measured spectra to the reference spectrum of the lamp, it is possible to derive the wavelength-dependent response of the spectrometer, fiber and lens. This response can be used to correct the spectra of wavelength shifters measured with this spectrometer, such as TPB. Since the intensity of the halogen lamp is very low at wavelengths below 300 nm, the correction was derived in the range from 300 nm to 950 nm, as shown in Figure 2.6. The dark gray line shows the mean value of the 4 measurements and the shaded area shows one standard deviation from the mean.

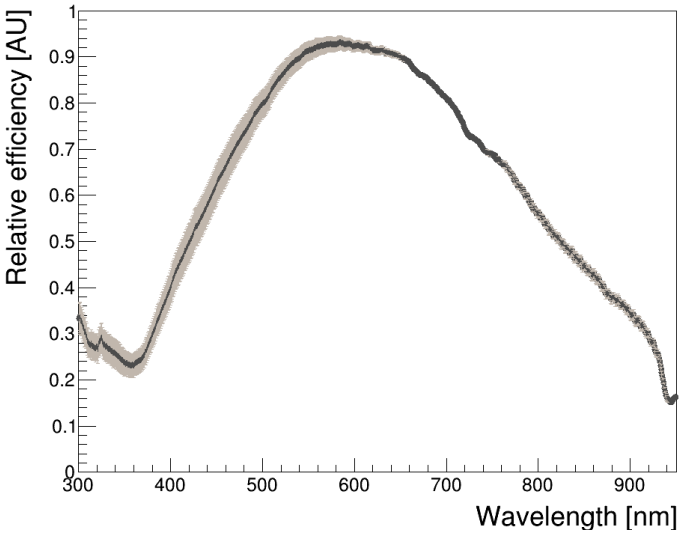

FIGURE 2.6: Convoluted wavelength-dependent detection response of the Ocean Optics QE65000 spectrometer, its optical fiber and lens.

As a comparison, the spectrum of the lamp without lens was measured and no difference was observed. Therefore, the transmittance of the lens is probably flat above 300 nm.

Figure 2.7 shows the emission spectra of TPB before (blue) and after (magenta) the wavelength-dependent response correction. As a comparison and cross-check, the same sample was measured with a Cary Eclipse spectrophotometer (described in Subsection 2.4.1) with an excitation wavelength of 260 nm (this device does not provide a good signal at lower excitation wavelengths and its lowest excitation wavelength is 190 nm). Both the spectrum measured with this setup (black line) and the corrected spectrum measured with the Ocean Optics match. However, the spectrum published in [54], which is often used as reference for TPB, seems to be shifted to the left.

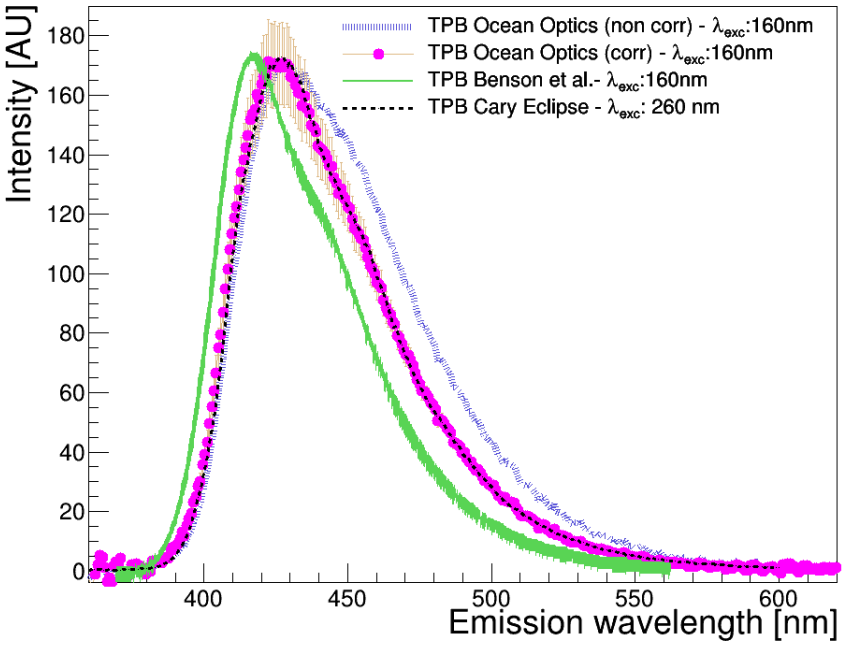

FIGURE 2.7: Fluorescence emission spectra of TPB. In dashed blue: non-corrected spectrum measured with the Ocean Optics spectrometer for 160 nm excitation light. In magenta: the same spectrum after corrections. The error bars come from the uncertainty in the correction factors. In dashed black: spectrum of the same sample measured with the Cary Eclipse spectrophotometer with 260 nm excitation light, which coincides perfectly with the one in magenta. In green: Spectrum of TPB excited with 160 nm, from [54].

It is not clear if this shift could be dependent on the batch of TPB and substrate or if the spectrum measured by [54] was not properly corrected for the response of the spectrometer.

In addition to TPB, the wavelength shifter 1,4-Bis(2-methylstyryl)benzene (Bis-MSB) was measured. Its spectrum was also corrected for the calibrated response of the spectrometer and compared to the spectrum measured with the Cary Eclipse spectrophotometer. These measurements are described in Section A.2. The spectrum measured with the Cary Eclipse and the one measured with the Ocean Optics (after correction) also match. Furthermore, the relative photon yield of the WLSs TPB and Bis-MSB measured with the spectrometer match the values measured with the PMT (see Section A.2 for more details).

2.3.3.3 Slit width and energy resolution

The energy resolution of the band of excitation light depends on the slit widths of the monochromator. In these measurements, the slits were wide open to allow more light to go through, since very low-levels of fluorescence were expected. To investigate the broadness of the selected bandwidth of excitation light, the spectra of the excitation light of selected (nominal) wavelengths of 210 nm, 250 nm, 280 nm and 300 nm were measured with the spectrometer. Lower wavelengths were not measured because the spectrometer is not sensitive to light below 190 nm.

The lens used in the setup to collect the light into the fiber does not observe the incident light directly, but sees the excitation light that is reflected by the sample. Therefore, PTFE was used to reflect the excitation light, directing part of it into the lens. Figure 2.8 shows the spectra of the light reflected by PTFE.

The position of the peaks roughly agree with the nominal wavelength. The peaks can appear slightly shifted due to the wavelength-dependent response of the spectrometer (not characterized below 300 nm) and the wavelength-dependent reflectance of PTFE. The peaks were fitted by a gaussian and the standard deviations of the fits will be added as error bars in the results presented at the end of this section.

2.3.4 Procedures

All the samples were placed in the sample holder with the same geometry relative to the excitation slit and light detector for a set of measurements at a given angle.

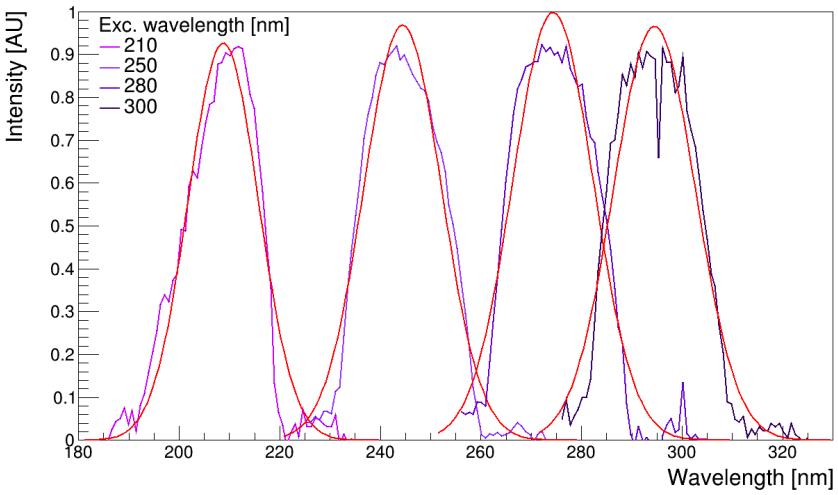

FIGURE 2.8: Spectra of the excitation light of nominal wavelengths 210, 250, 280 and 300 reflected by PTFE.

In order to guarantee the stability and reproducibility of the measurements (investigated in Subsection 2.3.3.1), all the sample measurements followed the same procedures and requirements: i) The pressure inside the monochromator chamber and flange was less than 5×10^{-4}mbar; ii) The lamp was turned on 40 minutes before starting the measurements; and iii) the PMT was turned on at least 60 minutes before starting the measurements.

During the warm-up time of the lamp, the emission slit of the monochromator was closed to prevent the samples from degrading[3]. Then, the slit was opened 5 mm wide and the emission from the sample was measured for the selected excitation wavelength.

The spectrometer measured the fluorescence spectra and the PMT measured the wavelength-integrated fluorescence intensity of the samples. The spectrometer was set up to record each spectrum 10 times with 10 s illumination time each. The output spectrum is the average of those measurements after background subtraction. For the wavelength-integrated measurements, the optical fiber was coupled to the PMT. For a single measurement, the PMT rate was recorded ten times over a 50 s window. The same procedure was used to measure the background (dark count and background light), which was taken at the beginning and at the end of the measurement of a sample, with the slits closed.

Two sets of wavelength-integrated measurements were done. In the first one, all the acrylic and reference samples (listed in Section 2.2) were excited with light of wavelengths 130 nm

[3]TPB, for instance, is known to degrade with time when exposed to UV light.

and 160 nm, under an incidence angle of 39.5°. These measurements were done without the acrylic filter in front of the PMT window.

Then, a second set of measurements was done with the filter, in order to extend the range to higher wavelengths (note that the PMT is sensitive to light above approximately 180 nm, as shown in Figure 1.11). The filter was used to absorb the excitation light reflected by the sample and stray light from the monochromator. For this set of measurements, the RPT and Spartech acrylic were plasma cleaned and measured with excitation wavelengths of 130 nm, 150 nm, 160 nm, 170 nm, 180 nm, 210 nm, 250 nm, 280 nm and 300 nm and under incidence angles of 39.5° and 12.5°. The PTFE, TPB (sample 2) and aluminium samples were also measured with these excitation wavelengths and under the same angles.

The first set of measurements was mainly done as an investigation of stray light and background fluorescence, which is described in the next subsection.

2.3.5 Stray light and background fluorescence investigation

To measure the level of stray light in the setup, the monochromator was set to pass either 130 nm or 160 nm, and the chamber was re-pressurised to atmospheric pressure, while keeping the samples inside the setup and the lamp on. In this configuration, the VUV excitation light is absorbed by the oxygen in the air (see Figure 2.9), and only stray light above approximately 180 nm reaches the sample.

The light detected in these measurements is composed of: i) stray light above 180 nm reflected by the samples, ii) photoluminescence induced in the sample by stray light, and iii) background light and dark count (here called dark rate). The last contribution was independently measured and can be subtracted from the VUV filtered light level to learn about the level of stray light (contributions i and ii). Table 2.1 shows the signal yield in the VUV filtered measurements, and the percentage of stray light (contributions i and ii) and dark rate (contribution iii) relative to the total signal detected in the sample measurements (that is, in the measurements of the sample with the excitation light impinging on it).

Table 2.1 shows that TPB yields the highest absolute VUV filtered signal, which indicates that TPB fluoresces when excited by stray light. However, this component is negligible when

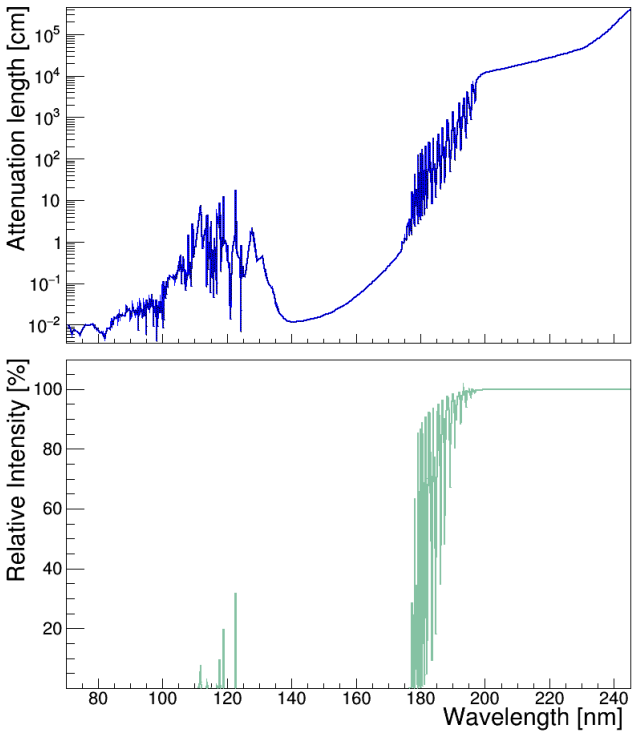

FIGURE 2.9: Upper plot: Attenuation length of the VUV light in air (these values were calculated using the attenuation coefficient of Equation 2.1). Bottom: Relative intensity of VUV light reaching the sample at a distance of 20 cm from the source when the chamber is filled with air (see Equation 2.2 for details).

Sample	Exc. wavelength:130 nm			Exc. Wavelength:160 nm		
	VUVfilt. (Hz) ±σ	SL ±σ (%)	Dark rate ±σ (%)	VUVfilt. (Hz) ±σ	SL±σ (%)	Dark rate ±σ(%)
TPB	116.41 ± 3.39	0.21 ± 0.01	0.04 ± 0.01	148.81 ± 3.74	0.06 ± 0.00	0.01 ± 0.00
RPT	17.27 ± 3.34	3.84 ± 5.26	15.36 ± 3.86	16.59 ± 3.34	1.28 ± 2.18	6.39 ± 1.58
RPT (rough)	38.41 ± 3.35	19.52 ± 4.00	11.49 ± 2.79	45.15 ± 3.35	12.29 ± 1.95	5.66 ± 1.35
RPT (w. bond)	19.67 ± 3.36	4.48 ± 18.68	72.79 ± 22.59	23.38 ± 3.38	9.42 ± 9.48	35.93 ± 10.29
Spartech	24.36 ± 3.41	1.9 ± 6.87	32.96 ± 5.79	21.32 ± 3.37	0 ± 0.00	17.14 ± 3.08
Spartech (rough)	62.22 ± 3.40	32.51 ± 4.56	15.89 ± 2.92	68.40 ± 3.42	21.27 ± 2.39	9.06 ± 1.56
Spartech (w. bond)	25.41 ± 3.37	6.2 ± 10.43	48.96 ± 14.98	26.86 ± 3.36	3.21 ± 3.56	16.78 ± 3.28
SNO	31.73 ± 3.40	3.81 ± 13.89	87.17 ± 25.62	34.29 ± 3.44	8.56 ± 10.95	66.94 ± 19.50
sandpaper	46.37 ± 3.34	58.53 ± 12.83	44.61 ± 9.34	57.92 ± 3.37	69.88 ± 12.08	37.01 ± 7.61
Aluminium	56.17 ± 3.39	29.66 ± 4.92	23.47 ± 3.54	67.62 ± 3.37	20.33 ± 2.57	11.78 ± 1.75
Sample holder	43.25 ± 3.37	26.78 ± 9.46	53.41 ± 9.16	45.49 ± 3.38	17.21 ± 5.05	29.73 ± 3.94
empty flange	21.32 ± 3.37	4.63 ± 16.02	67.25 ± 17.64	22.00 ± 3.35	4.27 ± 9.87	41.44 ± 9.2

TABLE 2.1: Signal yield in the VUV filtered measurements normalized by the recording time of the measurements, and percentage of the signal detected in the sample measurement that is due to stray photons (SL) and due to dark rate. All the values are shown for the excitation wavelengths 130 nm and 160 nm.

considered relative to the total fluorescence signal induced by the nominal wavelength (see the small SL value). By comparing the SL values of TPB at 130 nm and at 160 nm, one can see that the relative contribution of the stray light is smaller at 160 nm, where the intensity of the deuterium lamp peaks. For samples that had a very low light response, the difference is not very pronounced. This might indicate that the level of stray light is roughly constant, and that the samples with a low light yield are only reflecting this stray light (contribution i rather than ii). Note that the rough samples yield a higher VUV filtered signal. This increase might be due to their higher reflectivity, since the SL values are also higher (10-35% against approx 0-9% for the smooth samples).

The level of background fluorescence can be roughly estimated with the measurements of the aluminium sample, of the empty sample holder and the empty flange. Out of the light detected from the aluminium sample, 20 to 30% is due to stray light and 11 to 23% is due to dark rate (see SL and dark rate (%) values in Table 2.1). The rest can be either fluorescence of the lens induced by the excitation light reflected by the aluminium or fluorescence of any impurity in the sample (which is unlikely, since it is plasma cleaned). The light yield due to stray light or fluorescence of the lens are expected to be higher for an aluminium sample than for an acrylic sample, since aluminium reflects the excitation light better.

Most of the light detected in the measurements of the sample holder and of the empty flange is stray light or dark rate, as shown by the SL and dark rate (%) values. The total signal yield of their measurements done without filtering the excitation light is very low (not shown in the table). The total signal yield is consistent (within errors) with zero after the subtraction of the VUV filtered signal for 130 nm light and at the level of 0.01% of the photon yield of TPB for 160 nm light. This means that background fluorescence from possible contamination in the chamber is negligible. That is, there is no other significant source of background in the setup in addition to stray light and the possible low-level fluorescence of the lens, which are expected sources of backgrounds, as discussed in Subsection 2.3.2.

In the VUV filtered measurements of acrylic with the filter in front of the PMT, the signal was similar to the dark rate. That means that the amount of stray light that goes through the filter in these measurements is negligible. The VUV filtered measurements of PTFE (with acrylic filter) corresponded to 48% of the total amount of light detected in the measurements

of PTFE excited with 160 nm. Therefore, also with filter, there is a non-negligible amount of stray light being detected by the PMT when measuring PTFE. This is expected, since the amount of reflected stray light depends on the reflectance of the sample and PTFE is highly reflective.

2.3.6 Data analysis and discussion

2.3.6.1 Spectrometer measurements

The emission spectra of TPB, PTFE and RPT acrylic excited with 160 nm light were background subtracted and the spectrum of TPB was corrected for the response of the spectrometer. The average spectra are shown in Figure 2.10.

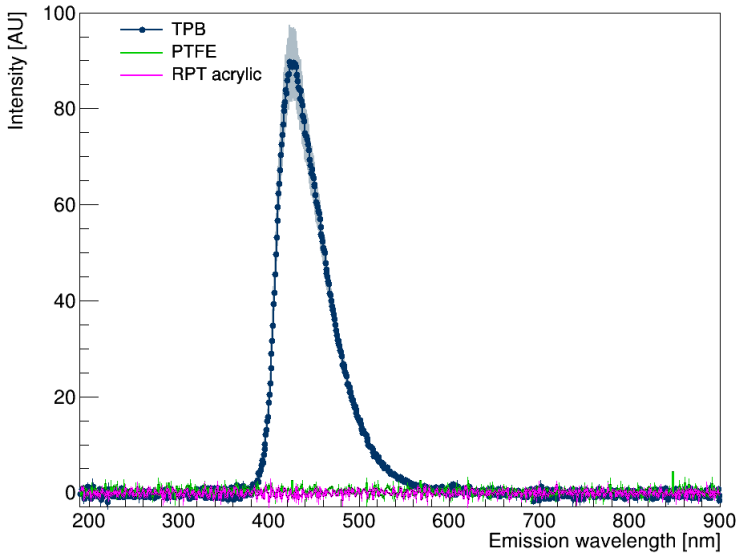

FIGURE 2.10: Emission spectra of the TPB, PTFE, and RPT acrylic measured with 160 nm excitation light at an incident angle of 39.5°. The error bars (shown in gray) come from the uncertainty of the response function of the spectrometer.

To better evaluate whether a low-level of fluorescence was detected, the distribution of the intensities of the spectrum of RPT acrylic from 300 nm to 600 nm were plotted in a histogram and compared to the distribution of the intensities of the spectrum of TPB from 650 nm to 950 nm (above the wavelengths emitted by TPB, where no fluorescence is expected). This comparison is shown in Figure 2.11.

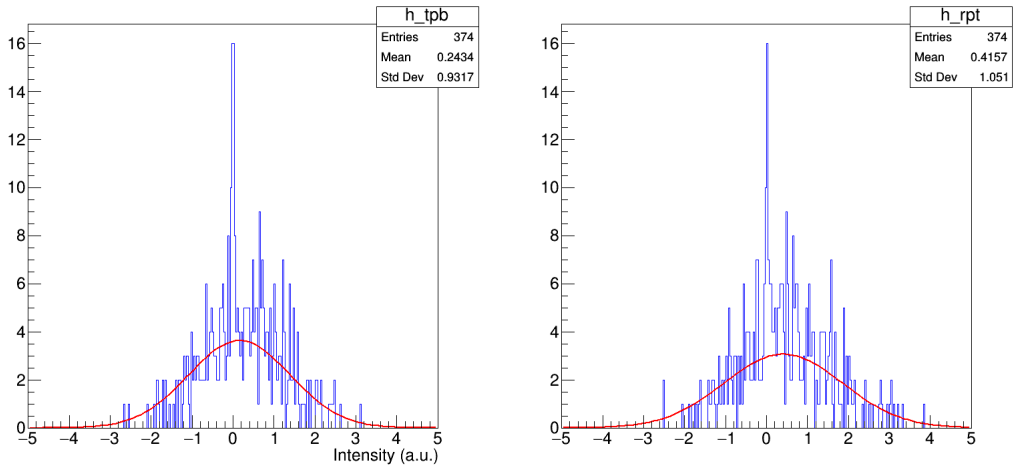

FIGURE 2.11: 1D Histograms: Distribution of the intensities of the spectrum of TPB from 650 nm to 950 nm (left) and RPT from 300 nm to 600 nm (right).

The shapes of the distributions are very similar and their mean values agree within one sigma. Therefore, no fluorescence response significantly above the noise was detected from the RPT acrylic. The same is true for the PTFE sample.

The signal to noise ratio is approximately 1%, which allows to set a limit on the light yield of PTFE and RPT acrylic relative to TPB, assuming that these samples emit light at roughly the same wavelength range of the emission from TPB. If they emit light at shorter wavelengths, the limit is weakened, since the spectrometer is less sensitive, as shown in Figure 2.6. If they emit light between 500 nm to 600 nm, the limits are below 1%.

2.3.6.2 Wavelength-integrated measurements

The PMT rate of a sample excited with a certain wavelength was determined by averaging the rates from the 10 individual measurements and correcting it for the dead time of the counter. The uncertainty on the rate is given by the statistical and systematic errors. The statistical error is the standard deviation of the 10 measurements. As described in Subsection 2.3.3.1, the measurement has a systematic error due to the stability of the lamp, σ_{syst}^{Lamp}, and due to the stability of the PMT, σ_{syst}^{DR}. .

The sample rate is then background subtracted: For the first set of measurements (without acrylic filter), the rate of the VUV filtered measurement was subtracted; For the second set

of measurements (with acrylic filter), the rate of the dark measurement was subtracted, since VUV filtered measurements could only be done for part of the excitation wavelength range.

After these corrections, the mean rates of the measurements of the plastic samples were divided by the mean rate of the TPB sample[4] measured at the same angle and with the same excitation wavelength. The errors are propagated and the ratios result in the relative photon yield. Note that the term "photon yield" of a sample will be often used throughout this thesis an does not imply that the measured samples fluoresce, but rather mean the amount of light detected while measuring them. The relative photon yield for the first set of measurements (without acrylic filter) and their errors (2 standard deviations) are shown in Table 2.2.

Sample	Exc. wavelength:130 nm	Exc. Wavelength:160 nm
	Rel. photon yield (%) ± 2σ	Rel. photon yield (%) ± 2σ
RPT acrylic	0.1504 ± 0.0302	0.0839 ± 0.0112
RPT acrylic (rough)	0.1769 ± 0.0353	0.0867 ± 0.0099
RPT acrylic (with bond)	0.0120 ± 0.0300	0.0118 ± 0.0100
Spartech acrylic	0.0942 ± 0.0313	0.0475 ± 0.0122
Spartech acrylic (rough)	0.1373 ± 0.0458	0.0660 ± 0.0105
Spartech acrylic (with bond)	0.0427 ± 0.0529	0.0452 ± 0.0148
SNO acrylic	0.0065 ± 0.0416	0.0047 ± 0.0106
sandpaper used in DEAP	0.0001 ± 0.0013	0.0000 ± 0.0001

TABLE 2.2: Relative photon yield of acrylic from different batches and/or surfaces, and of the sandpaper. All the samples were excited with 130 and 160 nm light under an incidence angle of 39.5°. Values are relative to the fluorescence yield of TPB measured in the same conditions.

By subtracting the rate of the VUV filtered from the rate of the sample measurements, the sample rate was corrected for both stray light and dark measurement. Therefore, the non zero values of the photon yield of smooth and rough RPT and Spartech acrylics either indicate that they fluoresce or indicate that the lens fluoresces when excited with light reflected by the samples, as discussed in Subsection 2.3.5.

The acrylic samples with bond and the SNO acrylic presented very low photon yield, consistent with zero within errors. This could be either due to their different geometry (described in Section 2.2) which led to uncertainties in their positioning in the sample holder or because they fluoresce less than the other acrylic samples. The sandpaper also did not yield any light, which proves that it does not fluoresce. Note that the sandpaper is black and may

[4]Sample 1 was used for the first set of measurements and sample 2 for the second. The efficiency of the samples were roughly the same.

not reflect enough light to induce fluorescence of the lens. These samples, which presented low photon yield, were not further measured. Furthermore, the limits on the WLSE of the acrylic samples with bond and the SNO acrylic will not be presented together with the final results, since there is an uncertainty on the positioning.

In the second set of measurements, the excitation wavelength range was extended to 300 nm, an acrylic filter was used to absorb the reflected excitation light (and most of the stray light), the acrylic samples were plasma cleaned, and PTFE was also measured. At excitation wavelengths above 180 nm, it is not possible to assess the level of stray light with the VUV filtered measurements. Therefore, the photon yield was corrected only for the dark measurement. The relative photon yield and its dependence on excitation wavelength is shown in Figure 2.12.

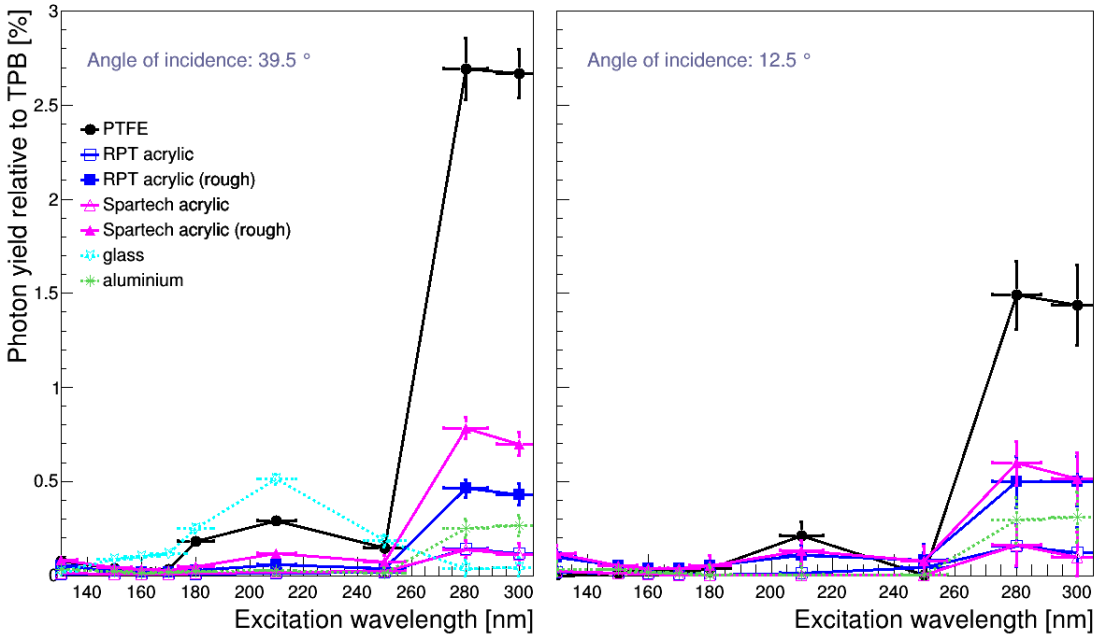

FIGURE 2.12: Photon yield vs. excitation wavelength of plastics and reference samples (see legend) relative to TPB at different angles of incidence: 39.5° on the left and 12.5° on the right. The two-standard-deviation error bars on the relative photon yield include the statistical and systematic errors. The error bars of the excitation wavelengths are the standard deviation of the gaussian fits of the distribution of excitation light.

The wavelength dependence may be mostly due to the dependence of the sensitivity on the wavelength, since the measurements are most sensitive[5] at wavelengths around 160 nm (the

[5]That is, the greatest signal to noise ratio when measuring a fluorescent sample, such as TPB.

highest intensity of the lamp). Furthermore, the sensitivity depends on the transmittance of the acrylic filter and on the reflectance of the sample, both of which are wavelength-dependent. Samples that are more reflective (such as PTFE) reflect more excitation light and more stray light, which can either induce the fluorescence of the lens or be transmitted by the filter and be detected. The latter seems to be the case for 280 nm and 300 nm excitation light, since the filter presents a small bump in its transmittance around these wavelengths, as shown in Figure 1.11.

These bumps in the transmittance of acrylic at approximately 260 nm to 320 nm seem to be common for UVA acrylic[6]. Two possible explanations are: i) acrylic has two separated absorption bands in the UV due to unsaturated systems [97] and the bump appears in between these bands; or ii) acrylic fluoresces at a low-level when excited with light between 260 nm to 320 nm. In the second case, the bump would appear because the UV-VIS spectrometer (used to measure the transmittance of the filter) would detect the fluorescence light instead of the excitation light and interpret it as less absorbance to this excitation wavelength.

Even though the wavelength dependence may be mostly related to the sensitivity at different wavelengths, the wavelength dependence of the WLSE of TPB and of the possible fluorescence of the samples may also play a role. Note that the photon yield of the glass sample decreases at 280 nm and 300 nm while the photon yield of the acrylic samples increases. Also note that the glass may also fluoresce and its cleaning process was not so rigorous like the one for the other samples (see Section 2.2 for more details).

To better observe the angle dependence of each measurement between 130 nm and 250 nm and the differences between the rough and smooth samples, the relative photon yield measured at both angles were plotted together in this wavelength range and separated by sample. This is shown in Figure 2.13 for PTFE and in Figure 2.14 for acrylic. The measurements of aluminium at both angles are shown in Figure 2.13. Since these measurements agree within errors, only one measurement of aluminium is shown in the other figures.

As evidenced by these figures, the angle dependence of the relative photon yield is minor: The relative photon yield of acrylic measured at different angles are mostly consistent within errors

[6] I contacted some manufactures, whose datasheets of UVA acrylic also showed these bumps in the transmittance, and none of them could explain the reason for the bumps.

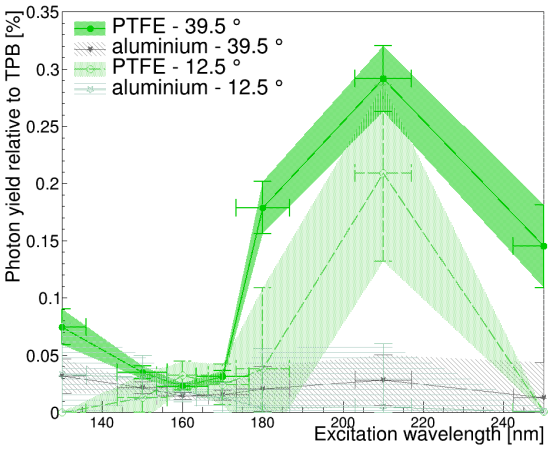

FIGURE 2.13: Photon yield of PTFE relative to TPB. Lines and shaded area are shown to guide the eyes through the measured data points and error bars.

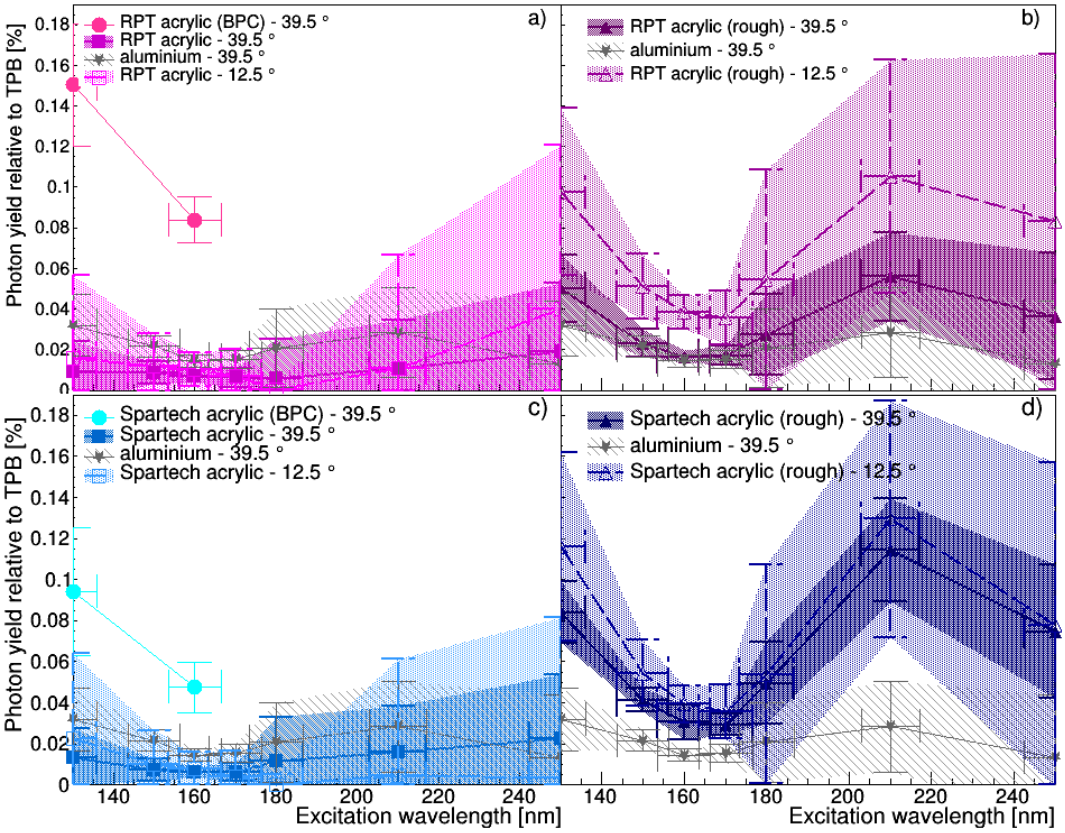

FIGURE 2.14: Photon yield of RPT and Spartech acrylic relative to TPB for different excitation wavelengths and angles of incidence (see legend). In a) the RPT acrylic before (BPC) and after plasma cleaning are shown, in b) the RPT acrylic after plasma cleaning and sanding, in c) the Spartech acrylic before (BPC) and after plasma cleaning are shown and in d) the Spartech acrylic after plasma cleaning and sanding are shown. In all the figures, the measurement of aluminium at 39.5° is shown. Lines and shaded area are shown to guide the eyes through the measured data points and error bars.

as well as the photon yield of PTFE measured with the most intense excitation wavelengths (150 nm to 170 nm). The slight disagreement for some excitation wavelengths can be either due to the angle dependence of reflected light, which is most relevant for PTFE, or due to differences in the angular distribution of light emitted by the samples.

Together with the measurements of the smooth acrylic sample, the measurements of the smooth samples of the first set of measurements (before plasma cleaning) are shown in Figure 2.14. Note that the acrylic samples yield less light after plasma cleaning. This could be due to fluorescent surface contamination, such as oils, present on the samples before cleaning. The photon yield of the aluminium sample, for instance, was 5 times higher before plasma cleaning (not shown in the figure). One concern about plasma cleaning is that it could damage the organic bonds of PMMA (or of the potentially fluorescent substance present in it) due to energetic-particle and/or VUV-photon impact. However, we did not observe less light yield from the samples irradiated for a long time in comparison to a new sample. That is, VUV did not seem to degrade the samples. Furthermore, if the organic bonds were superficially damaged, the sanding of the sample would eliminate this surface and expose a non degraded surface to the excitation light.

Figure 2.14 shows that the rough samples presented higher photon yield. This increase could be due to: i) effects coming from the different path of excitation light after reaching the surface, which could, for instance, result in more reflected stray and excitation light; ii) less angle-dependence of the light emission distribution; or iii) due to the aforementioned resurfacing, which removes any possibly degraded surface. Note that fluorescence of residue from the sandpaper as a cause of the enhanced photon yield has already been excluded.

2.3.7 Results: Upper limits on the wavelength shifting of acrylic and PTFE relative to TPB

The spectrometer did not detect any fluorescence emission from acrylic or PTFE within its sensitivity, which is of 1% in the wavelength range of light emitted by TPB. Therefore, any fluorescence signal at this range must be below the 1% level.

The measurements with the PMT have a better signal to noise ratio, since the PMT integrates the signal over a range of wavelengths. The noise (dark rate) to signal ratio[7] is approximately 7×10^{-5} for 160 nm excitation light (and a bit higher for other wavelengths). The light yield[8] of the aluminium reference sample relative to TPB varies from 1×10^{-4} to 5×10^{-4}, showing that the low-level background fluorescence and stray light in the setup are only slightly above the dark rate. However, the photon yield of the plastic samples are roughly in the same order of magnitude. Thus, it is not possible to decouple the low-level background fluorescence and stray light in the setup from the possible low-level of light emitted by the plastics.

Therefore, the relative photon yield and their uncertainty are used to derive upper limits on the WLSE of these plastics relative to TPB. The 95%-confidence-level limits are the sum of the mean relative photon yield and the 2 standard deviations, which include statistical and systematic errors. These results are shown in Figure 2.15 against the excitation wavelength (from 130 nm to 250 nm).

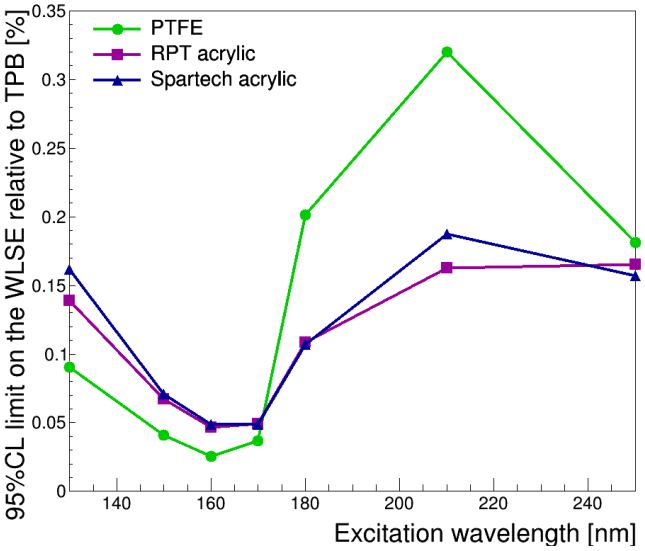

FIGURE 2.15: 95% CL upper limit on the wavelength shifting efficiency of PTFE, RPT acrylic, and Spartech acrylic relative to TPB for different excitation wavelengths. Also shown are the limits based on the photon yield of RPT and Spartech acrylics before plasma cleaning (BPC). Lines are shown to guide the eyes through the measured data points.

The upper limits on the fluorescence of acrylic were calculated using the photon yield of the rough samples. These results lead to more conservative limits, since the fluorescence light

[7] That is, dark rate divided by the light yield of TPB excited with 160 nm light.
[8] For excitation wavelengths from 130 nm to 250 nm.

emitted by the rough samples should be less dependent on the angle[9] and if the sample was degraded after plasma cleaning, a new surface was exposed to the VUV light after sanding. Even though the relative photon yield of RPT acrylic before plasma cleaning would lead to a slightly higher limit than the ones presented in Figure 2.15, they were not taken into account, since its higher photon yield could be due to superficial contaminations, which are not present in the AV of DEAP, since the AV was resurfaced (sanded).

The upper limits presented here refer to the wavelength shifting efficiency (WLSE) as defined[10] in [54], which is dependent on the thickness of the WLS. The thickness-dependent WLSE of TPB can be found in [54, 55].

These results are valid for an emission spectrum similar to the one of TPB. If this is not the case, the results must be corrected for the wavelength-dependent sensitivity of the setup, shown in Figure 1.11. This correction was not done, because no emission spectrum of PTFE or acrylic was detected by the spectrometer.

The limits on the WLSE of acrylic for 280 nm and 300 nm excitation wavelengths were one or two orders of magnitude higher than the limits for the wavelength range shown here. This is mainly because the setup is not sensitive to these wavelengths (due to the intensity of the lamp and transmittance of the filter). Therefore, the response of acrylic and PTFE to UV light of wavelengths higher than 250 nm will be investigated with the setups of Section 2.4 and Chapter 3.

2.3.8 Conclusion

The photoluminescence response of acrylic and PTFE to VUV light was tested at the level of 10^{-3} of the wavelength shifting efficiency of the TPB reference sample.

[9] The dependence of the relative photon yield on the angle and wavelength were more thoroughly discussed in the previous section.

[10] This definition is different from the intrinsic quantum efficiency, since it does do not take absorption and surface effects into account.

These results set stringent limits on the wavelength shifting efficiency of these plastics when excited by UV light from 130 nm to 250 nm and for an emission spectrum similar to the spectrum of TPB. The limiting factors of the sensitivity were i) stray light from the monochromator and ii) fluorescence of the optical lens, induced by excitation light reflected by the samples. It was also shown that the cleaning procedure of the plastics may play an important role in the level of photoluminescence.

The next step is to cross-check if these limits remain the same at LAr and LXe temperatures. Measurements at low temperatures and with a UV LED were done for this reason. They are described in Chapter 3.

2.4 Measurements of acrylic with UV light above 190 nm

2.4.1 Setup

The Cary Eclipse Fluorescence Spectrophotometer, shown in Figure 2.16, was used to measure the response of acrylic to UV light from 190 nm to 380 nm.

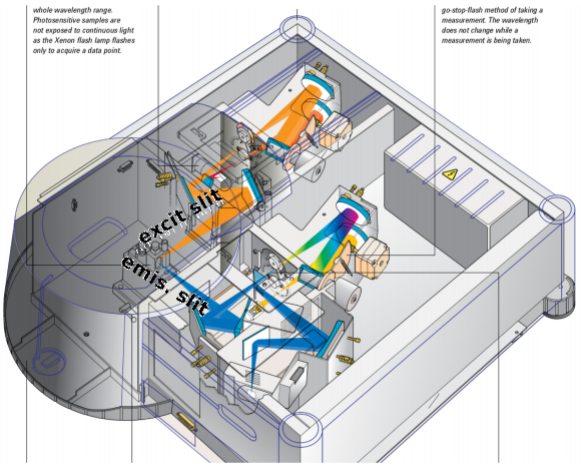

FIGURE 2.16: Cary Eclipse Fluorescence Spectrophotometer

In this setup, the samples are excited with a selected wavelength of light from a xenon lamp and the spectrum of the light emitted by the sample is measured by a photodetector. The setup has room light immunity and the recorded spectrum is already corrected for it.

This device is more sensitive than the VUV setup at these wavelengths because the intensity of the xenon lamp is higher than the intensity of the deuterium lamp in this range.

Another motivation for using this setup was the fact that some collaborators from DEAP measured the fluorescence of the acrylic samples with this setup. They suggested that fluorescence light from acrylic was observed for excitation light below 230 nm. These results were cross-checked.

2.4.2 Procedures

Similarly to the measurements done with the VUV setup, the light yield of acrylic is compared to the fluorescence of TPB. To allow for the direct comparison, the conditions for all the

measurements should be the same. The voltage of the photodetector was always 600 V[11], but the widths of the excitation (exc.) and emission (em.) slits varied for each sample, in order to increase the sensitivity for the samples that yield less light. Therefore, the relation between slit width and light yield is investigated in Subsection 2.4.2.2. Different excitation and emission filters - that is, filters that are placed before and after the slits - were also used for each measurement. Their effect on the light yield is characterized in Subsection 2.4.2.1.

The samples were placed inside the spectrophotometer in two different ways: "front face" (as shown in Figure 2.17) and "back face". Figure 2.18 shows these configurations.

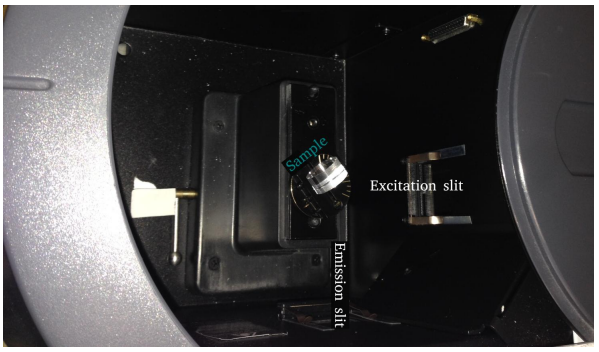

FIGURE 2.17: Cylindrical acrylic sample placed inside the Cary Eclipse Fluorescence Spectrophotometer.

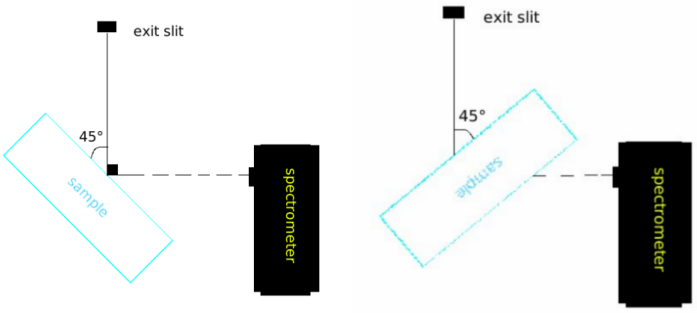

FIGURE 2.18: Scheme of two possible positioning of the samples: Front face is shown on the left and back face is shown on the right.

All the acrylic and reference samples listed in Section 2.2 were measured with this setup. The incidence angle was approximately 40°. The angle and the position of the the sample could not be very precisely controlled, since the sample did not fit inside the sample holder.

[11] At higher voltages, the photodetector saturated when measuring TPB.

As it will be shown later, this is not the main source of uncertainty. Thus, no improvements were made to mitigate this problem.

Before starting the measurements of acrylic and TPB, some reference samples were measured in order to understand the sources of stray light and background fluorescence in the setup. This investigation is discussed in the next subsection.

2.4.2.1 Stray light and background fluorescence investigation

In Subsection 2.3.2, I discussed how monochromators transmit a low level of light outside the selected bandwidth. The measurements with the VUV setup showed that this stray light can limit the sensitivity of the setup at some excitation wavelengths. To absorb most of the stray light, excitation filters can be used between the light source and excitation slit.

In order to characterize the stray light and sensitivity of the Cary Eclipse spectrophotometer, I measured the glass and aluminium samples described in Section 2.2 with and without exc. filter. The emission spectra of these samples excited with 260 nm light are shown in Figure 2.19. The spectrum of a standard xenon flash lamp is also shown for comparison. Both spectra without exc. filter are similar to the spectrum of the xenon lamp. This indicates that stray light is present in measurements without excitation filter.

The spectrum of the glass sample measured with excitation filter shows that there is some fluorescence from the glass in addition to stray light. This fluorescence extends from 360 nm to 680 nm and will be used to determine the relation between detected light and slit width in Subsection 2.4.2.2. The spectrum of the aluminium reference sample measured with filter shows that most of stray light is absorbed by the excitation filter, which absorbs light above 395 nm. The light detected in the measurement without filter is thus only stray light.

In order to investigate the effect of the filters on the measurements, I divided the measurements into four excitation and emission wavelength ranges, using different sets of filters:

- Excitation wavelengths from 250 nm to 380 nm and emission spectrum from 430 nm to 680 nm. The measurements in this range were done using an exc. filter with high transmittance from 250 nm to 395 nm and an emission filter from 430 nm to 1100 nm.

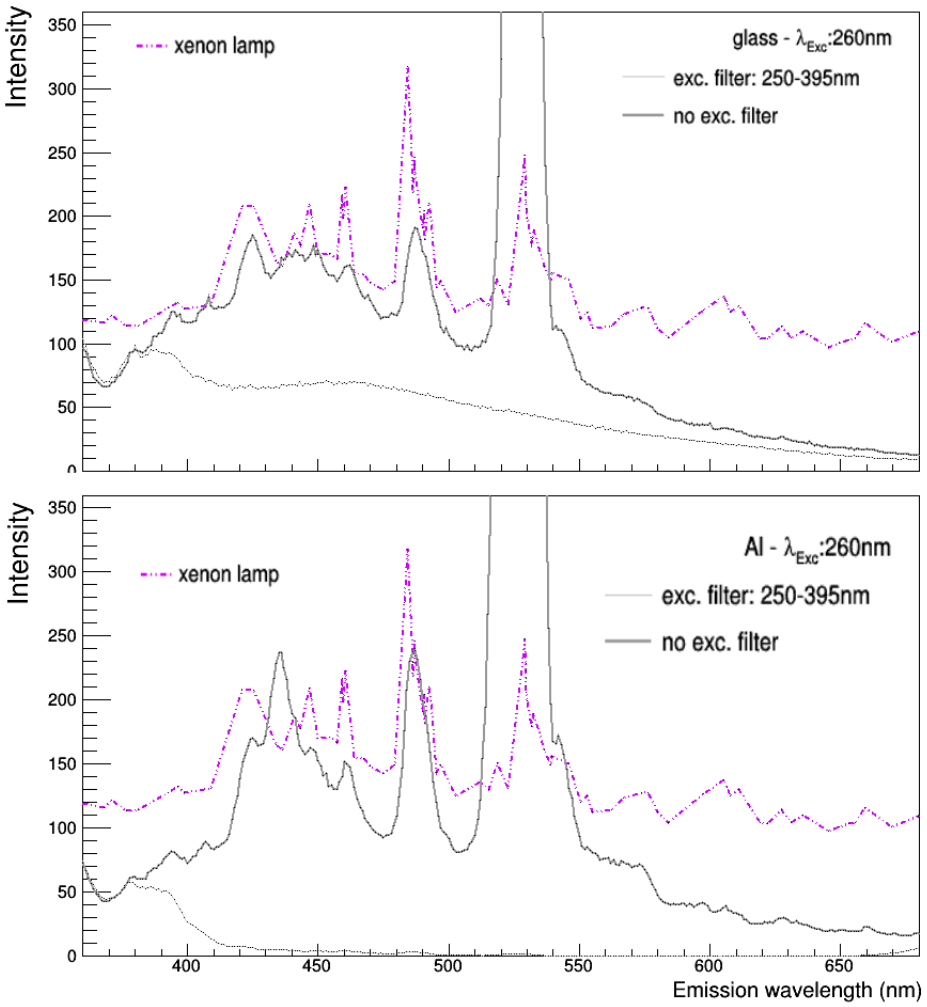

FIGURE 2.19: Top: Fluorescence emission spectra of a glass sample excited with 260 nm light, using 5-5 nm slit width. The measurement with exc. filter (250-395 nm) is shown by the dotted gray line and without filter is shown in solid gray. The dashed purple line shows the spectrum of a xenon flash lamp. Bottom: Fluorescence emission spectra (with and without filter) of a plasma cleaned aluminium sample for an excitation wavelength of 260 nm and 5-5 nm slits.

- Excitation wavelengths from 250 nm to 380 nm and emission spectrum from 390 nm to 680 nm. Same exc. filter of the previous range, but with an emission filter from 360 nm to 1100 nm. These measurements are referred as *Em. filter 2*.

- Excitation wavelengths from 190 nm to 240 nm and emission spectrum from 360 nm to 680 nm. For this excitation range, no excitation filter was available and the emission filter with transmittance in the range 360 nm to 1100 nm was used. These measurements are referred as *no exc. filter*.

- Excitation wavelengths from 250 nm to 300 nm and emission spectrum from 360 nm to 480 nm. Neither excitation nor emission filters were used and the excitation and emission wavelength range were therefore constrained by stray light and second order peaks These measurements are referred as *no filters*.

A common acrylic sample and the aluminium reference were measured using these 4 different ranges. The results are shown in Figure 2.20 and Figure 2.21. The emission spectrum for each excitation wavelength is shown in a different color.

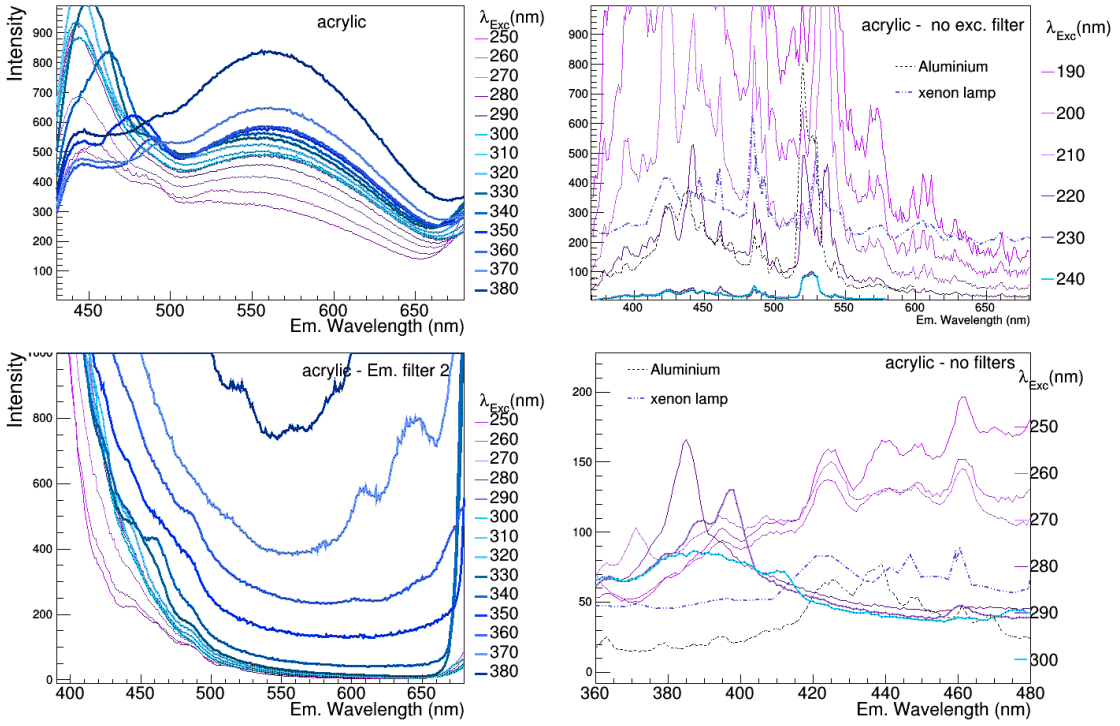

FIGURE 2.20: Fluorescence spectra of a stock acrylic sample for different filters and excitation/emission wavelength ranges. Upper left: These measurements were done with the 250-395 nm exc. filter and the 430-1100 nm em. filter. The exc. and the em. slits were both 20 nm open. Upper right: no exc. filter and the 360 nm to 1100 nm emission filter. Slits 5-2.5 nm. Bottom left: 250-395 nm exc. filter and 360 nm to 1100 nm emission filter. Slits 20-10 nm. Bottom right: no filters. Slits 5-5 nm

Figure 2.20 and Figure 2.21 show that the spectra of the same sample vary for different sets of filters and the spectra of aluminium and acrylic are similar for a given set of filters. This indicates that the filters autofluoresce. Therefore, the light detected in the measurements with filters (left plots) may be due to the fluorescence of the filters induced by the excitation

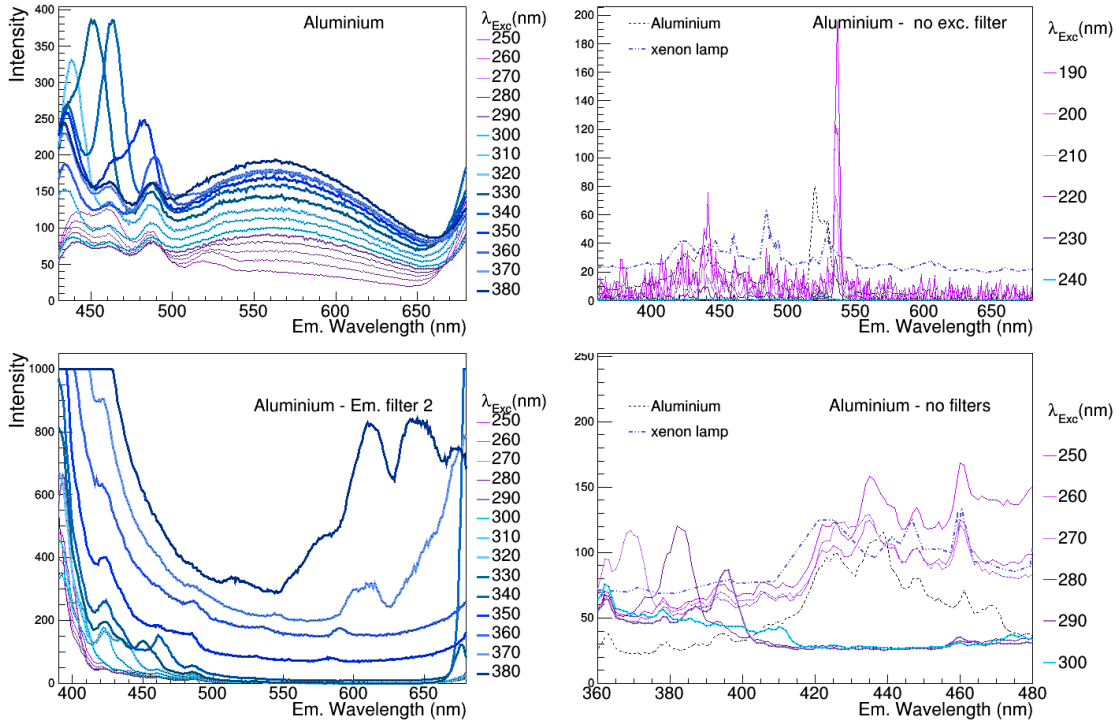

FIGURE 2.21: Measurements of the plasma cleaned aluminium sample. Upper left: These measurements were done with the 250-395 nm exc. filter and the 430-1100 nm emission filter. The exc. and the em. slits were both 10 nm open. upper right: no exc. filter and the 360 nm to 1100 nm emission filter. Slits 1.5-1.5 nm. Bottom left: 250-395 nm exc. filter and 360 nm to 1100 nm emission filter. Slits 10-5 nm. Bottom right: no filters. Slits 1.5-1.5 nm.

light (directly or reflected by the sample) and light detected in the measurements without exc. filters (plots on the right) are mostly stray light.

Note that the slits of the measurements shown in Figure 2.20 and Figure 2.21 were wide open (in comparison to the results shown in Figure 2.19) and that the intensities are not equivalent in the plots, since the slit width varies. By setting the slits to be wide open, we expect the detector to be more sensitive to the fluorescence light of the samples. However, mostly stray light or autofluorescence of the filters is detected. This means that if acrylic fluoresces, this fluorescence might be at the level or lower than the stray light of the monochromators and autofluorescence of the filters used in the Cary Eclipse spectrophotometer. The spectra shown in Subsection 2.4.3.1 also support this assertion.

2.4.2.2 Relation between slit width and light yield

In order to compare the light detected in the acrylic measurements to the fluorescence yield of TPB, the relation between the slit width and the light yield must be understood, since the slits were more open in the measurements of acrylic. This relation should be roughly linear. That is, increasing the size of one slit should equally increase the amount of light reaching the sample or reaching the detector. This does not seem to be the case for the Cary Eclipse spectrophotometer. Figure 2.22 shows that the increase of the signal from fluorescence is much higher than the increase of the slit width.

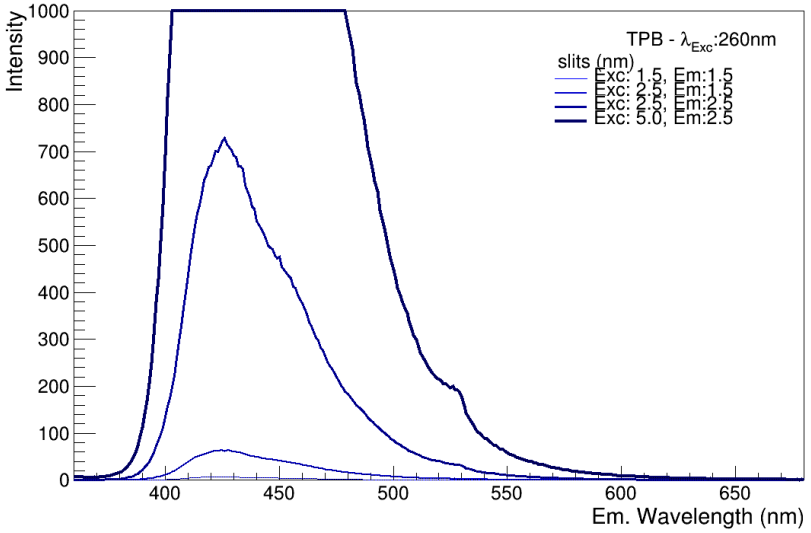

FIGURE 2.22: Emission spectra of the TPB reference sample excited with 260 nm light. Measurements were done with different exc. and em. slit widths (see legend), an exc. filter transmissive from 250 nm to 395 nm and an emission filter transmissive from 360 to 1100 nm. The photodetector saturated for the largest slit width.

The relation between slit width and light yield can be measured with TPB only for small slit widths, since the photodetector saturates for larger slits. To determine the relation between slit width and light yield for larger slits, the low-level background fluorescence from the glass sample was used. This relation is shown in the inset of Figure 2.23. It was not possible to determine the relation for larger slit widths because the signal saturates. A linear relation for larger slit widths will be thus assumed and this assumption will be the most relevant uncertainty in these measurements.

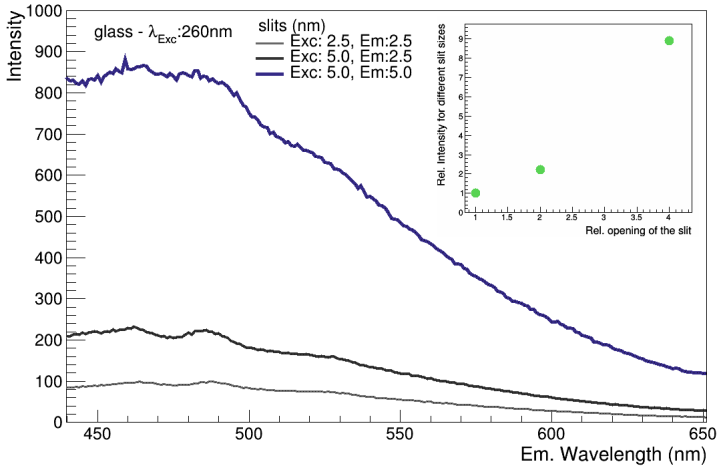

FIGURE 2.23: Fluorescence spectra of a glass plate excited with 260 nm light. Measurements were done with different exc. and em. slit widths (see legend), an exc. filter transmissive from 250 nm to 395 nm and an emission filter transmissive from 360 to 1100 nm.

2.4.3 Data analysis and discussion

2.4.3.1 Fluorescence emission spectra

I compared the measurements done with the Cary Eclipse at TUM to the ones done by other DEAP collaborators at Queen's University. The measurements of the Spartech acrylic done at TUM with excitation wavelengths from 200 nm to 300 nm and without excitation filters are shown in Figure 2.24. The emission spectra measured with different excitation wavelengths are shown in different colors. Also shown are the measurements of the aluminium reference sample and the spectrum of a standard xenon lamp.

Both TUM and Queen's measurements (not shown here) evidence that the Cary Eclipse spectrophotometer detects a high signal when set to its most sensitive setting (wide open slits from 5 nm to 20 nm and voltage medium or high). The high-intensity spectra of the acrylic sample is very similar to the one of the aluminium reference sample. This shows that the detected light is not coming from the fluorescence of the acrylic sample. The spectra reproduce very well the spectrum of a xenon lamp, which indicates that the signal is stray light, as investigated in Subsection 2.4.2.1.

Figure 2.25 shows the spectra of the Spartech and RPT acrylics measured using the front face configuration, without excitation filter and with excitation light from 200 nm to 300 nm.

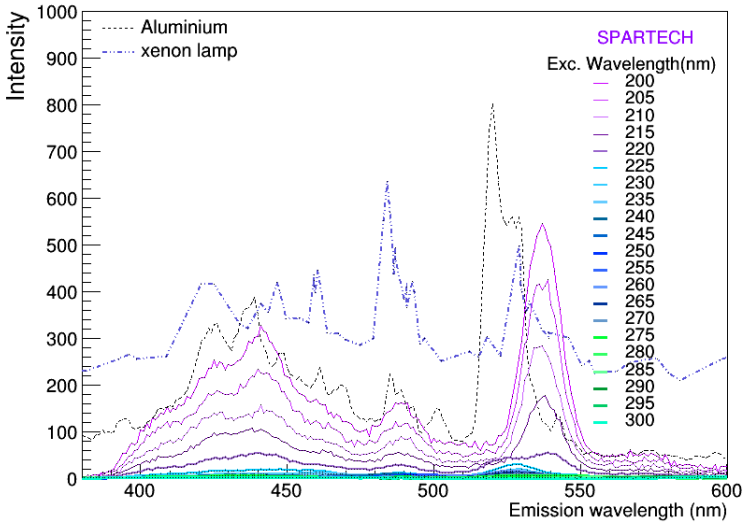

FIGURE 2.24: Fluorescence measurements of the Spartech acrylic sample for excitation wavelengths from 200 nm to 300 nm. These measurements were done using the back face position. Also shown are the measurements of an Aluminium plate and the spectrum of a xenon lamp.

In these spectra, a broad peak appears for excitation wavelengths above 250 nm (blue). This peak, unlike the others, cannot be explained by stray light (see the spectrum of the xenon lamp) and was not present in the spectrum of aluminium. However, this peak did not appear in the back face measurements, even though acrylic is transparent above 390 nm. This disappearance could be due to less light collection after changing the position of the sample. All the following spectra shown here were measured in the front face configuration.

Figure 2.26 shows the spectra of RPT acrylic measured with different filters. The peak that appears in the upper left plot at approximately 445 nm does not appear in the measurements of the bottom left plot, which were done with another emission filter. Therefore, this peak is not from the fluorescence of the sample and might be related to the filter. The peak observed in the bottom left plot may also be related to the filter, since it also appears in the measurements of glass and aluminium done with the same filter.

The peak shown in the bottom right plot, at around 395 nm, is not explained by stray light (see xenon flash lamp spectrum in the same plot). This peak does not appear in the spectra of glass and aluminium and is the same observed in Figure 2.25. The wavelength range of this peak is partially in the sensitive region of DEAP. The peak only appears for some excitation wavelengths (the highest intensity occurs when the sample is excited with approximately

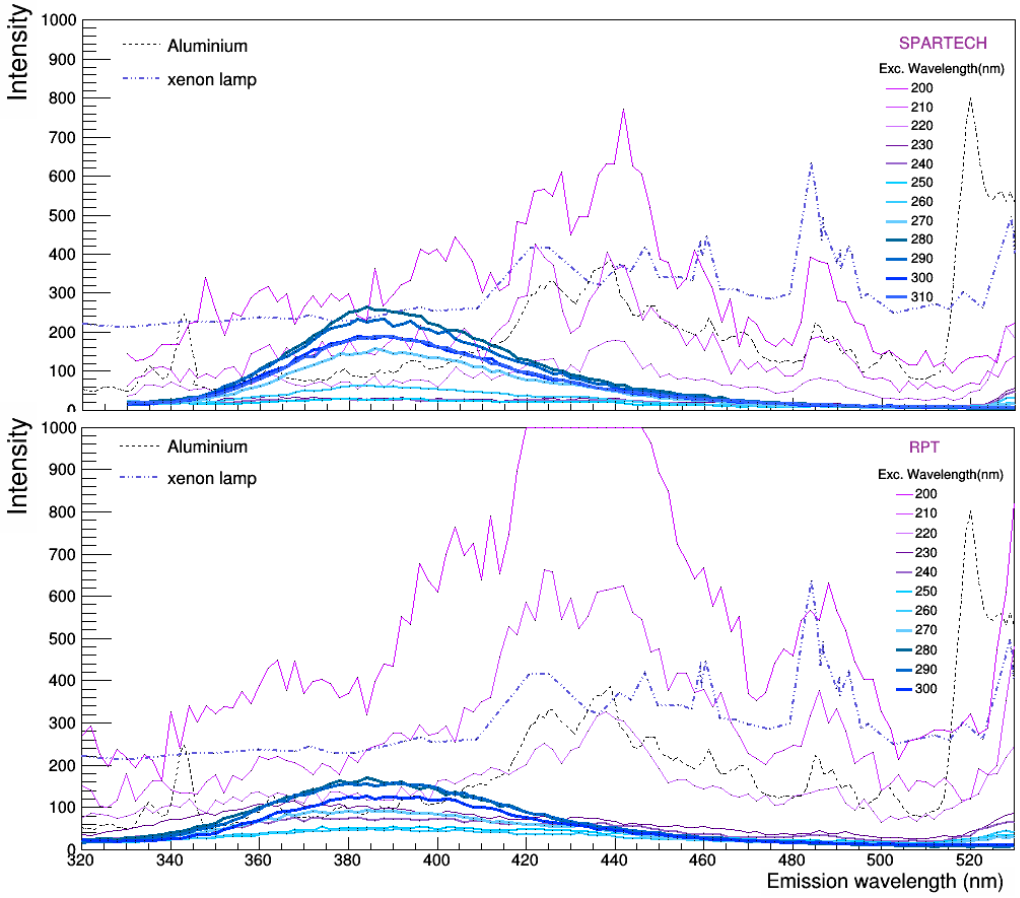

FIGURE 2.25: Upper plot: Front face fluorescence measurements of Spartech acrylic for excitation wavelengths from 200 nm to 310 nm (without filters). Bottom: Fluorescence measurements of RPT acrylic using the same settings described above. Also shown in both plots are the measurements of an Aluminium sample and the spectrum of a xenon lamp.

280 nm light). The other peak observed in the same plot, at approximately 430 nm, partially appears in the measurements of aluminium. This peaks is also observed in the spectrum of the xenon lamp, as shown in Figure 2.28, and in the spectra of the sandpaper, as shown in Figure 2.27. Therefore, it is not coming from the fluorescence of the acrylic sample.

The fluorescence measurements of the Spartech acrylic sample are shown in Figure 2.28 and are very similar to the measurements of RPT acrylic. The results of the samples with bond and the SNO acrylic sample are also very similar and are not shown here.

The measurements the rough RPT sample are shown in Figure 2.29. They slightly differ from the previous results of smooth RPT and Spartech (Figure 2.26 and Figure 2.28). The shape of the peaks of the measurements with filters seem to be distorted and the peak of the measurement without filters almost disappeared, being much smaller than the peak at

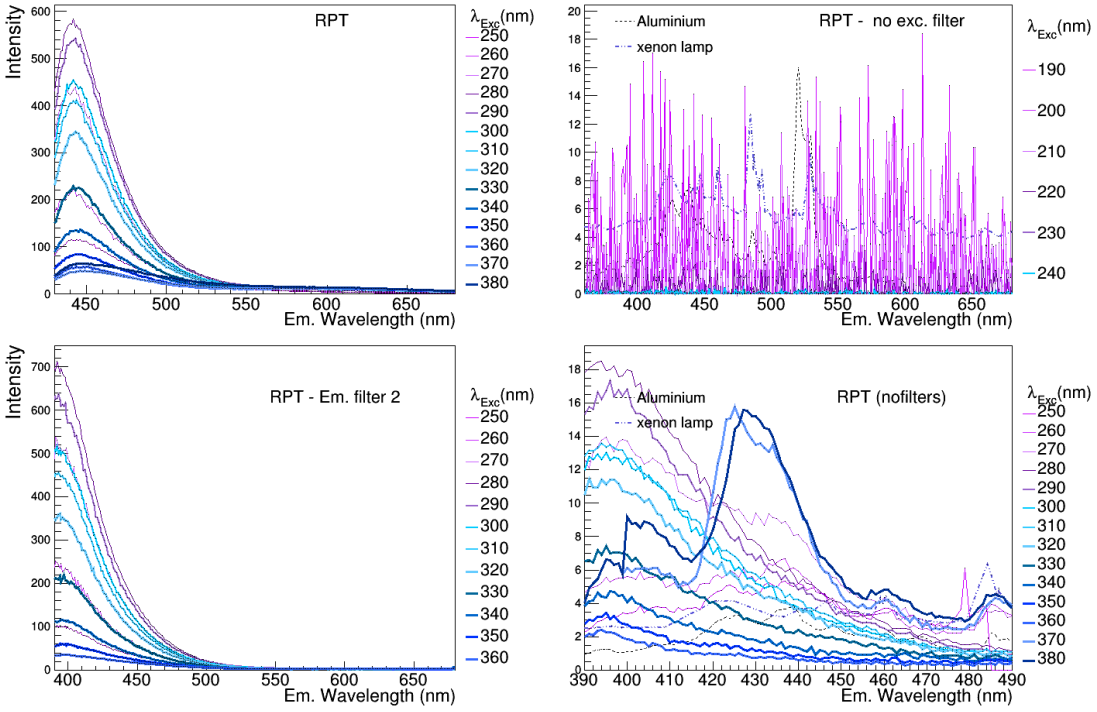

FIGURE 2.26: Fluorescence emission spectra of the RPT acrylic sample. Upper left: These measurements were done with the 250-395 nm exc. filter and the 430-1100 nm emission filter. The exc. and the em. slits were both 20 nm open. Upper right: no exc. filter and the 360 nm to 1100 nm emission filter. Slits 2.5-2.5 nm. Bottom left:250-395 nm exc. filter and 360 nm to 1100 nm emission filter. Slits 20-10 nm. Bottom right: no filters. Slits 10-5 nm.

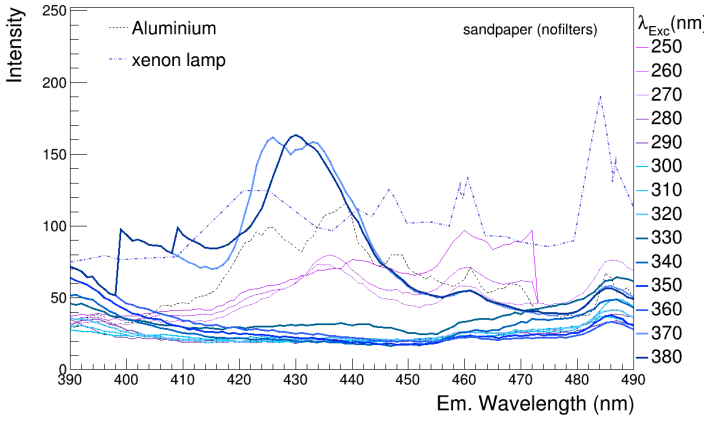

FIGURE 2.27: Measurements of the sand paper done without filters. Excitation slit was 10 nm open and emission slit was 5 nm open.

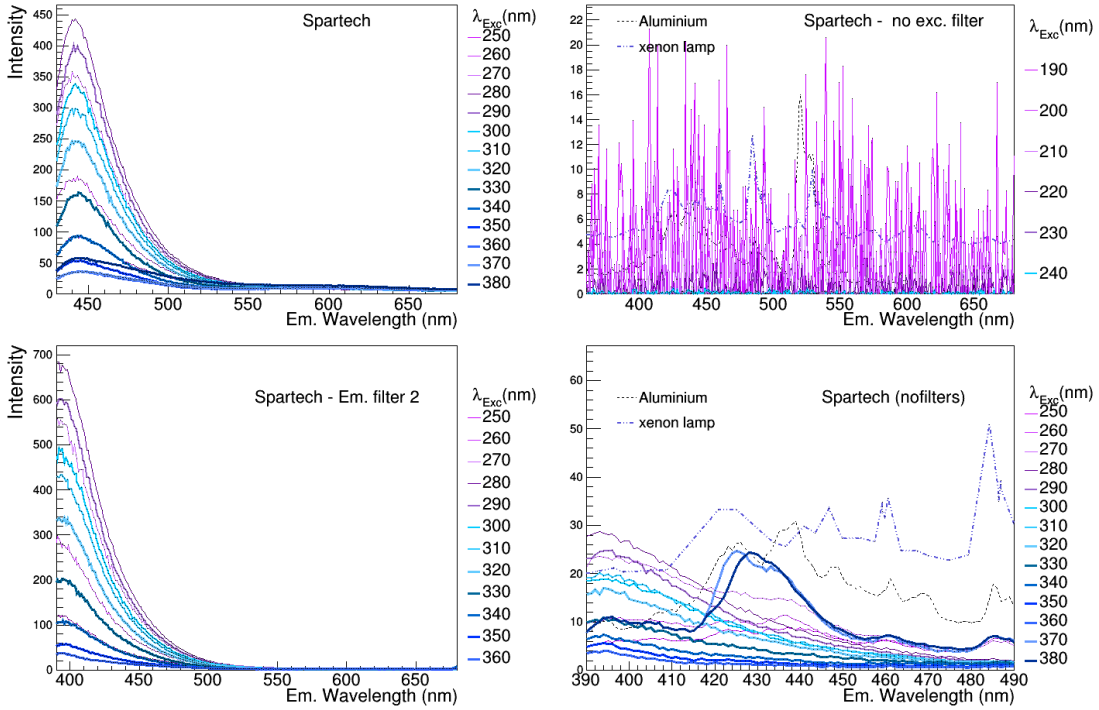

FIGURE 2.28: Fluorescence emission spectra of a Spartech acrylic sample measured with different filters and excitation/emission wavelength ranges. Upper left: These measurements were done with the 250-395 nm exc. filter and the 430-1100 nm em. filter. The exc. and the em. slits were both 20 nm open. Upper right: no exc. filter and the 360 nm to 1100 nm em. filter. Slits 2.5-2.5 nm. Bottom left: 250-395 nm exc. filter and 360 nm to 1100 nm emission filter. Slits 20-10 nm. Bottom right: no filters. Slits 10-5 nm

approximately 425 nm. The intensity of this peak for the rough Spartech also decreased, as shown in Figure 2.30. This difference could be due to the fluorescence of some superficial contamination which was decreased by the process of sanding.

In general, the measurements without excitation filter (upper right plots) showed that the sensitivity of the Cary Eclipse spectrophotometer is strongly constrained by stray light for measurements with excitation wavelength below 250 nm, for which there are no excitation filters.

The fluorescence emission spectra of the TPB reference sample are shown in Figure 2.31 and Figure 2.32. Figure 2.32 shows the spectra taken without exc. filter, which are noisy due to stray light. The spectra of Figure 2.31 show that if there is any fluorescence from the filters, its level is very low, compared to the fluorescence of TPB, since none of the peaks

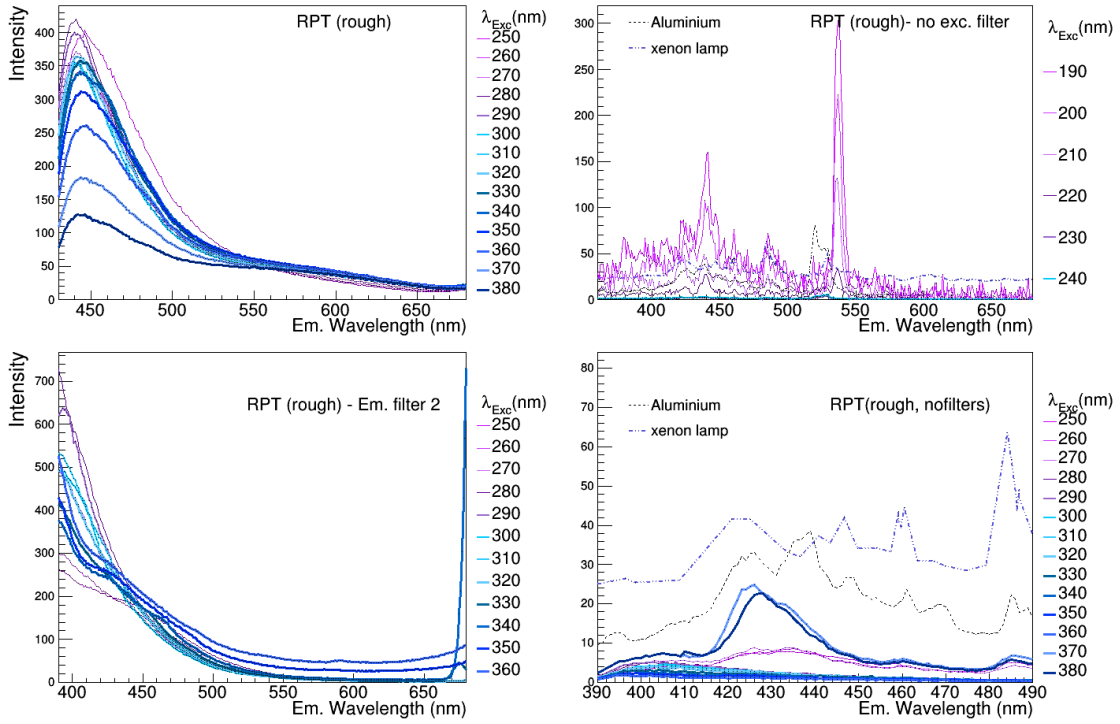

FIGURE 2.29: Fluorescence emission spectra of the rough RPT acrylic sample measured with different filters and excitation/emission wavelength ranges. Upper left: These measurements were done with the 250-395 nm exc. filter and the 430-1100 nm em. filter. The exc. slit was 20 nm open and the em. slit was 10 nm open. Upper right: no exc. filter and 360 nm to 1100 nm em. filter. Slits 2.5-2.5 nm . Bottom left: 250-395 nm exc. filter and 360 nm to 1100 nm emission filter. Slits 10-10 nm. Bottom right: no filters. Slits 10-5 nm

that appeared in the previous measurements with filters has appeared in the measurement of TPB. Note that the slits are only 2.5 nm open for the measurements of TPB.

2.4.3.2 Relative photon yield

The relative photon yield is calculated for each excitation wavelength by dividing the integrated spectrum obtained in the measurements of acrylic by the integrated emission spectrum of TPB. Here, again, relative photon yield means the relative amount of light detected in the measurements. The spectra were integrated from 390 nm to 680 nm, which is the region of interest of these measurements (based on the sensitivity of the photodetection system used in DEAP). In order to avoid the integration of the peaks attributed to the fluorescence of the filters, the range of integration of the spectra from acrylic was divided in two: From 390 nm to 490 nm, the spectrum measured without filters was integrated; from 490 nm to

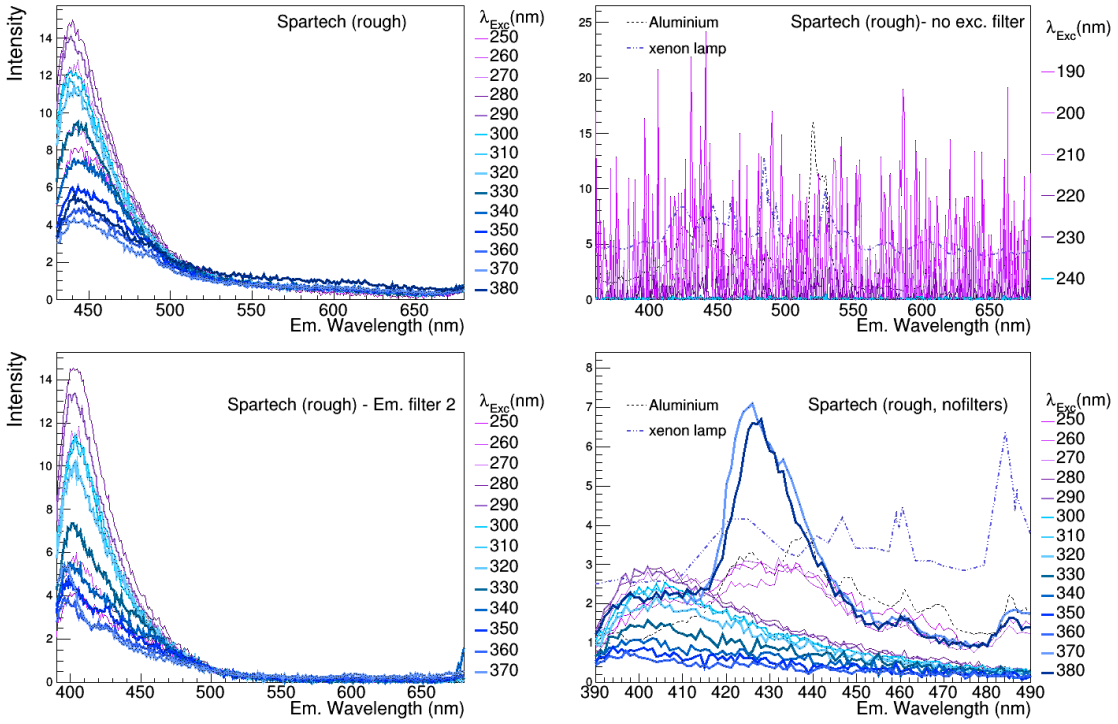

FIGURE 2.30: Fluorescence emission spectra of the rough Spartech acrylic sample measured with different filters and excitation/emission wavelength ranges. Upper left: These measurements were done with the 250-395 nm exc. filter and the 430-1100 nm em. filter. The exc. slit was 20 nm open and the em. slit was 10 nm open. Upper right: no exc. filter and 360 nm to 1100 nm emission filter. Slits 2.5-2.5 nm open. Bottom left: 250-395 nm exc. filter and 360 nm to 1100 nm emission filter. Slits 10-10 nm. Bottom right: no filters. Slits 10-5 nm.

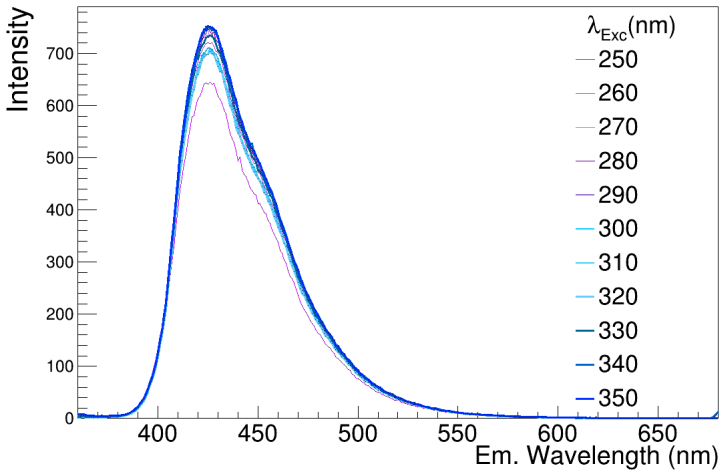

FIGURE 2.31: Fluorescence spectra of TPB (sample 1) for the excitation wavelengths from 250 nm to 350 nm. These measurements were done with an exc. filter 250-395 nm and an emission filter of range 360 nm to 1100 nm. Both slits were 2.5 nm open.

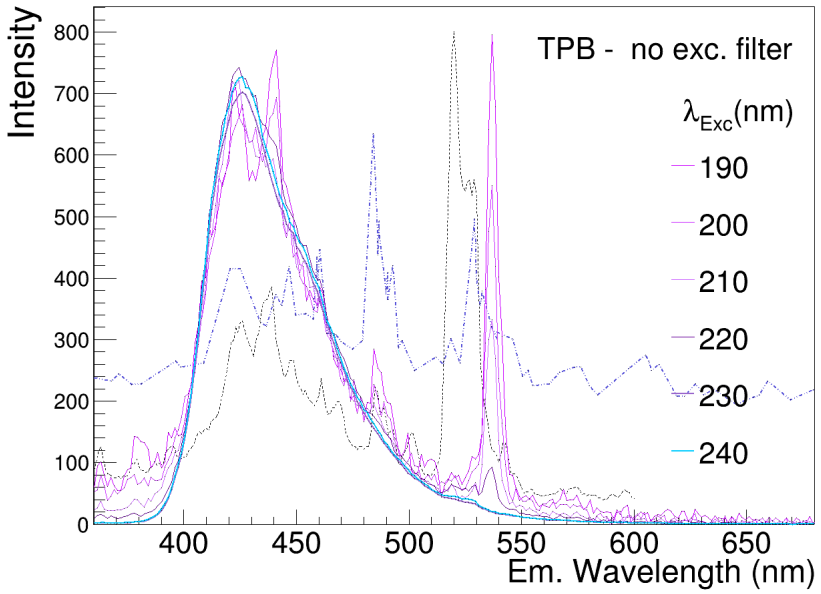

FIGURE 2.32: Fluorescence spectra of a TPB (sample 1) for the excitation wavelengths from 190 nm to 240 nm. These measurements were done without any exc. filter and with an emission filter of range 360 nm to 1100 nm. Both slits were 2.5 nm open.

680 nm, the spectra measured with the 360 nm to 1100 nm exc. filter were integrated. Note that the measurements without filters were not done for wavelengths above 490 nm because of second order peaks. Following the integration, the values were corrected for the slit width, as explained Subsection 2.4.2.2. The results are shown in the next subsection.

2.4.4 Results

The relative photon yield is shown in Figure 2.33. No error bars were calculated, since the uncertainty in the extrapolation of the relation between slit width and light yield could not be assessed, as described in Subsection 2.4.2.2. These results are not limits on the fluorescence of acrylic relative to TPB. They are rather an estimate of the sensitivity of the Cary Eclipse spectrophotometer to low-level fluorescence and an estimate of at which level the light yield of acrylic was tested. All the estimated values for excitation light from 230 nm to 360 nm are below 1.2% and most of them are below 0.4%. In addition to the uncertainty in the relation between slit width and light yield, other sources of uncertainties in these measurements were: the geometry, as described in Subsection 2.4.2, possible fluorescence of the filters, and stray light.

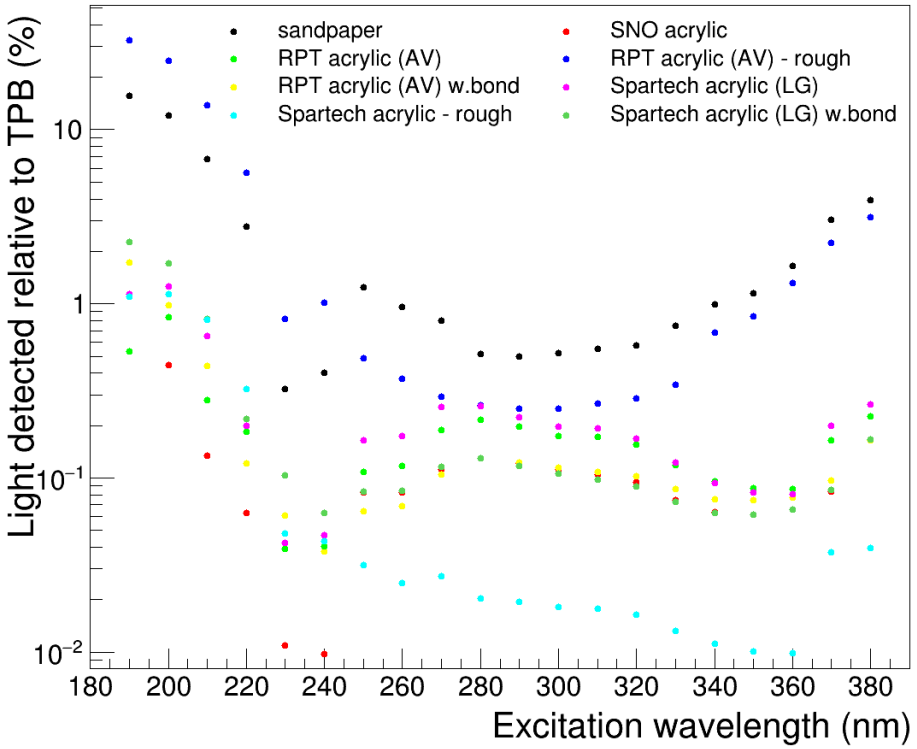

FIGURE 2.33: Estimates of the level at which the fluorescence of acrylic was tested relative to the fluorescence yield of TPB.

No clear fluorescence emitted by acrylic was measured. The only peak, among the noise, which could not be explained by either stray light or fluorescence of the filters, was the broad 385 nm peak shown in Figure 2.25. This peak was observed only in the emission spectra of the acrylic samples and not in the spectra of the glass and aluminium reference samples. The excitation wavelengths for which this peak presents the highest intensity also matches the ones for which the measurements with the VUV setup presented the highest values. More measurements with a different setup and at low temperature were therefore done. They are described in the next chapter.

Chapter 3

Fluorescence response of acrylic (PMMA) to UV light at temperatures from 300 K to 4 K.

The main objective of these measurements is to set limits on the efficiency at which acrylic, compared to TPB, shifts UV light to the visible range when cooled to LAr temperature.

These measurements also aim to determine whether the wavelength shifting efficiency of the acrylic sample is dependent on the temperature. In case the acrylic sample fluoresces, its re-emission could increase at lower temperatures, since thermal non-radiative transitions would be suppressed. To better assess the dependence on temperature, the response of acrylic and TPB were measured down to 4 K.

These measurements were done with an optical cryostat at Queen's University as a joint effort from DEAP collaborators to characterize the fluorescence of acrylic.

3.1 Setup

The idea of this setup is to cool down the samples to temperatures between room temperature and 4 K, excite them with UV light at a number of specific temperatures, and observe the

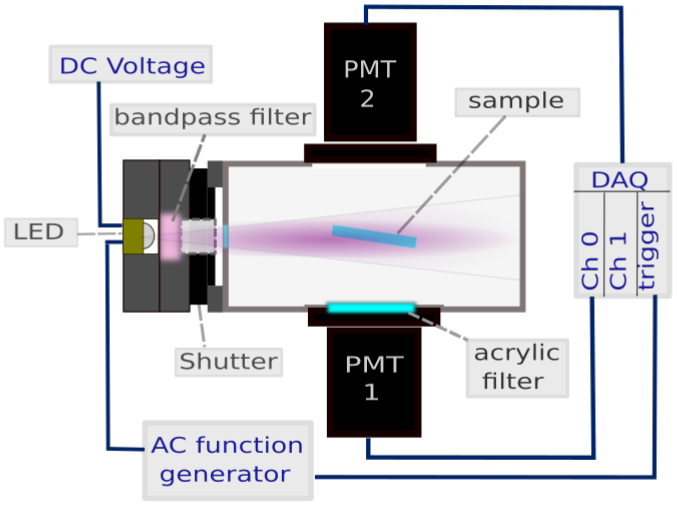

FIGURE 3.1: Schematic of the setup. Only the external chamber of the cryostat is shown, with the PMTs coupled to the large windows and the LED-filter set coupled to the shutter on the side. See text for details.

possible fluorescence response with a photodetector. A schematic of the setup is shown in Figure 3.1.

The samples are cooled inside a closed-cycle cryostat (shown in Figure 3.2), which is composed of three nested chambers that are cooled by a helium compressor. The inside of the cryostat can be viewed from four sides through fused silica windows, which have nominal transmission above 90% between 200 nm to 1000 nm [98]. Two photodetectors view the inside of the cryostat from opposite sides. They are R6095 bialkali and super bialkali Hamamatsu PMTs. A 280 nm LED from Roithner Lasertechnik GmbH, together with a bandpass filter, are attached to a third window. An LED-filter holder was made to steadily attach the LED and filter to a shutter, an then to the cryostat, as shown in Figure 3.1.

To place the samples inside the cryostat and ensure that the geometry (the position of the sample relative to the light source and PMTs) is always the same for both acrylic and reference samples, a sample holder was used. This sample holder was designed to fit the samples inside the cryostat, while minimizing how much the samples would have to be machined. A

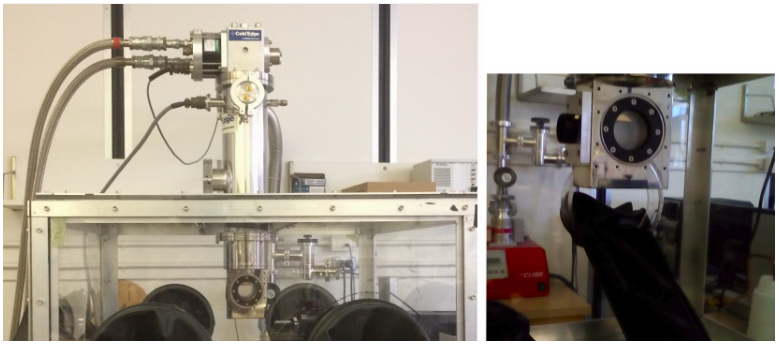

FIGURE 3.2: Left: Front view of the optical cryostat inside the glove box (Figure from [99]). Right: View of the large window and shutter on the side.

TPB sample placed in the sample holder inside the 4 K chamber is shown in Figure 3.3. The sample holder is at 8° from the axis of the LED and is open at the back part of the sample. Therefore, fluorescence light emitted in the visible region can be seen by both PMTs, as shown in Figure 3.1.

FIGURE 3.3: Front and side view of the sample and sample holder inside the 4 K chamber.

The spectral response of the bialkali PMT (PMT-2 in the schematic) is from 300 nm to 650 nm [100], which is similar to the ones used in DEAP. The spectral response of the super bialkali PMT (PMT-1 in the schematic) may be similar[1]. Yet, an acrylic filter was placed in front of this PMT (inside a sleeve) to filter out possible reflected 280 nm light. The transmittance of the acrylic filter was measured with a UV-Vis Perkin Elmer spectrophotometer and is shown in Figure 3.4. Even though the filter presents a bump in the transmittance at approximately 270 nm, it filters out most of the 280 nm light. The PMT-1 covers approximately 8% of the

[1]The datasheet of this PMT was not found.

solid angle and the PMT-2 covers slightly more, since there is no filter between the window and the PMT.

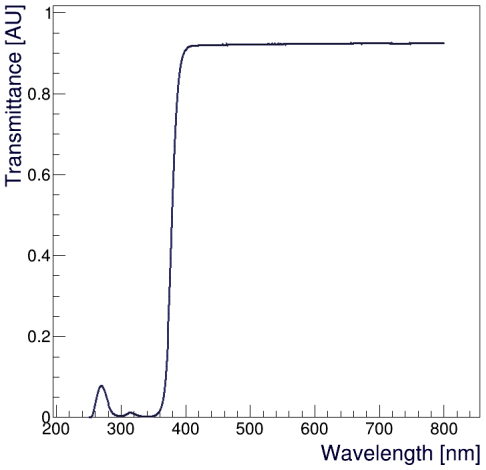

FIGURE 3.4: Transmittance of the acrylic filter coupled to the PMT-1.

The light output of the LED peaks at 280 nm, but it also presents a visible broad component. To filter out this component, a 280 nm bandpass filter from Edmund Optics with a FWHM of approximately 10 nm and transmittance above 50% at 280 nm was used. The LED was used in a pulsing mode. For this purpose, a pulser based on the circuit of reference [101] was used. This pulser has a nominal rise time and pulse width of only a few ns. The LED pulser is fed with DC voltage and an AC square signal from an Agilent function generator. This pulse also triggers the data aquisition (DAQ), as shown in Figure 3.1. The outputs of both PMTs are read by a PXI digitizer from National Instruments. A LabView program is used to read the data and set the time length of an event and its trigger conditions.

3.2 Procedures

The samples were placed in the sample holder inside the cryostat, at an angle of incidence of 82°. Then, we closed the cryostat and turned the vacuum pump on. After the pressure in the cryostat reached 10^{-5}mbar, the compressor, the PMT and the voltage output of the LED were turned on. We set the temperature in the cryostat with a temperature controller. Measurements started after the target temperature was reached and was stable within ±0.5 K. The samples were measured at these temperatures (K): 300, 250, 210, 163 (LXe), 120, 100,

87 (LAr), 77, 50, 20, 10, 6, 4. At the time a measurement started, the PMT and LED were already on for at least 2 hours. As an investigation of the stability of the setup (mainly of the LED), measurements at RT (290 K to 300 K) were done at the beginning and at the end of the measurements.

To allow for direct comparison between the acrylic and the reference, the settings of the pulsed LED, PMT and DAQ were the same for all the measurements. The PMTs operated in photon-counting mode with a voltage of 1250 V, provided by a CAEN N1470 high voltage power supply. The DC voltage of the LED pulser was 16.3 V and the AC square signals were generated with a frequency of 50 Hz and a peak to peak amplitude of 3 V. The data acquisition was triggered synchronous to the LED by a square function. A pretrigger of 10% of the event window was used. Each event was recorded for 10 µs and 45000 to 112500 events were recorded at each temperature. Both the reduced data (calculated by the online analysis of the LabView software) and the raw traces were saved for an offline analysis. The pulse finding threshold of the online analysis was set as 4 standard deviations above the average baseline. This threshold is less than 6% of the average amplitude of a single photoelectron pulse (see Section B.1 for details).

After the LED was turned on, it was kept on all the time until all the measurements were finished. The degradation of the sample due to exposure to UV light is negligible, since the frequency of the LED is 50 Hz and the pulse time is less than 5 ns. The measurement of each sample took approximately 5 days.

To investigate whether the setup was light-tight, the measurements of the dark rate of the PMTs were done inside a dark box and were then compared to the measurements of the PMTs in the setup with the LED off. The rates in both configurations were similar, proving that no ambient light was reaching the PMTs.

To ensure that the PMT was operating in photon-counting mode and that the pulse finder of the online analysis was identifying and integrating the pulses correctly, we did some tests with a pulsed visible LED and with the UV LED pulsing light on TPB at a low voltage. These tests are described in Appendix B, Section B.1. The spectrum of the pulses detected by the super bialkali PMT in these measurements is shown in Figure 3.5.

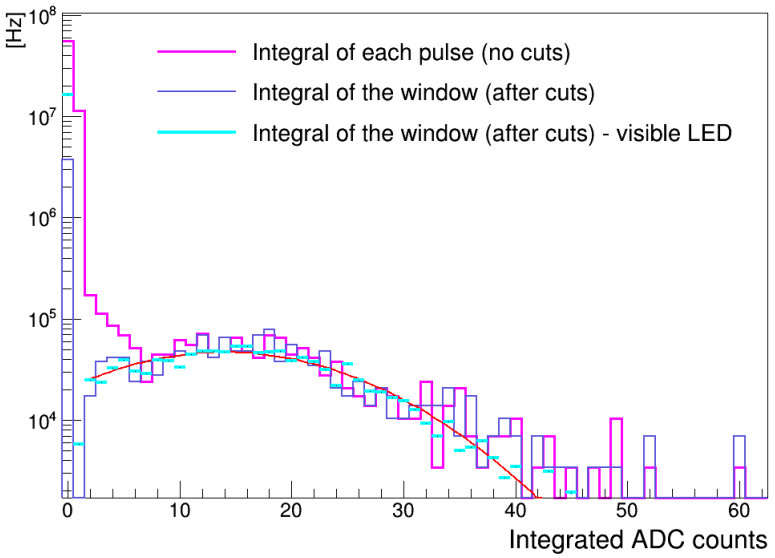

FIGURE 3.5: Single-photoelectron spectrum of the super bialkali R6095 Hamamatsu PMT when measuring fluorescence from TPB excited with single-photon pulsed UV light. Also shown are the gaussian fit and the spectrum obtained with pulsing a visible LED in single-photon mode.

The single-photoelectron peak obtained after removing the noise was fitted with a gaussian, with a mean at 13.99 (integrated ADC counts), which is the charge value equivalent to one photoelectron. The single-photoelectron spectrum obtained with the visible LED is also shown for comparison.

The measured samples are described below.

3.2.1 Samples

A disc of the RPT acrylic (described in Section 2.2) was cut[2] and then sanded with the same sandpaper used in DEAP (see Section 2.2 for more details). After sanding, the sample was sonicated in isopropanol, sonicated in distilled water, and dried with a nitrogen gun.

The TPB reference sample was newly vacuum evaporated on a sanded piece of acrylic. Its thickness was approximately 0.4 µm, which was measured with a profilometer. Its fluorescence emission spectrum was measured with the Cary Eclipse spectrophotometer described in Subsection 2.4.1. The spectra measured with excitation light from 250 nm to 355 nm are shown in Figure 3.6, together with the spectra of the TPB reference from Section 2.3, which

[2] with a machine that does not use oils and without touching the front surface of the sample.

consisted of a 1.2 µm TPB layer vacuum evaporated on glass. The integrals of the spectra measured with 280 nm excitation light are compared. The comparison showed that the WLSE of the new sample is 78±8% of that of the old sample. The uncertainty comes from the dependence of the WLSE on the angle of incidence.

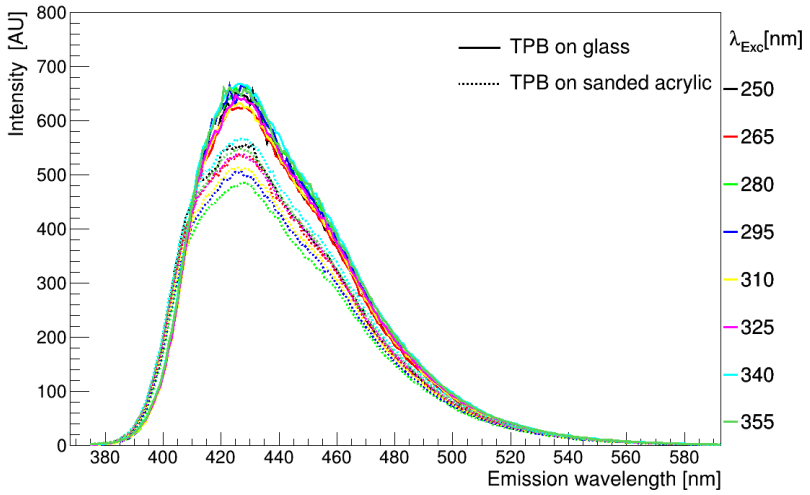

FIGURE 3.6: Fluorescence emission spectra of TPB evaporated on glass (ref. sample of Section 2.3), and of TPB evaporated on sanded acrylic. The spectra were measured with excitation light from 250 nm to 355 nm.

3.3 Data analysis

As in the previous chapter, the goal is to compare the light intensity detected from the acrylic to that detected from the TPB sample. The light intensity is determined by summing the charge of the pulses detected by the PMT-1 within a short (or long) window around the time the LED is fired. The charge sum is normalized to the number of LED flashes and corrected for the acceptance of cuts, before the comparison between samples.

The online analysis implemented in the DAQ LabView software calculates the charge integral of each pulse of an event. First, it calculates the mean value of the baseline in each event (using the 10% pretrigger fraction) and its standard deviation. Then, it sums the amplitudes of samples that are 4 standard deviations above the mean baseline and corrects it for the baseline. In order to ensure that the analysis threshold is the same for all the measurements, the standard deviation of the baseline must be roughly constant. These values were analyzed and they vary less than 2%.

Within 4 standard deviations, one sample of the baseline in each 30000 will be above the threshold. Since the sample time is 0.4 ns/sample, a minimum pulse width of 2 ns is used to cut single samples that are above threshold. This is also used to cut the baseline noise generated by the pulser, which is described in the next subsection.

3.3.1 Baseline noise investigation

The pulser electronic is part of the same circuit board that provided the bias voltage to the PMT. Pulsing the UV LED was found to introduce noise to the baseline of the signal from the PMT that was not there when the pulser was turned off. As an investigation of this noise, measurements were taken with the same geometry as show in Figure 3.1, but with the shutter closed. In this configuration, photons from the LED could not reach the PMT, and only the additional electronics noise on the baseline was recorded. A trace of the noise is shown in Figure 3.7.

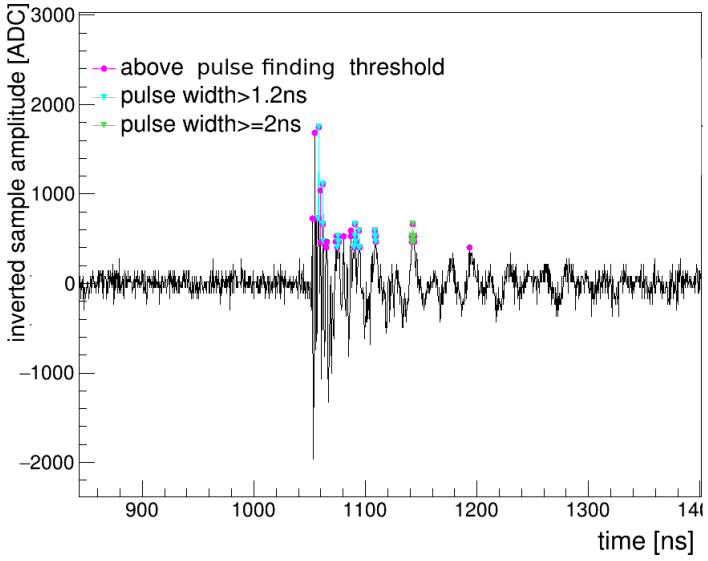

FIGURE 3.7: Trace of the baseline noise produced when the UV LED is pulsed and the shutter is closed. The points in magenta show the samples above the pulse finding threshold. The other points show the samples that additionally pass minimum pulse width cuts.

The amplitude of the electronic noise induced by the pulser is above the pulse finding threshold. The pulse finder of the online analysis therefore cannot distinguish between the noise and a pulse. This noise is thus cut in an offline analysis. Figure 3.7 suggests that most of the noise can be cut by requiring a pulse to have a minimum width of 2 ns, if the noise has always the same shape. This was further investigated and is shown in Figure 3.8. In this

figure, we see that: i) the baseline noise is constant, that is, its shape does not change for different runs; and ii) the noise that survives the pulse width cut (>=2 ns) has an average amplitude only slightly above the pulse finding threshold, which is approximately 400 ADC. Therefore, the mean amplitude of this noise summed to 4 standard deviations will be used as an extra threshold cut: To be considered a pulse, the maximum amplitude of the pulse must be higher than this new threshold value. The leakage of this cut, that is, noise being considered as a pulse is less than 0.01%.

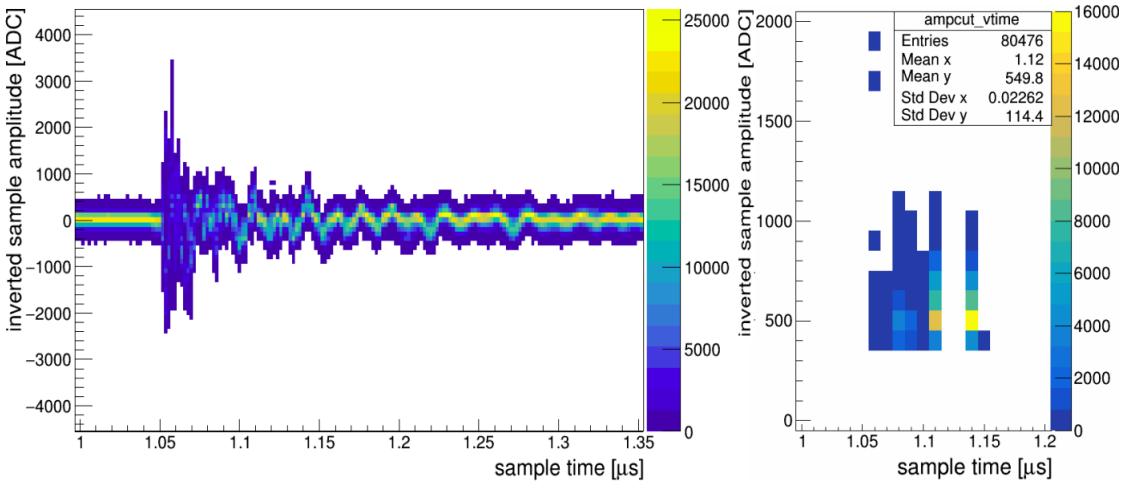

FIGURE 3.8: Left: 2D histogram of the baseline noise traces (amplitude vs. time) for 15000 events taken from 3 noise runs. Right: 2D histogram of the noise that survives the pulse width cut (>=2 ns).

The acceptance of the cut was calculated by analyzing the data taken using the pulsed visible LED. The noise in this data is almost negligible, since the voltage necessary to pulse the visible LED is much lower (approximately 4.5V). By applying this maximum amplitude threshold cut to the data, the total charge integral decreased by only 0.16%, that is, the acceptance of the cut is 99.84%.

Furthermore, the noise does not contribute significantly to the integrated charge of the pulses, since the noise with higher amplitude happens before the fluorescence pulses and the noise that happens in the time window of the pulses averages out to zero. More details on how the cuts affect the data are given in Appendix B, Section B.2.

3.3.2 Integration window

The recorded time of each event was 10 µs and the LED was fired 1 µs after the beginning of the event. The pulse arrival time distributions from TPB and RPT acrylic measured at 300 K are show in Figure 3.9. These distributions do not significantly change with temperature. Therefore the data at 300 K is taken as a representative sample (see Section B.2 for more details). The distributions are shown before (in magenta) and after applying the cuts (in gray or black). Note that the distributions measured for RPT before cuts are mostly baseline noise.

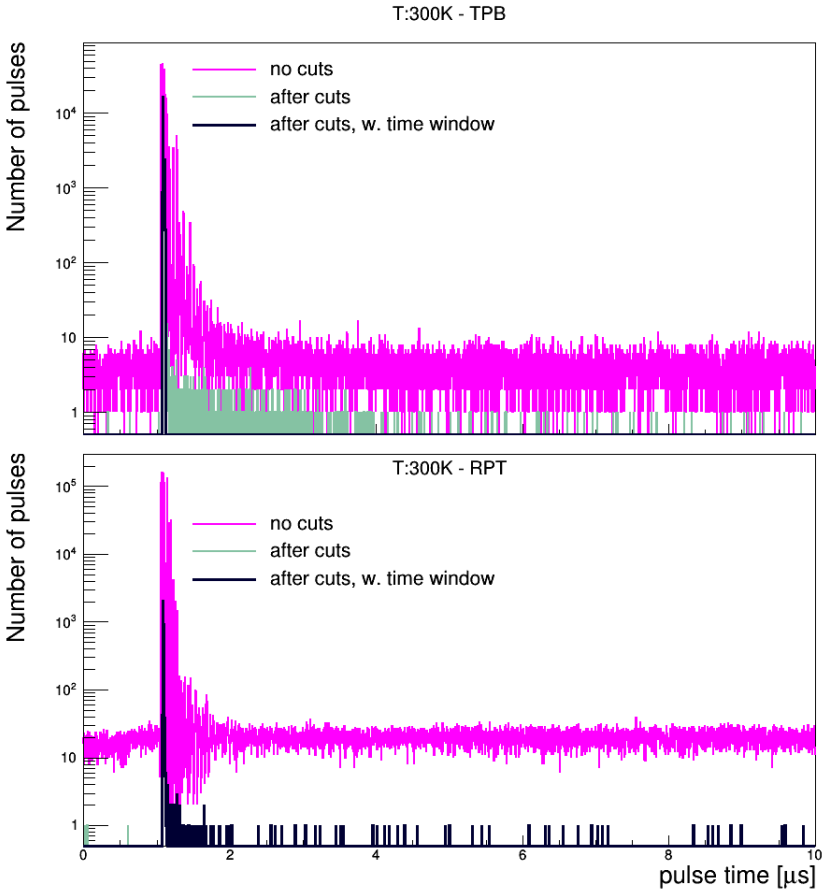

FIGURE 3.9: Arrival time distributions of the pulses detected in the measurements of TPB (45000 events) and RPT acrylic (112500 events) at 300 K. All the pulses identified by the pulse finder of the online analysis are shown in magenta. In gray, only the ones that pass the cuts are shown. In black (overlaying the one in gray) are the pulses that pass the cuts and are within the integration window (50 ns after pretrigger for TPB and the entire window after the pretrigger for RPT).

More than 98% of the pulses from TPB arrive in the first 50 ns after the pretrigger time[3].

[3]Pretrigger time was considered to be 1.07 µs, since no pulse arrives before that.

This is shown by the black line in the upper plot of Figure 3.9. The decay time of the fluorescence emission by TPB is a few nanoseconds [102]. However, there is also evidence of long-lived states of TPB, which lead to a low-intensity tail toward longer times (of the order of microseconds) [103]. Therefore, pulses that arrive later could be delayed photons from TPB (in addition to afterpulsing and a few dark counts). It is, however, unclear whether 280 nm light is able to induce the delayed florescence of TPB. Reference [103] states that the delayed component might be related to the ionization of TPB by VUV light, and says that the ionization potential of TPB is not known. To better understand the decay components of TPB, an average pulse of TPB measured at 87 K was fit from 1 µs to 5 µs with two exponential functions: one with a short decay constant and one with a longer constant. This is shown in Figure 3.10.

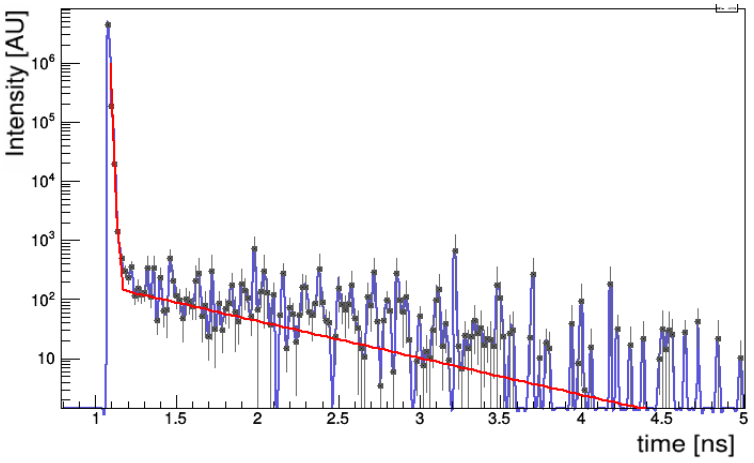

FIGURE 3.10: Average pulse (average intensity of light detected vs. time) of TPB fit by two exponential functions. Fit parameters are described in Appendix B.

More details on the rise time of the pulser and the afterpulsing of the PMT would be necessary to decouple the decay constants of TPB from the features of the PMT and LED pulser. Therefore, the light yield by TPB will be integrated only for the first 50 ns after the pretrigger time, since it leads to more conservative limits on the relative photon yield.

Figure 3.9 shows that most of the pulses from the measurements of RPT acrylic are detected right after the pretrigger time. The decay time of the possible fluorescence light emitted by acrylic should be of the order of nanoseconds, given that acrylic has been reported to fluoresce and not phosphoresce. The late pulses can be either dark counts or afterpulsing. To obtain the light detected in the measurements of acrylic, the time window will be integrated for

both 50 ns and approximately 9 µs after the pretrigger time. For all the measurements, the 1 µs pretrigger window will be used to measure the dark counts.

3.3.3 Relative photon yield

The pulses that passed all the cuts and occurred within the integration window were integrated. The distribution of the integrated ADC counts for the TPB sample measured at different temperatures is shown in Figure 3.11. The average of the distribution is at approximately 100 integrated ADC counts, which represents an average of 7 photoelectrons per event. Figure 3.12 shows the 87 K TPB data from Figure 3.11 (normalized for the number of events) together with the corresponding data for the RPT acrylic sample. In the measurements of acrylic only approximately 10% of the events have a pulse, and most pulses are of single photoelectron size.

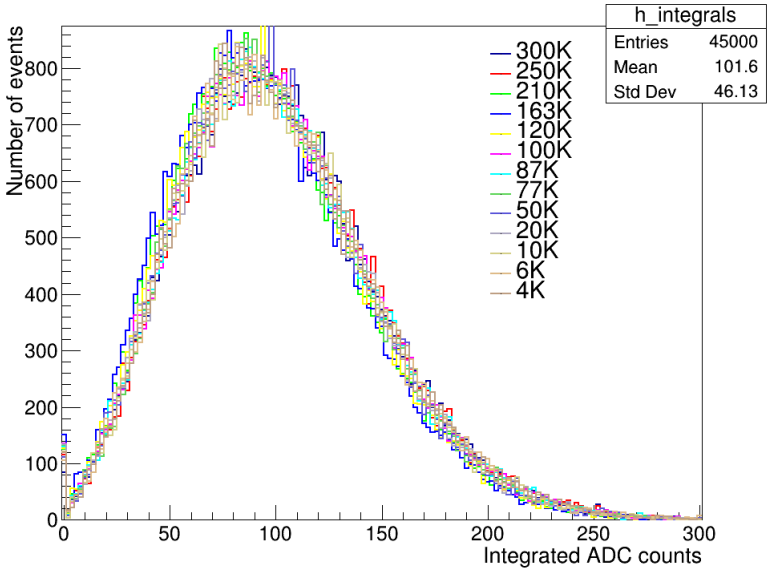

FIGURE 3.11: Integrated ADC counts of the measurements of TPB. Each histogram shows the integrals of 45000 events measured at a different temperature.

The number of dark counts expected for each integration window (50 ns for TPB and 9 µs for RPT) is low (the dark rate is approximately 100 Hz). It represents less than 1% of the light detected in the measurements of acrylic and is close to zero in the measurements of TPB. Therefore, the measured charge integrals will not be corrected for the dark rate.

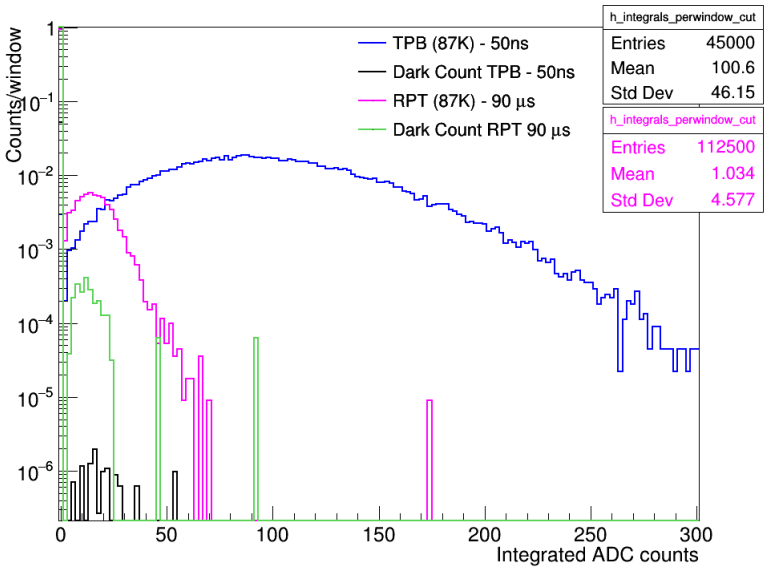

FIGURE 3.12: Integrated ADC counts (after cuts) per event of: TPB (integration time of 50 ns) and RPT acrylic (integration time of 9 µs) measured at 87 K. Also shown are the dark counts during the measurements of TPB and RPT (scaled for the same integration times).

Figure 3.13 shows the average pulses of TPB and RPT acrylic at 4 different temperatures. The average pulses show how much light intensity is observed on average as a function of time. For the RPT sample, the typical light intensity at all times increases slightly toward lower temperatures. To better observe this increase, the average pulse at 300 K was subtracted from the average pulses at lower temperatures (210 K, 87 K and 4 K). The residuals are shown in Figure 3.14. The residual values above 1.2 µs (approximately 150 ns after pretrigger time) are statistical fluctuations. The inset shows that the increase of the light intensity at lower temperatures happens in the first hundred nanoseconds.

In order to determine the statistical uncertainty on the photon yield of the sample[4], the number of events was divided into 10 sets of measurements. The mean of each set of measurements was calculated and the uncertainty on the mean photon yield is the standard deviation of the 10 values. To assess the systematic uncertainty from the instability of the LED, measurements at RT were done at the beginning and at the end (5 days later) of one cryostat run. These measurements agree within one standard deviation (see more details in Section B.2). Therefore, no systematic error will be derived from the instability of the LED

[4]The term "photon yield" of a sample is used here in the same way it was used in the previous chapter: It does not imply that the measured samples fluoresce, but rather mean the amount of light detected while measuring them.

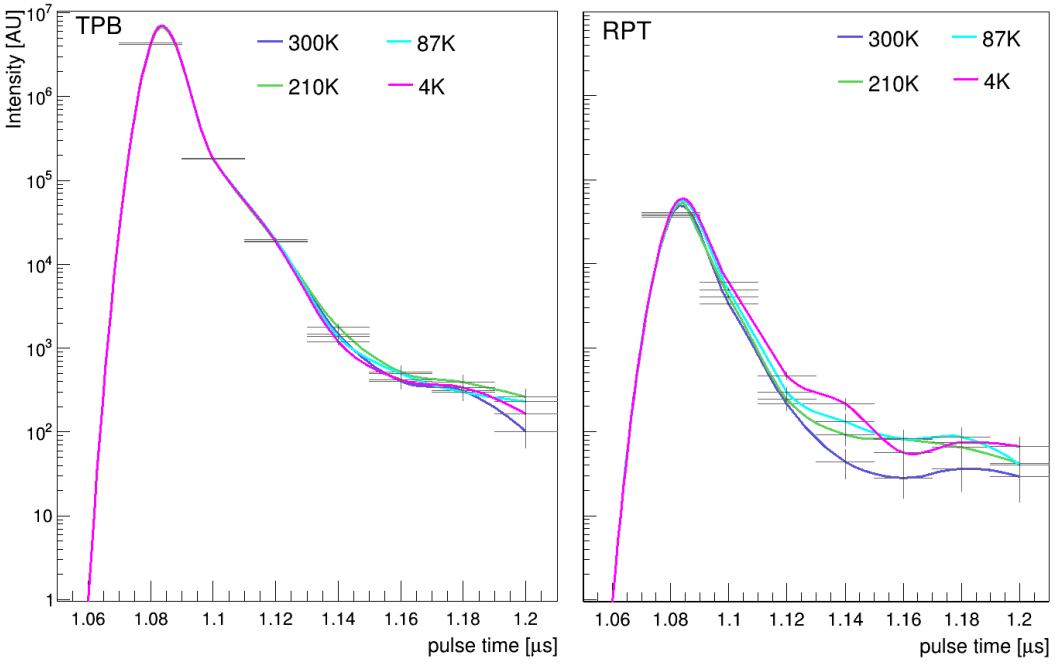

FIGURE 3.13: Average pulse (average intensity of light detected vs. time) of TPB and RPT acrylic zoomed in the first 140 ns after pretrigger.

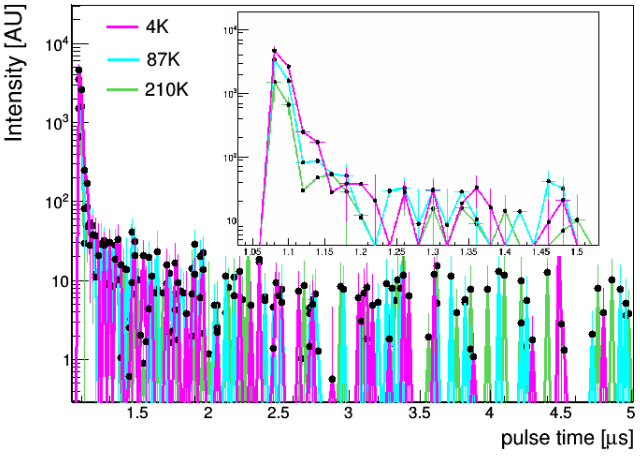

FIGURE 3.14: Residual average pulse of RPT acrylic measured at 210 K, 87 K and 4 K and subtracted by the average pulse measured at 300 K. The inset shows a zoom between 1 and 1.5 µs

or of the setup. The light detected in the measurements of RPT acrylic at different temperatures is shown in Figure 3.15. The increase of the light intensity toward lower temperatures is again evidenced.

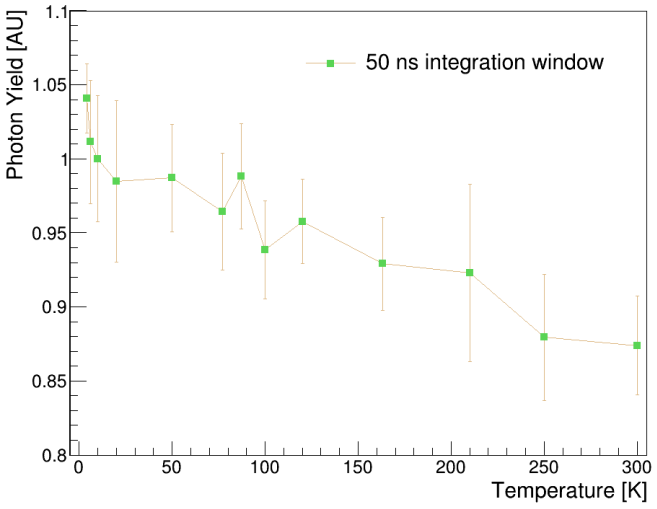

FIGURE 3.15: Photon yield of RPT acrylic (integration window of 50 ns) vs. temperature. The error bars show one sigma statistical uncertainty.

The mean values of photon yield are corrected for the acceptance of the maximum amplitude threshold cut and divided by the mean photon yield of TPB measured at the same temperature. The statistic errors are propagated. The photon yield in the measurements of RPT acrylic for integration times of 50 ns and 9 µs relative to the photon yield of TPB are shown in Figure 3.16.

To compare the relative photon yield at RT measured with this setup to the values previously measured with the VUV fluorescence setup (Section 2.3, Figure 2.12), the efficiency of the TPB sample used in these measurements was corrected for the efficiency of the TPB sample measured before (as described in Subsection 3.2.1). The errors on the correction were propagated and the resulting relative photon yield of the RPT acrylic rough sample at RT is 1.1232 ± 0.1207. The relative photon yield of the same sample previously measured at RT and with 280 nm excitation light was 0.4984 ± 0.0682. Since the surface of the sample is rough, the dependence on the angle of incidence is not strong (as also shown in Figure 2.12). Therefore, it is possible to compare the values of photon yield of acrylic in both measurements, and the value measured previously can be used to constrain the photon yield of RPT measured at RT with the setup of this chapter.

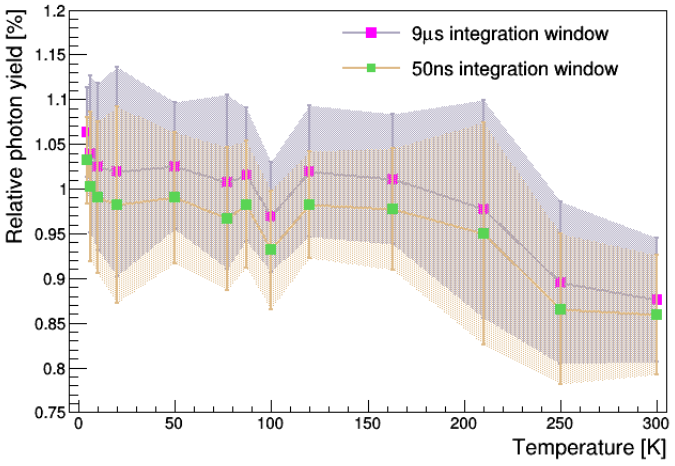

FIGURE 3.16: Photon yield of RPT acrylic relative to the photon yield of TPB [%] versus temperature. The values calculated by integrating the entire window are shown in magenta and the ones for the 50 ns window in green. Lines and shaded area are shown to guide the eyes through the measured data points and error bars.

The difference between the values of the previous chapter and the current one might be due to stray/reflected light and background fluorescence, since most of the light seen at RT with this setup might be: i) the visible component of the LED that is not absorbed by the bandpass filter[5]; ii) reflected 280 nm light that is not absorbed by the acrylic filter; and iii) background fluorescence of the 6 windows that are in between the LED and the PMT. Therefore, the difference between the values of relative photon yield at RT can be accounted for this background. The relative photon yield of RPT after correcting for this background is shown in Figure 3.17. The error bars include the statistic error of the measurements of both RPT and TPB, and the uncertainties on the correction of TPB's efficiency and on the background correction.

This background correction does not account for all the sources of background light described here. It only accounts for the background light that is in excess of the light observed in the previous measurement. Since the background fluorescence and stray light levels of this setup have not yet been well characterized and their level seem to be above the level of fluorescence expected from the sample, it is not possible to decouple the background light of the setup from the possible low-level of light emitted by acrylic. Therefore, the relative photon yield shown in Figure 3.17 and the two sigma uncertainty will be used to derive upper limits on the

[5]Measurements done by other collaborators from DEAP with the same setup showed that the bandpass filter (which was from the same manufacturer of the bandpass filter used in these measurements) did not fully eliminate the visible component of the LED.

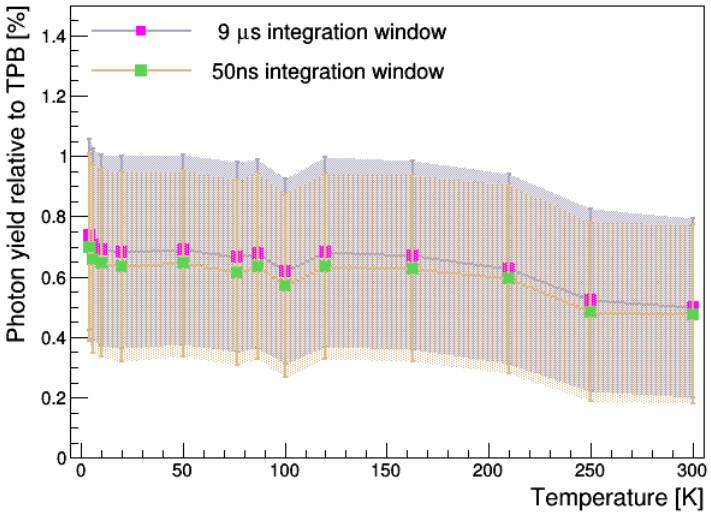

FIGURE 3.17: Photon yield of RPT acrylic relative to TPB [%] versus temperature (after corrections, see text for details). The values calculated by integrating the entire window are shown in magenta and the ones for the 50 ns window in green. Lines and shaded area are shown to guide the eyes through the measured data points and error bars.

WLSE of RPT acrylic relative to TPB. Although the relative photon yield calculated for the long integration window (9 µs) might include afterpulsing and dark counts, these values will be used to set the limits, since they include possible delayed fluorescence and are therefore more conservative. The limits are shown in the next section.

3.4 Results

Figure 3.18 shows the 95%CL upper limit on the WLSE of RPT acrylic relative to that of TPB for excitation with 280 nm light and at temperatures from 4 K to 300 K.

The limits on the WLSE increase toward lower temperatures because the light detected in the measurements of RPT acrylic increases toward lower temperatures, as shown in Figure 3.15. The same trend (increasing photon yield at low temperatures) was observed in the measurements after the compressor was turned off and while he cryostat was warming up (decreasing of photon yield at higher temperatures). The 95%CL limit on fluorescence of acrylic at LAr temperature is 0.99% of the fluorescence yield by TPB. These limits are valid for 280 nm excitation light and for an emission spectrum similar to the one of TPB, as described in Subsection 2.3.7. If the emission spectrum of TPB changes at lower temperatures, as described

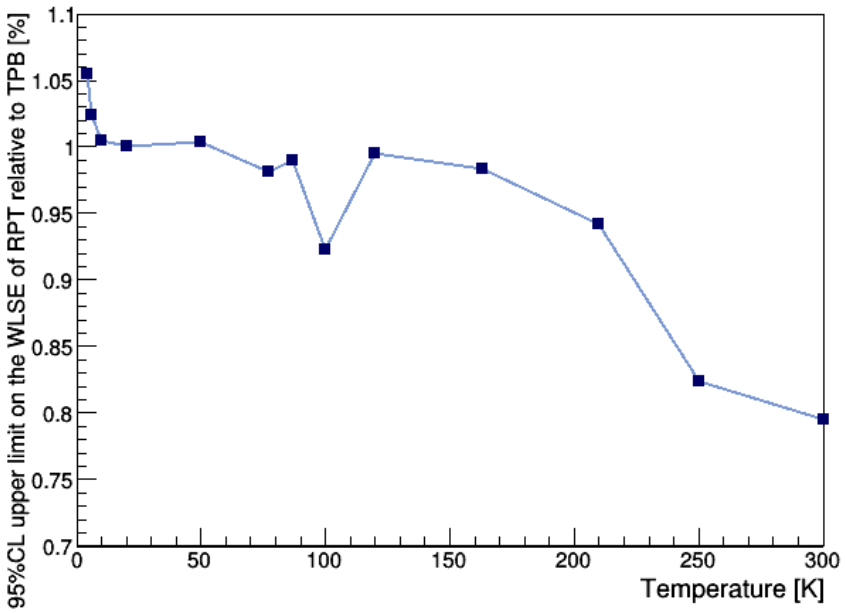

FIGURE 3.18: 95%CL upper limits on the wavelength shifting efficiency of RPT acrylic relative to TPB at different temperatures and excited with 280 nm light. See text for details.

in [104], the efficiency with which the PMT detects the light emitted by TPB can slightly change. Since the light detected in the measurements of TPB at different temperatures is constant within 3%, this did not seem to affect the measurements. Furthermore, the limits are directly comparable to the light yield in DEAP, since the spectral response of the PMT in DEAP (together with the acrylic vessel and light guides) is similar to the one of the PMT with the acrylic filter used in this setup.

3.5 Conclusion and discussion

The fluorescence of the RPT acrylic used in the acrylic cryostat of DEAP was tested at LAr temperature. At the sensivity of the setup, no photoluminescence from the acrylic sample was detected and a limit was therefore set on its wavelength shifting efficiency relative to that of TPB. When comparing the RT results presented in this chapter to the ones described in Section 2.3, we see that the VUV setup had better sensitivity at RT, although the intensity of the deuterium lamp was low at 280 nm. The lower sensitivity of the optical cryostat for these measurements could be attributed to stray light and the possible fluorescence of the windows of the cryostat. The level of stray light is determined by the ratio between the

transmitted visible light and the intensity of the selected wavelength (280 nm). This ratio seems to be higher for the LED with the bandpass filter than for the deuterium lamp with the monochromator. Background fluorescence of this setup was also probably higher than in the VUV setup, since the optical cryostat has a total of 6 windows between the LED and the PMT. Despite this, these measurements allowed limits on the WLSE of acrylic at LAr temperature to be set at a level better than 1% relative to TPB, and to measure the dependence of the WLSE of the RPT acrylic on the temperature, between 300 K and 4 K.

The WLSE of RPT acrylic seems to be related to the temperature, since the light detected increased at lower temperatures. This effect cannot be attributed to stray light or the fluorescence of the outer windows of the cryostat, since the LED and the outer chamber of the cryostat are always at RT. Another explanation for this increase could be the fluorescence of the window of the inner chamber, which is at the same temperature of the sample. A measurement of the empty cryostat, to check for this possibility, has been planned, but has not yet been accomplished due to time constraints.

As a continuation of the work of this thesis, time-resolved measurements of PTFE with the optical cryostat have been suggested and the VUV setup at TUM will be upgraded to cool down the samples to liquid nitrogen temperature, so that the wavelength range of the measurements at low temperature can be extended to the VUV.

Chapter 4

Relative wavelength shifting efficiency of polyethylene naphthalate

Polyethylene naphthalate (PEN) is a polymer with scintillating and wavelength shifting properties. Its scintillation yield was reported by [105] as comparable to the photon yield of organic scintillators. The current increasing interest of the scientific community in this plastic is not only because of its high scintillation yield, but also due to its emission in the visible (blue) spectral region, good mechanical properties, low radioactivity [106], easy availability and low cost compared to other scintillators and WLSs [105].

PEN has been proposed by [61] as a self-vetoing material to be used in the GERDA experiment and has been investigated, during the work done for this thesis, as a substitute of the wavelength shifter TPB in future LAr-based detectors. This investigation was done together with the other authors of [107], as a continuity of the work started by one of the authors.

PEN absorbs UV light and it is mostly transparent to visible light [108]. Its photoluminescence response to UV light was measured by [109] and [108]. The first reference showed that while the shape of the emission spectrum of PEN does not significantly change, its wavelength shifting efficiency increases at low temperatures (measured down to 93 K). Reference [108]

showed that the wavelength shifting efficiency of PEN (similarly to its absorption) increased at lower excitation wavelengths (measured down to 50 nm).

The increase in the WLSE of PEN at low temperatures and when excited with VUV light, together with its high scintillation photon yield, indicates that its efficiency in shifting 128 nm photons to the blue spectral region at LAr temperature might be high. However, none of the aforementioned references reported the absolute values of its WLSE or QE. That is, it is not yet known how efficient PEN is, compared to other well established WLSs.

Therefore, measurements of the WLSE of PEN relative to TPB were done with the setup described in Subsection 2.3.1. TPB is a suitable reference for these measurements because it is widely used as wavelength shifter in LAr-based experiments [8, 41, 50–53] - which allows for direct efficiency comparison - and its WLSE and QE are described in the literature [54, 110, 111].

Since the PEN sample is a plastic film and TPB is a powder, a rough PEN sample was measured in order to obtain relative WLSE results that depend less on possible differences in the angular distributions of light emitted by TPB and PEN. The samples are described in more details in the next section.

4.1 Samples

- TPB: A 1.2±0.2 µm layer of TPB vacuum evaporated on glass. See Section 2.2 for more details.
- PEN: A 125 µm thick film of PEN type Teonex R Q83, produced by Teijin DuPont Films. The sample was sonicated in isopropanol, then it was dried with a nitrogen gun, sonicated in distilled water and dried with a nitrogen gun again. For better comparison to the TPB sample evaporated on glass, the same type of glass was used behind the PEN sample during the measurements. The glass was sonicated in acetone, dried with a nitrogen gun, sonicated in isopropanol, and dried with a nitrogen gun.
- PEN rough: The same sample of PEN was sanded, cleaned again using the procedures used for the smooth sample and measured again (also with a glass plate).

4.2 Procedures and data analysis

The procedures are similar to the ones described in Subsection 2.3.4. The measurements were done under two angles of incidence (39.5° and 12.5°), and with the excitation wavelengths: 120 nm, 130 nm, 150 nm, 160 nm, 170 nm, 190 nm, 210 nm, 230 nm, 250 nm and 250 nm. The measurements were done with both photodetection assemblies of Subsection 2.3.1: The PMT with the acrylic filter was used for the wavelength-integrated measurement, and the Ocean Optics spectrometer was used for the wavelength-resolved measurement. Since the photon yield of PEN is much higher than that of the plastic samples from the previous chapters, the spectrometer can be used, in addition to the PMT, to obtain the photon yield of the sample relative to TPB.

In the wavelength-integrated measurements, the emission of both PEN and TPB are measured with the PMT and then compared: The relative photon yield and its uncertainty are obtained for each excitation wavelength as described in Subsection 2.3.6.2. These values are then corrected for the spectral response of the photodetection assembly. This correction is minor (approximately 1%), since the spectral response of the light detector (with filter) is mostly flat above 380 nm and the emission spectrum of PEN is very similar to the one of TPB.

In the wavelength-resolved measurement, the spectra of PEN and TPB are measured with the spectrometer. First, the spectra are corrected for the wavelength-dependent response of the spectrometer assembly. Then, the spectrum of PEN is integrated and divided by the integrated spectrum of TPB. This is done for each excitation wavelength. The error bars in the relative photon yield come from the uncertainty of the response function of the spectrometer and from the relation between signal to noise, which is strongly dependent on the excitation wavelength.

In both measurements, the error bars on the excitation wavelength are the standard deviation of the gaussian fits of the distribution of excitation light, as described in Subsection 2.3.3.3.

4.3 Results and discussion

The spectra of PEN and TPB excited with 160 nm light are shown in Figure 4.1. The spectra measured with 130 nm excitation light are similar, but are not shown here, since the best signal is obtained with 160 nm excitation light (where the intensity of the deuterium lamp peaks).

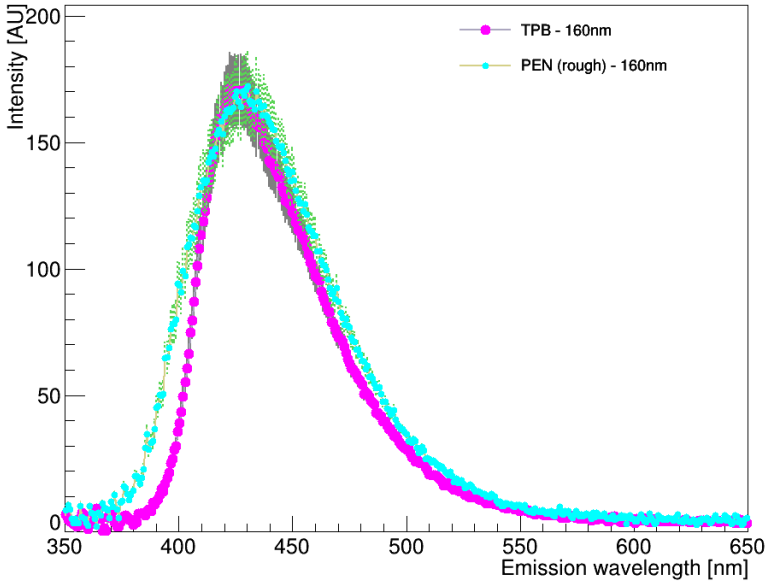

FIGURE 4.1: Fluorescence emission spectra of TPB and PEN (scaled to the same amplitude) excited with 160 nm light. The error bars come from the uncertainty of the response function of the spectrometer

The photon yield of the rough and the smooth PEN samples, measured with the PMT and with the spectrometer, is shown in Figure 4.2 relative to TPB for excitation wavelengths from 120 nm to 250 nm. The wavelength-integrated photon yields (▲) agree within errors with the values measured under the same angle of incidence with the spectrometer (□) at almost all excitation wavelengths. The agreement is better for the excitation wavelengths from 150 nm to 170 nm, where the spectrometer is most sensitive. In this region, the photon yield of PEN rough (shown in blue) measured at different angles also agree within errors. The same does not happen for PEN smooth (shown in gray), which may indicate its dependence on the angle of the measurement.

The rough sample seems to yield more light than the smooth one, since its relative photon yield was higher for both angles of incidence, as shown in Figure 4.3.

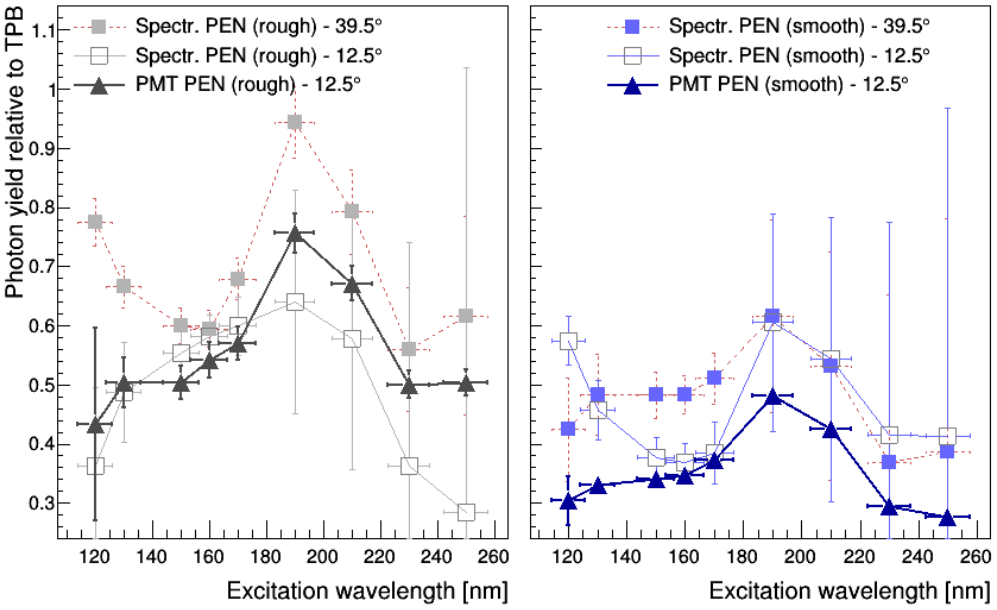

FIGURE 4.2: Photon yield of PEN rough (on the left) and smooth (on the right) relative to TPB and measured with: the PMT (▲), and with the spectrometer at 39.5° (■) and at 12.5° (□). The 2-standard-deviations error bars include statistical and systematic errors.

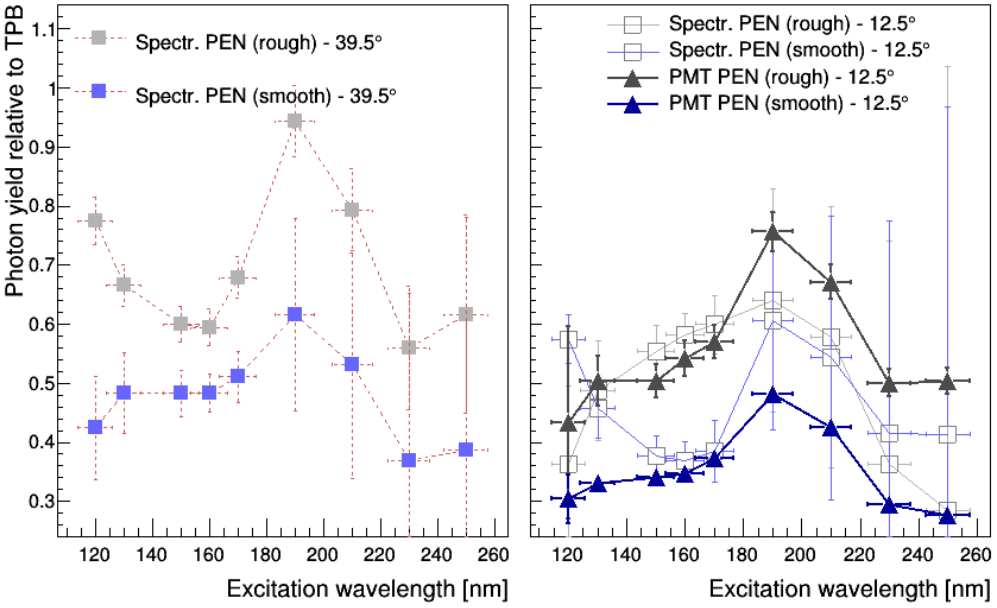

FIGURE 4.3: Photon yield of PEN (rough and smooth) relative to TPB measured under incidence angles of 39.5° (left) and 12.5° (right) with the PMT (▲) and with the spectrometer (■ and □.)

The observed increase in the photon yield of the rough sample can be attributed to: i) an asymmetry in the direction of light emitted (forward/backward), since only one surface was sanded and the sample was not optically coupled to the substrate; ii) the difference between the angular distributions of light emitted by PEN and TPB (in this case, the angle measured might have been unfavorable for collecting light emitted by PEN smooth); and/or iii) the removal of a thin degraded layer by the process of sanding the film. The last is especially important when exciting the sample with VUV, since VUV does not penetrate deep in the sample and a slightly degraded layer could be enough to significantly decrease the wavelength shifting efficiency of the film.

Note that the error bars of the wavelength-integrated photon yield (▲) are smaller. This is because its signal to noise ratio is better than that of the wavelength-resolved ones. Therefore, the wavelength-integrated results will be used to infer the WLSE of PEN relative to TPB. The photon yield of PEN rough (smooth) excited with 130 nm light was 50.42±2.12% (33.06±0.45%) of the photon yield of TPB.

For the results presented in [107], the relative photon yield presented here was conservatively corrected for the measurements of PEN relative to TPB done with an integrating sphere. This correction was done in order not to overestimate the relative WLSE of PEN due to the possible forward/backward asymmetry aforementioned or due to differences in the angular distribution of light emitted by TPB and by PEN. This correction is described in detail in [107] and lowers the values of relative photon yield of PEN presented here by 15% (for the smooth sample) and by 45% (for the rough sample).

4.4 Conclusion

The wavelength shifting of a PEN film relative to TPB was investigated and its emission spectrum was measured with VUV excitation light.

The photon yield of the samples after sanding was higher than before sanding, reaching over 50% of the fluorescence yield of TPB when excited with 130 nm light. In addition to the angle dependence of the light emitted by the smooth sample, a possible asymmetry in the forward and backward emission of light by the rough sample, and the removal of a

degraded layer by sanding were considered as possible causes of the increase in the photon yield. Therefore, pristine samples (preferably from different manufacturers and types) of PEN should be investigated and their exposure to UV light should be controlled, since PEN has been reported to degrade [112].

In order to mitigate possible angle dependence of the measurements due to differences in the angular distributions of the fluorescence emitted by TPB and PEN, the next measurements should be done either with an integrating sphere or at a few more angles, systematically investigating the effects. It is also necessary to test the dependence of the WLSE of PEN on film thickness and test it at LAr temperature, since its efficiency is reported to increase by approx. 30% at low temperatures [109].

The efficiency of TPB does not seem to increase at lower temperatures (as shown in Subsection 3.3.3). Therefore, if the increase in the efficiency of PEN at low temperatures is confirmed, and the efficiency of pristine PEN at RT reaches the value of 50% (or higher) of the photon yield of TPB (as measured for the rough samples), PEN can be considered a strong candidate in substituting TPB in future large-scale LAr-based experiments, such as DUNE [31].

Chapter 5

Simulation of a setup for in-situ attenuation length measurements of LAr scintillation photons

In order to guarantee high efficiency of light detection in a scintillator, it is necessary to know well - and if necessary optimize - its optical properties, especially the transparency of the target to its scintillation photons. The characterization and simulation of a setup to measure the transparency of liquid argon to its photons is the focus of this chapter.

5.1 Attenuation length: overview and literature

The attenuation length is defined as the distance at which the probability that a particle has not been absorbed in a certain material has dropped to 1/e. In this case, the particles are the scintillation photons from LAr and the medium is also LAr. The dependence of the intensity of the particles on the distance for a certain material and energy is described by the Equation 5.1.

$$I = I_0 . e^{\frac{-d}{\lambda_{att}}} \tag{5.1}$$

where I_0 is the initial intensity, d is the distance traveled in the material and λ_{att} is the attenuation length.

The transparency of liquid argon to its own scintillation photons has been measured by several experiments. The authors of [44] measured the attenuation length of the scintillation photons in liquid argon and obtained the value of 66±3 cm. The value found by [43] in the ArDM detector was 50 cm. Reference [45] set a lower limit of 110 cm on the attenuation length of the scintillation from pure liquid argon.

The values reported in the literature disagree, because the attenuation length of LAr depends on the amount of impurities present in the measured sample. Liquid argon itself does not absorb its own scintillation light. However, impurities such as nitrogen, oxygen, methane and xenon absorb the VUV photons from the scintillation of LAr [113][43]. Therefore, the attenuation length in a certain sample of liquid argon gives information about its contamination level. Since the contamination level is not only dependent on the source of the LAr, but also on the environment where it is applied, the measurements of attenuation length should be ideally done in-situ. Measurements of the attenuation length of LAr photons in the GERDA experiment were done and a value of 12.35 cm was found [114].

The setup described here aims to measure the attenuation length of the scintillation photons from liquid argon in the TUM LAr test stand using a triggered source.

5.2 TUM Liquid Argon Test Stand

The TUM LAr Test Stand is located at an underground laboratory, which is at a depth of 10 m.w.e (meters water equivalent) at TUM (Garching-Forschungszentrum). The test stand is composed of a cryostat, a lock and glove box, as shown in Figure 5.1. The cryostat is shielded with lead and has a capacity of approximately 800 kg of LAr. A detailed schematic drawing of the cryostat is shown in Figure 5.2. This test stand is used for the development and test of the LAr veto used in the GERDA experiment [53]. The possible deployment of the attenuation measurement setup in the GERDA experiment is also a motivation for these measurements and for the development of the setup.

FIGURE 5.1: TUM LAr test stand: In the figure, the lock part inside the glove box and the upper part of the cryostat below the glove box are shown.

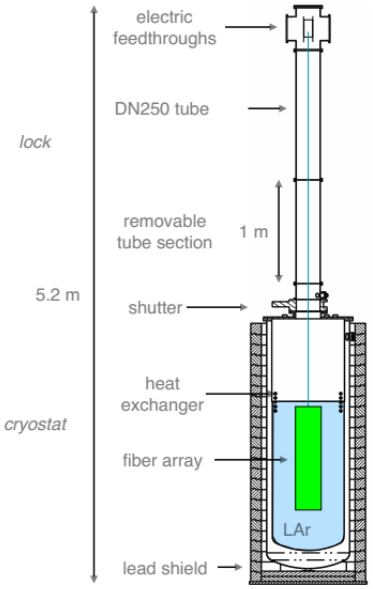

FIGURE 5.2: Schematic drawing of the cryostat (Figure from [53]). Also shown in the scheme are the fibers used in the LAr veto in the GERDA Experiment.

5.3 Selecting a source for attenuation length measurements in LAr

As the light to be measured in this experiment is the scintillation light from liquid argon, a source is necessary to induce scintillation of LAr. In this section, radiation sources for the use in the attenuation length setup are discussed.

Typical radiation sources that can produce excimers in LAr are beta, alpha and gamma sources. Due to the Cherenkov light produced by most beta emitters, beta sources will not be investigated here. Alpha sources produce localized light in LAr, since the penetration depth of alphas is very small. This is an advantage, since localized light production leads to less uncertainties in the distance between the interaction point (where the scintillation light was produced) and the detectors. However, using an open source inside the cryostat could lead to the contamination of the LAr and alpha sources are usually not encapsulated (since the alphas would be shielded by the encapsulation).

In this context, only an alpha source was investigated, a Po-210 source with rolled foils manufactured by Eckert & Ziegler. This Po source is called AFR source (alpha source for research) and is safe against contamination and suitable for high vacuum and low temperature applications. The projected range[1] in LAr of the 5304.38 keV alphas emitted by the Po source is approximately $7.3 \times 10^{-3}\,\mathrm{g/cm^2}$ [115]. The penetration depth in LAr is therefore approximately 52 µm. Any other gamma or alpha emission of Po-210 has a branching ratio below 0.00112 %.

Another possible source is a gamma emitter. Since medium and high energetic gammas penetrate deep in liquid argon, only low energetic gamma sources will be investigated. Also, only sources that produce particles with an attenuation length not longer than the one of the 59.54 keV gamma of Am-241 will be investigated. This energy corresponds to an attenuation length of 1.53 cm in LAr, which is calculated by Equation 5.2, where μ_ϱ is the mass attenuation coefficient and ρ is the density. In Figure 5.3, the mass attenuation coefficients in LAr for energies from 10 to 100 keV are shown. The data was taken from the

[1] "average value of the depth to which a charged particle will penetrate in the course of slowing down to rest. This depth is measured along the initial direction of the particle." [115]

NIST website [116] and used in the calculation of the attenuation lengths shown in the same figure.

$$\lambda_{att} = \frac{1}{\mu_{\varrho} . \rho} \tag{5.2}$$

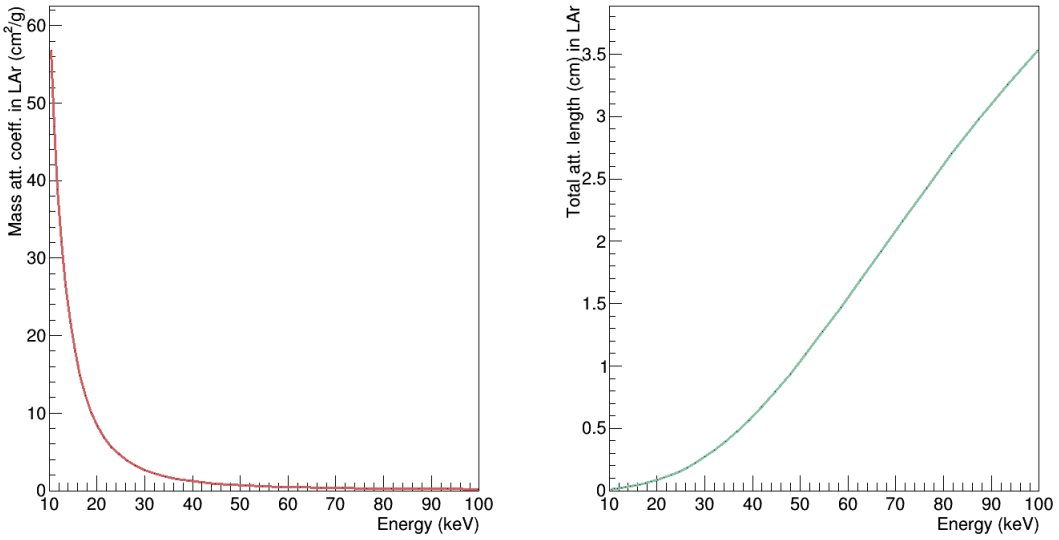

FIGURE 5.3: Left: Mass attenuation coefficients of photons with Energy from 10 to 100 keV in liquid argon. Data from NIST [116]. Right: Attenuation length of photons with Energy from 10 to 100keV in liquid argon. The density of LAr used in the calculation of the attenuation length was 1.3954 g/cm^3.

The gamma sources that are investigated here fulfill the following requirements: Emission of gammas below 60 keV with branching ratio (BR) above 5%, no beta emission or other high energetic gammas (with significant BR) and half-life long enough to do the measurements. The low energetic gamma sources that fulfill these requirements are Te-125m, Re-186m and Am-241[2]. The half-lives, emission energies and branching ratios of these sources are shown in Table 5.1.

The Te-125m source is the least energetic gamma source from the table and therefore produces the most localized scintillation light in liquid argon, with an attenuation length of 0.43 cm. It must be, however, neutron activated. The problem of the neutron activation is that pure Te-124 is necessary in order to be activated. Tellurium has other isotopes that are beta

[2]selected data from the energy-ordered list of principal gamma rays from nuclei whose parent or grandparent half-life exceeds 1h [117]

Isotope	Half-life	Emission energy (keV)	BR (%)
Te-125m (NA)	57.4d	35.4919	6.67
Re-186m (NA)	200000y	40.35	5.04
Re-186m (NA)	200000y	59.009	17.83
Am-241	432.2 y	59.5412	35.9

TABLE 5.1: Half-lives, emission energies and branching ratios of low energetic gamma emitters that fulfill the requirements described in this section. Data taken from [117].

emitters, such as Te-128 and Te-130, which are the most abundant ones. Therefore, Te-125m is not a suitable source. Re-186m can also be obtained with neutron activation. Its main gamma emission is very similar to the gamma emission of Am-241, which does not need to be neutron activated and is easily available. Therefore, this source will be further investigated in the next subsection.

5.3.1 Characterization of the americium source

Am-241 is obtained from Pu-239. Pu-239 is irradiated with neutrons and decays through a beta decay generating Am-241. This process is done in nuclear reactors and Am-241 sources are commercially available.

In order to avoid contamination of the LAr in the cryostat by the source, the source was encapsulated with a thin layer of stainless steel. Its radioactivity was measured before and after encapsulation with the low background germanium detector, which is very sensitive to low energies due to its thin entry window. These measurements are described in Section C.1. The radioactivity of the source was estimated to be 24.28±0.11 kBq and the percentage of the gammas that are attenuated by the encapsulation is approximately 50%.

5.4 Triggered detection of scintillation light from liquid argon with an americium source

As shown in the previous section, the attenuation length of the 59.54 keV Am-241 gammas is 1.53 cm in liquid argon. The probability of finding a particle at a certain distance from the source is described by the Equation 5.3.

$$P(d) = e^{\frac{-d}{\lambda_{att}}} \tag{5.3}$$

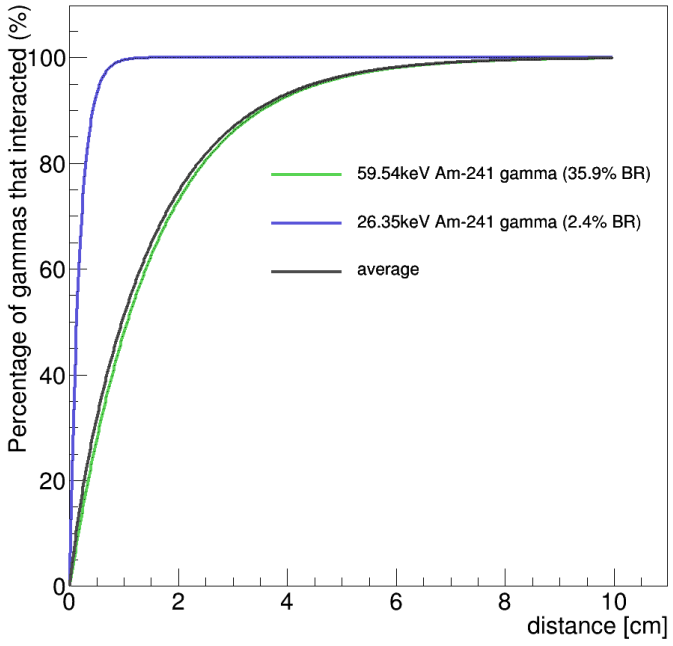

FIGURE 5.4: Distance from the source versus percentage of Am-241 gammas that have interacted up to this distance. This is shown for two gamma energies and the average accounts for the branching ratios.

Therefore, the fraction of gammas that interact with LAr at a certain distance from the source is $1 - P(d)$ and is shown in Figure 5.4. This figure shows that the percentage of gammas from americium that were attenuated in LAr reaches 99.5% at a distance of 8 cm. In this figure, only the 59.54 keV and 26.35 keV gammas are shown, because there are no other gammas emitted with a significant branching ratio (all of them are below 0.2%). The average fraction of gammas that interact at a certain distance is very close to the fraction of 59.54 keV gammas that interact at this distance. Therefore, I will only consider this gamma line in the next simulations.

In order to determine the attenuation in LAr, the distance between scintillation production (gamma interaction) and light detection (distance to the photodetector) must be well known. Therefore, a constrained active volume will be used. That is, gamma interactions outside this active volume will not be taken into account and the ones within the active volume will

trigger the measurement. The possible active volumes, trigger thresholds and photodetectors are discussed in the next sections.

5.4.1 Detection of scintillation photons from LAr with SiPMs

To detect the scintillation light from LAr, two types of silicon photomultipliers (SiPMs) will be used: the "trigger" SiPMs and the "far" SiPMs. The trigger SiPMs (two or three) will be located very close to the source (at a distance from 1 cm to 2 cm). The SiPMs used will be the 4th generation of the Hamamatsu VUV-MPPC silicon photodetectors, which are sensitive to the VUV region and have a quantum efficiency of approximately 14% at 128 nm. These SiPMs are suitable for cryogenic temperatures and the S13374 series is very radio-pure compared to other SiPMs. They are available with an active area of 6 mm^2, 9 mm^2 or 36 mm^2. The selected SiPM for these measurements were the S13370 series with a photosensitive area of 36 mm^2.

The far SiPMs will be placed further away from the source (at distances from 4 cm to 38 cm) in order to measure the attenuation of the LAr scintillation photons. The far SiPMs are arrays of 9 Ketek SiPMS bonded at the surface of a quartz holder sputtered with aluminium, as shown in Figure 5.5. As there are a few of them available, each array will be placed at a distance, so that the scintillation light produced by the source can be simultaneously detected at different distances.

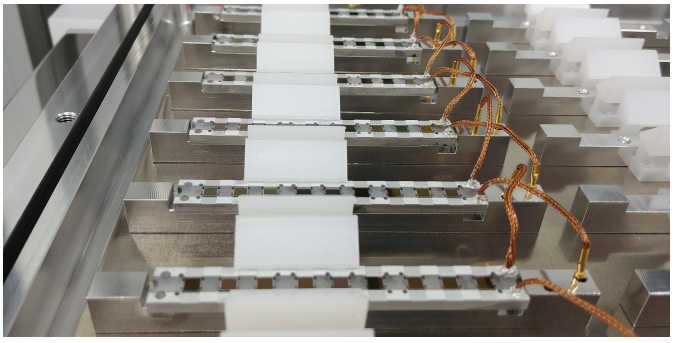

FIGURE 5.5: SiPM arrays before being attached to the fibers for the GERDA LAr veto. Each array is composed of 9x9 mm^2 Ketek SiPMs.

The area of each SiPM is 9 mm^2, so the SiPM array has a total area of 81 mm^2. These arrays are the same used in the LAr veto in GERDA and they are not sensitive to VUV photons.

Therefore, a special window coated with TPB must be designed for the use of the SiPM arrays in the attenuation measurements. The resulting efficiency of these SiPMs in detecting VUV photons is calculated in Equation 5.4

$$\epsilon_{tot} = QE_{SiPM}(\lambda_{TPB}) \times \epsilon_{TPB} \times T_{window} \tag{5.4}$$

where $QE_{SiPM}(\lambda_{TPB})$ is the quantum efficiency of the SiPM at the emission wavelength of TPB, ϵ_{TPB} is the wavelength shifting efficiency of TPB multiplied by a geometrical factor and T_{window} is the transmittance of the window. The transmittance of the window was assumed to be 90% and the wavelength shifting efficiency of TPB assumed to be 100%. As TPB emits fluorescence light isotropically, I will assume that 50% of the fluorescence photons go in the direction of the SiPMs. Therefore, ϵ_{TPB} is equal to 0.5. The quantum efficiency of the Ketek SiPMs at the emission wavelength of TPB is 43%, resulting in ϵ_{tot} equal to 0.19.

5.4.2 Simulation of the production and detection of scintillation photons in LAr

A toy Monte Carlo 2D simulation was done in order to verify the feasibility of the attenuation measurements using an americium triggered source and the SiPMs. The toy simulation estimates how many photons will be detected by each SiPM at different distances from the source for the distribution of gamma interactions in LAr shown in Figure 5.4. This information is necessary in order to determine:

1) The optimal active volume (AV) used to trigger the measurement (as discussed in Section 5.4).

2) The optimal distance between the trigger SiPMs and the source.

3) The distances between the far SiPMs and the source.

4) The relation between the attenuation of scintillation photons and the number of detected photons.

5) The trigger threshold of the trigger SiPMs.

In this simulation, 100K pseudo-random numbers are produced according to the probability density function of one gamma emitted by the source to interact with LAr at a distance d. The distribution of these numbers is shown in the first plot of Figure 5.6. The possible radiuses of active volumes investigated here were 0.2, 0.3, 0.4 and 0.5 cm. The fraction of gammas that interact within the AV is shown in purple on the first plots of Figure 5.6 to Figure 5.9 and vary from 0.12 to 0.28.

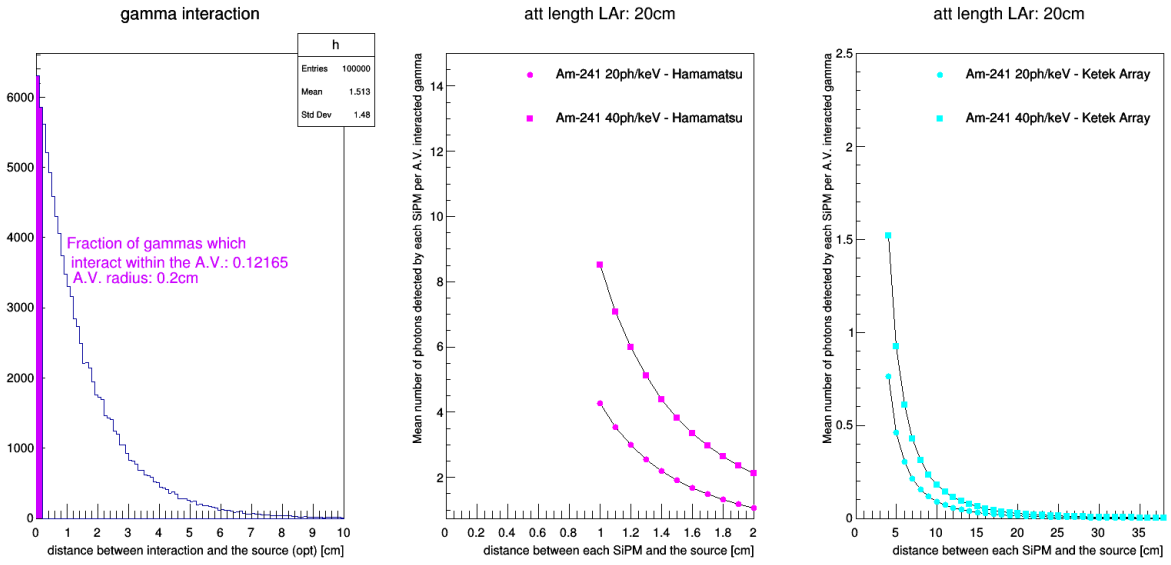

FIGURE 5.6: Left: 100K gammas distributed according to the distance at which they interact in LAr. The fraction of gammas that interacted in the active volume AV is shown in purple. The active volume considered here is a hemisphere of radius 0.2 cm and centered at the source. Middle (right): Mean number of photons detected by the trigger (far) SiPM per gamma that interacted in the AV for the values of LY of 20 and 40 ph/keV. The value of attenuation length of the scintillation photons in LAr used in the simulation was 20 cm.

In this simulation, these gammas come only from the front part of the source and are distributed in a semi-circle around it. The distance between the production of scintillation by the gamma in LAr and detection by the SiPM depends on the interaction distance from the source and the angle of emission within the semi circle. These distances are taken into account in the solid angle correction in order to know how many photons reach the SiPM. The number of scintillation photons produced per keV in LAr is 40, according to [38]. This number may also be dependent on the sample of LAr, since an increased content of oxygen leads to less recombination and less light yield. The number found by [114] that best fit the data was 1600 photons per MeV. In the simulation, two values of light yield in LAr were

used: 20 and 40 ph/keV. The number of photons that reach the SiPM, N_γ^r, per 59.54 keV gamma emitted by the source is calculated by Equation 5.5.

$$N_\gamma^r = E_\gamma \times LY \times \Omega_{corr} \times P(d) \tag{5.5}$$

where E_γ is 59.54 keV, LY is either 20 or 40 ph/keV, Ω_{corr} is the solid angle correction and $P(d)$ is the fraction of photons that have not been attenuated while traveling the distance from the source to the SiPM, as shown in Equation 5.3. The value of 20 cm for the attenuation length of LAr scintillation photons was assumed and other values will be later investigated. The solid angle correction was calculated in different ways for the trigger and far SiPMs. As the trigger SiPMs are very close to the source and have a square shape, the solid angle correction was given by the ratio of the solid angle of a square plate[3] divided by 4π, as shown in Equation 5.6.

$$\Omega_{corr} = \frac{\Omega_{sq}}{\Omega_{tot}} = \frac{4arccos\frac{\sqrt{1+2\alpha^2}}{1+\alpha^2}}{4\pi} \tag{5.6}$$

$$\alpha = \frac{SiPMsidesize}{2 \times distance} \tag{5.7}$$

The solid angle correction for the far SiPMs was calculated by dividing the total area of the SiPMs by the area of the sphere with radius equal to the distance. Note that this correction leads to a simple estimation and does not take the rectangular shape of the SiPMs neither their area distribution in the sample holder into account. These factors must be later considered for better estimations.

After calculating the number of photons that reach the SiPM, the number of photons that are detected by the SiPM are calculated as shown in Equation 5.8.

$$N_\gamma^{det} = N_\gamma^r \times \epsilon_{tot} \tag{5.8}$$

[3] Adapted from "Solid Angle of a Rectangular Plate" - Richard J. Mathar

where ϵ_{tot} is the detection efficiency of the SiPMs. ϵ_{tot} of the trigger SiPMs is simply their quantum efficiency at 128 nm and ϵ_{tot} of the far SiPMs was calculated in Equation 5.4. The mean number of detected photons by each SiPM (trigger SiPM in magenta and far SiPM in cyan) at different distances and for the LY of 20 or 40 ph/keV is shown in Figure 5.6 to Figure 5.9. Each figure shows these numbers for different active volumes (AV).

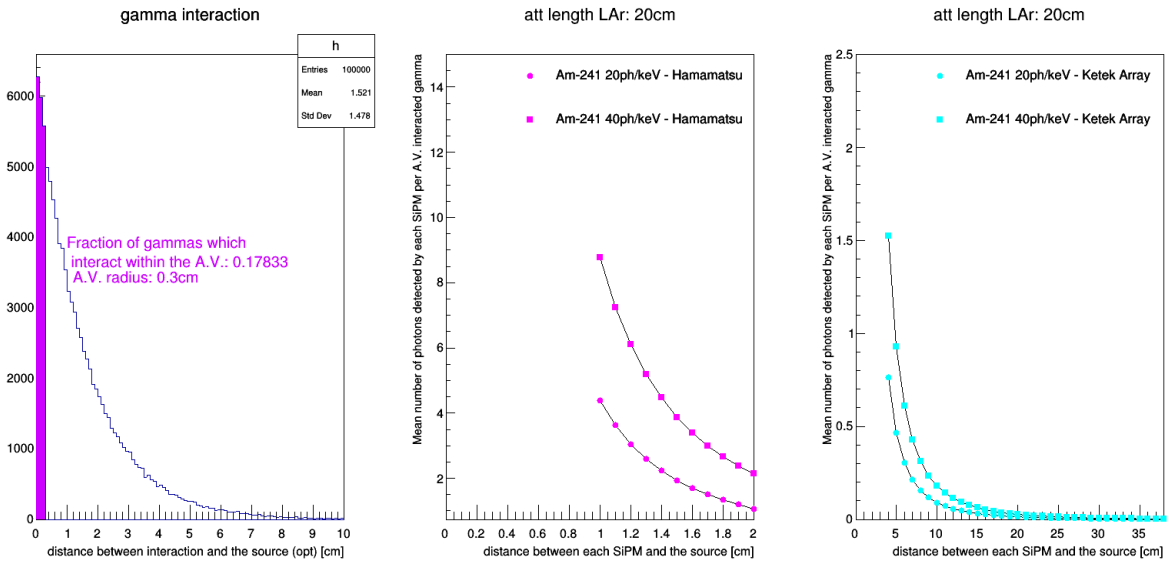

FIGURE 5.7: Left: 100K gammas distributed according to the distance at which they interact in LAr. The fraction of gammas that interacted in the active volume AV is shown in purple. The active volume considered here is a hemisphere of radius 0.3 cm and centered at the source. Middle (right): Mean number of photons detected by the trigger (far) SiPM per gamma that interacted in the AV for the values of LY of 20 and 40ph/keV. The value of attenuation length of the scintillation photons in LAr used in the simulation was 20 cm.

Figure 5.6 to Figure 5.9 show that the mean number of detected photons per gamma that interacted in the AV does not significantly increase for larger AVs. This indicates that the AV will not be well defined, since the trigger SiPMs will detect roughly the same number of photons for interactions happening within 0.5 cm from the source. The active volumes and the number of photons detected in each SiPM are further investigated in Section C.2. The closer the trigger SiPM is, the more photons it detects. Therefore, the distance of the trigger SiPM to the source will be chosen as 1 cm. The pile-up probability is low, since the radioactivity of the source is low and approximately half of the gammas are attenuated by its steel encapsulation. The rate of the 59.54 keV gammas (main gamma emission) that exit the front part of the encapsulation of the source was calculated in Section C.1 and is approximately 2 kHz.

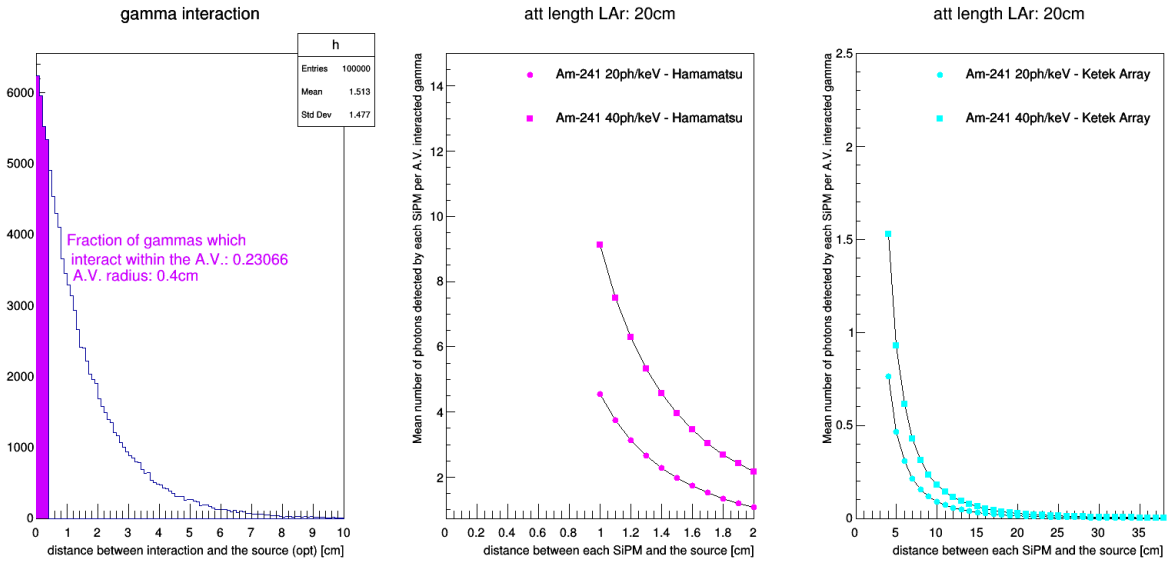

FIGURE 5.8: Left: 100K gammas distributed according to the distance at which they interact in LAr. The fraction of gammas that interacted in the active volume AV is shown in purple. The active volume considered here is a hemisphere of radius 0.4 cm and centered at the source. Middle (right): Mean number of photons detected by the trigger (far) SiPM per gamma that interacted in the AV for the values of LY of 20 and 40ph/keV. The value of attenuation length of the scintillation photons in LAr used in the simulation was 20 cm.

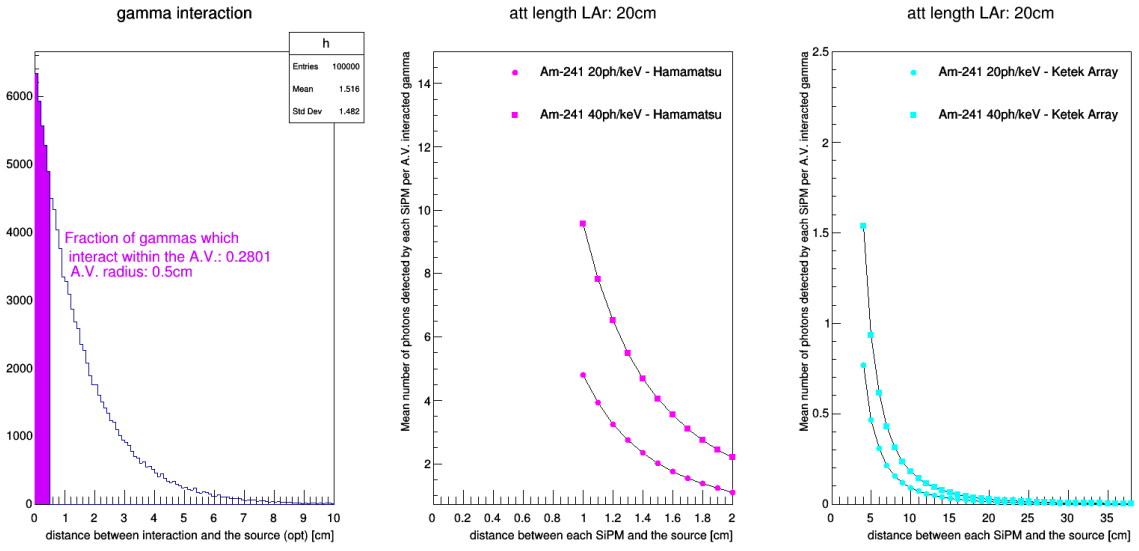

FIGURE 5.9: Left: 100K gammas distributed according to the distance at which they interact in LAr. The fraction of gammas that interacted in the active volume AV is shown in purple. The active volume considered here is a hemisphere of radius 0.5 cm and centered at the source. Middle (right): Mean number of photons detected by the trigger (far) SiPM per gamma that interacted in the AV for the values of LY of 20 and 40ph/keV. The value of attenuation length of the scintillation photons in LAr used in the simulation was 20 cm.

Note that the number of detected photons shown in Figure 5.6 to Figure 5.9 is the mean number for a single SiPM. In order to determine the the trigger threshold, it is necessary to understand the minimum and maximum number of photons detected by each trigger SiPM. This investigation is described in Section C.2. The trigger threshold was set as two photons, that is, the SiPMs should trigger the measurement if both of them detect two photons.

In the plots on the right of Figure 5.6 to Figure 5.9, we see that the number of photons detected by the far SiPMs is only above one for the array placed at a distance of 4 cm from the source and for the LY of 40 ph/keV. These results were calculated for an attenuation length of 20 cm. The results for different attenuation lengths are shown in Figure 5.10.

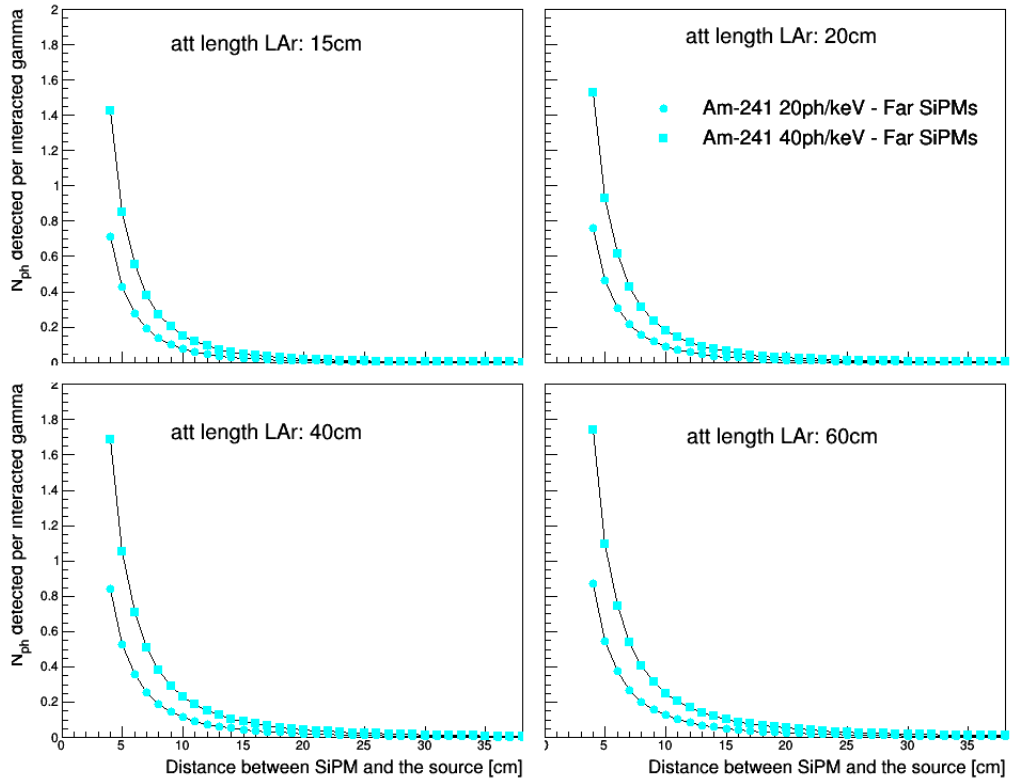

FIGURE 5.10: Mean number of photons detected by the far SiPMs (per gamma that interacted within the AV) at different distances from the source and for different values of the attenuation length of scintillation photons from LAr. The AV considered here was 0.5 cm(radius).

These estimations show that the mean number of detected photons by the far SiPMs is always below one for distances above 5 cm. Smaller distances were not investigated due to the complicated angular correction that would be necessary to account for the rectangular shape of the array which is 7.56 cm long and not fully covered by the SiPMs (less than 14%

of the area of the array is covered by the SiPMs). Since the arrays are large to be placed at smaller distances, the use of square SiPMs (instead of small SiPMs distributed in an array) for the distances between 1 and 4 cm is recommended. The advantage of the SiPM arrays is that a few of them can be placed at different distances from the source, allowing for simultaneous detection at different distances. However, their total photodetection area is small and 1-inch PMTs coated with TPB would detect approximately 5 times more photons.

5.5 Summary

In this chapter, radioactive sources for the use in the attenuation measurements of scintillation photons from LAr were discussed. An americium source was characterized, photodetectors and methods were suggested, and a simple simulation was done in order to test the feasibility of these measurements at the TUM LAr test stand with the available SiPM arrays, the Hamamatsu VUV SiPMs and a triggered source.

The 2D simulation estimated how many photons will be detected by each SiPM at different distances from the source. 28.01% of the gammas interact within 0.5 cm from the source and a mean number of approximately 10 photons are detected per interaction within this volume. For a trigger SiPM placed 1 cm away from the source, a threshold of 2 photons can be set for an active volume of 0.5 cm radius.

The mean number of photons detected by the far SiPMs is below one for all the cases considered and distances above 5 cm. The use of larger photodetectors could improve this value. Furthermore, the arrays are large to be placed at smaller distances, thus the use of single larger square SiPMs, such as the VUV Hamamatsu SiPMs, for the distances between 1 and 4 cm is recommended.

The estimates of this chapter indicate that the attenuation length measurements at the TUM LAr test stand using the characterized americium source and the suggested photodetectors is feasible. A more sophisticated simulation for better estimations is suggested in Section C.3.

Chapter 6

Summary and outlook

In this master's thesis, I investigated the wavelength shifting of scintillation photons from liquid argon in two contexts. The first one is related to the undesired wavelength shifting of VUV photons by detector materials that are usually not expected to fluoresce, and whether this could cause a background in the LAr and LXe-based experiments that use these materials in their cryostats. The second one is related to the efficiency of a wavelength shifter that has been proposed as a replacement for TPB in upcoming LAr-based experiments.

The materials investigated in the first context were acrylic and PTFE, focusing on the batches from DEAP and LUX experiments, respectively. The question as to whether PTFE and acrylic shift UV light was not only motivated by some phenomena observed in these experiments but also by the extensive literature on the photoluminescence of these materials (both discussed in Section 1.6). Despite this broad literature, the photoluminescence response of these plastics to VUV light had not yet been reported[1].

The work I present in this thesis is the first investigation of the photoluminescence of PTFE and acrylic excited with VUV light. The lack of literature for excitation with VUV light may be due to the difficulty of combining VUV fluorescence setups with high sensitivity to low levels of fluorescence. In this context and for this master's thesis, a VUV fluorescence setup was optimized, its stability was investigated, and its wavelength-resolved photodetector was calibrated. After these improvements, the sensitivity of the setup achieved the target

[1] To the best of my knowledge.

of measuring the photoluminescence response of the plastics at a level better than 1% of the WLSE of TPB. This value represents the level of fluorescence necessary for acrylic to create a background event in the DEAP detector. The limits set on the wavelength shifting efficiency of the acrylics used in DEAP and the PTFE used in LUX, excited with VUV light at RT, are approximately 0.2% of the WLSE of TPB. The limiting factors of the sensitivity were thoroughly investigated and were found to be stray light from the monochromator and fluorescence of the optical lens. It was also found that the cleaning procedure of the materials may play an important role in their photon yield.

In addition to VUV light, I also investigated whether acrylic shifts UV light of longer wavelengths. This investigation is relevant because particles traversing acrylic can produce Cherenkov light and there is evidence that acrylic shifts part of the UV Cherenkov light to the visible range. The response of acrylic and PTFE to UV light with wavelengths up to 300 nm was investigated and described in Section 2.3. The response of acrylic to UV light up to 380 nm was investigated and described in Section 2.4. In this section, some evidence that acrylic fluoresces when excited with 280 nm light was presented. This was further investigated with an optical cryostat at Queen's University (described in Chapter 3).

With the optical cryostat, the time-resolved fluorescence response of acrylic to UV light was measured at low temperatures for the first time. The temperatures measured included 87 K (LAr) as well as RT and lower temperatures (down to 4 K). A limit below 1% was set on the WLSE of acrylic, relative to that of TPB, at LAr temperature. The dependence of the photon yield of acrylic on temperature was measured and an increase of the intensity with decreasing temperature was observed. In order to exclude sources of background fluorescence and confirm whether this increase is due to the higher fluorescence yield of acrylic at low temperatures, further measurements were suggested. Time-resolved measurements of PTFE with the optical cryostat were also planned and have not yet been accomplished. These measurements could exclude or confirm the suspects of [87] and were suggested as a follow-up of the work done together with the other collaborators from Queen's University.

Regarding the possible causes of fluorescence of acrylic, I raised the question (in Section 1.6) as to whether the energy calibrations done in DEAP with pulsed LEDs and radioactive sources could generate color centers in acrylic that would later fluoresce when excited by UV

light. To answer this question, I started analyzing the data from DEAP before and after calibrations. This analysis is still ongoing and is therefore not described in detail in this thesis.

In the context of wavelength shifters for the detection of scintillation photons from LAr, I measured the WLSE of a polymer (PEN) that has been proposed as a competitive alternative to TPB in future LAr-based experiments. The spectrum of PEN excited with VUV light and its WLSE relative to that of TPB were measured. The photon yield of PEN reached 50% of the photon yield of TPB excited with 130 nm light. Further measurements were suggested in order to assess the angle dependence of this value and investigate the degradation of PEN, the dependence of its WLSE on film thickness and temperature, and the variability of the WLSE for different types and manufacturers. In the context of photon detection of scintillation light from LAr, the measurement of the attenuation length of the LAr of the TUM LAr Test Stand was planned. Possible sources and photodetectors for these measurements were considered and a first feasibility simulation was done.

Although the results of this thesis set stringent limits on the photoluminescence of PTFE and acrylic at RT, and limits on the WLSE of acrylic at LAr temperature, they do not fully exclude the possibility as to whether these plastics could cause a background in dark matter experiments. In order to completely answer this question, the VUV fluorescence setup at TUM will be upgraded to enable low-temperature measurements of low levels of photoluminescence (as well as the low-temperature measurements of the WLSE of PEN). This future work and the results presented in this thesis are especially important for the development of future rare event search experiments based on liquid scintillators that emit VUV light [31, 118, 119], and may also be of interest for the background analysis of ongoing experiments that use acrylic or PTFE surrounding their target, such as DEAP [58], LUX [64], DarkSide [41], Xenon [65], ArDM [48] and SNO [62]. Furthermore, due to the possible wavelength shifting of Cherenkov light, they might also be relevant for future experiments that will use acrylic vessels, such as JUNO [63].

Appendix A

Appendix to the Chapter 2

A.1 Stability measurements and dead time estimation

Dark rate stability

I measured the dark rate of the PMT 50 times within approximately 2.5 hours. Each 10 measurements were done in a row and their averages are shown in magenta. The error bars show one standard deviation.

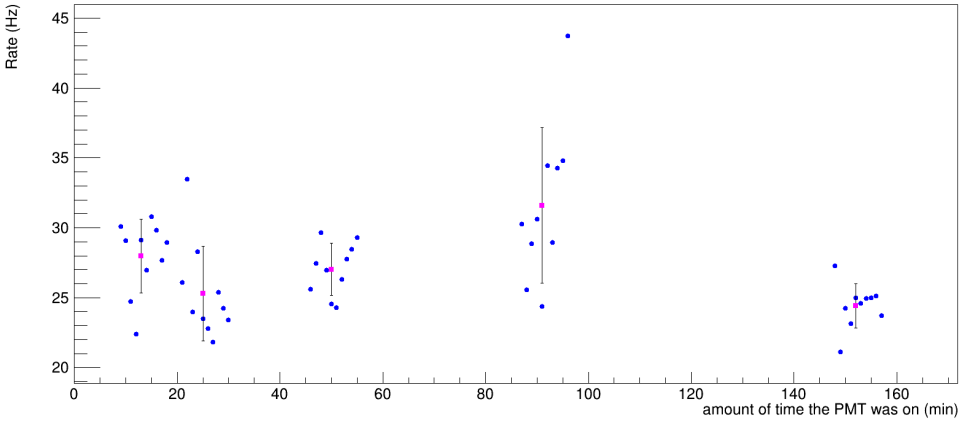

FIGURE A.1: Blue: Dark rate of the PMT versus amount of time the PMT was on (min). Magenta: Average of each 10 measurements done in a row and one standard deviation.

Figure A.1 shows that the mean dark rate versus time is stable within approximately ±10% within 2.5 hours. Thus, the PMT does not need to be turned on a long time before starting

the measurements and its warm-up time was defined as one hour. From the spread of mean values versus time, a systematic error of the dark rate, σ_{syst}^{DR}, was derived.

Lamp stability

In order to investigate the stability and warm-up time of the deuterium lamp, I turned the PMT on at first and then the lamp 70 minutes later. TPB was used as a reference sample, since the fiber is positioned in such a way that it only sees light coming from the samples. The excitation wavelength was 160 nm. The rate of the PMT was measured 50 times within approximately 2.5 hours, as shown in Figure A.2.

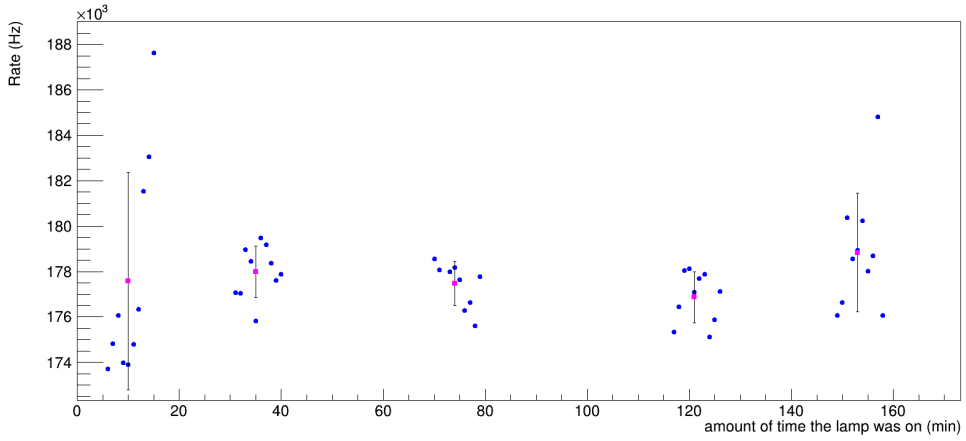

FIGURE A.2: Blue: Rate measured from the measurement of TPB versus amount of time the lamp was on (min). Magenta: Average of each 10 measurements done in a row and one standard deviation.

This figure shows that the lamp takes approximately 30 minutes to be warm and stable. From the spread of mean values versus time, a systematic error of the intensity of the lamp, σ_{syst}^{Lamp}, was derived. These measurements also show that TPB does not seem to degrade when exposed to the most intense VUV wavelength (160 nm) of the deuterium lamp[1] for approximately 2.5 hours.

[1]The power of the incident light at this wavelength is not known.

Dead time

The pulses of the PMT and of the constant fraction discriminator (CFD) measured with an oscilloscope are shown in Figure A.3. The time grid is 200 ns/div. The pulse width of the PMT is approximately 20 ns and the one of the CFD is approximately 400 ns. Since the rate of the PMT when measuring TPB goes from a few kHz to some hundreds of kHz (at the strongest excitation wavelength, 160 nm), the rate must be corrected for the dead time of the counter due to the pulsed width from the CFD. This correction is very small for most of the measurements and is only significant (above 2%) for measurements of an efficient WLS, such as TPB for high-intensity excitation wavelengths, such as from 150 nm to 180 nm.

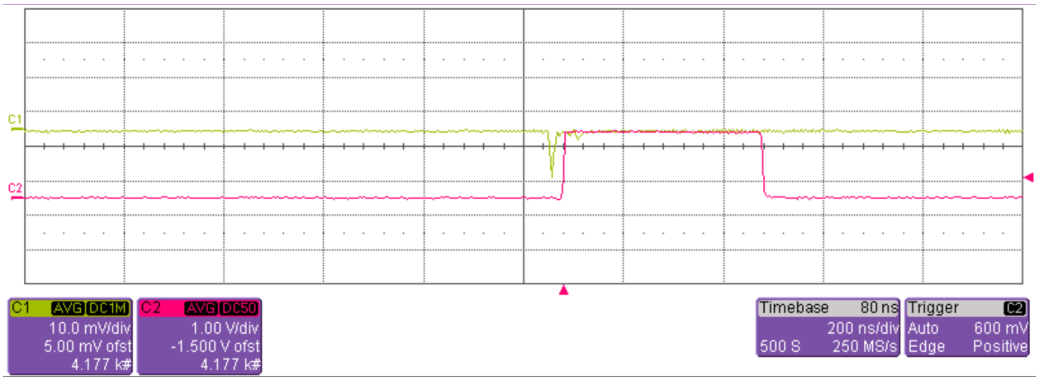

FIGURE A.3: The pulse of the PMT is shown in yellow. The pulse of the constant fraction discriminator is shown in magenta.

A.2 Calibration measurements and cross-checks

As a second cross-check of the calibration of the Ocean Optics spectrometer, I measured the spectrum of the wavelength shifter 1,4-Bis(2-methylstyryl)benzene (Bis-MSB) excited with 160 nm light, corrected it for the calibrated wavelength-dependent response of the spectrometer (Figure 2.6), and compared it to the spectrum measured with the Cary Eclipse spectrophotometer. The spectra are shown in Figure A.4 (A): before correction is shown in yellow, after the calibration correction is shown in magenta, and measured with the Cary Eclipse spectrophotometer with 260 nm excitation light is shown in black. The spectrum measured with the Cary Eclipse spectrophotometer coincides with the one measured with the Ocean Optics after the wavelength-dependent response correction.

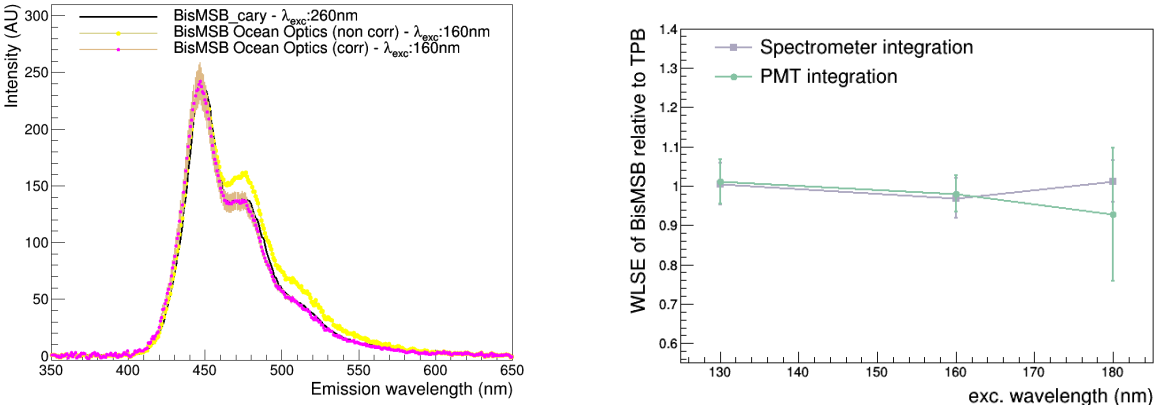

(A) (B)

FIGURE A.4: (A): Emission Spectra of BisMSB. The spectrum shown in black was measured with the Cary Eclipse spectrophotometer and coincides with the one in magenta. The spectrum measured with the Ocean Optics spectrometer is shown before and after corrections in yellow and magenta respectively. (B): Wavelength shifting efficiency of BisMSB relative to TPB, measured with both the spectrometer and the PMT.

To verify whether the relative integration of spectra measured with the spectrometer (after applying the calibration corrections) is consistent with the wavelength-integrated relative photon yield measured with the PMT (corrected for its quantum efficiency dependence), the photon yield by Bis-MSB was measured with both the spectrometer and PMT. Then, its WLSE (relative photon yield) was compared to TPB (also measured under the same conditions). This is shown in Figure A.4 (B) and the results agree within errors.

Appendix B

Appendix to the Chapter 3

B.1 PMT and DAQ settings

In order to set the optimal operating voltage of the PMTs for these measurements, the dark count, the signal amplitude and the single-photoelectron spectrum of the PMTs were characterized at different voltages (V): 1000, 1100, 1200 and 1250.

For these tests, a visible (blue) pulsed LED was used. The PMT was coupled via a sleeve to a dark box, as shown in Figure B.1, and it detected only the light of the pulsed LED. The voltage on the LED was low, in order to pulse it at a single-photon mode.

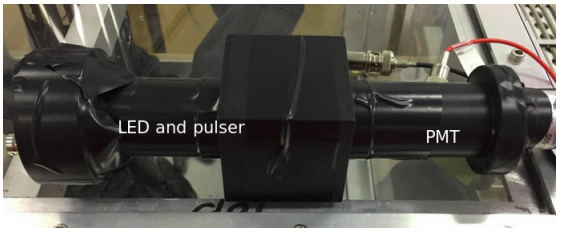

FIGURE B.1: Pulsed LED and PMT inside the dark box.

These tests were done for both PMTs, but here only the results of the super bialkali PMT are shown.

For different voltages applied to the PMT, the baseline remained constant while the mean charge integral of a pulse increased almost 3 times, as shown in Figure B.2. Also, the single-photoelectron spectrum became more separated from the noise pedestal. The dark rate also

increased almost 3 times, but it was still very low at a voltage of 1250 V (less than 100 Hz for the super bialkali PMT). As dark rate in these measurements will be negligible due to the small integration window, the higher voltage (1250 V) was chosen in order to have pulses with higher amplitude and more clearly separated from the baseline and noise.

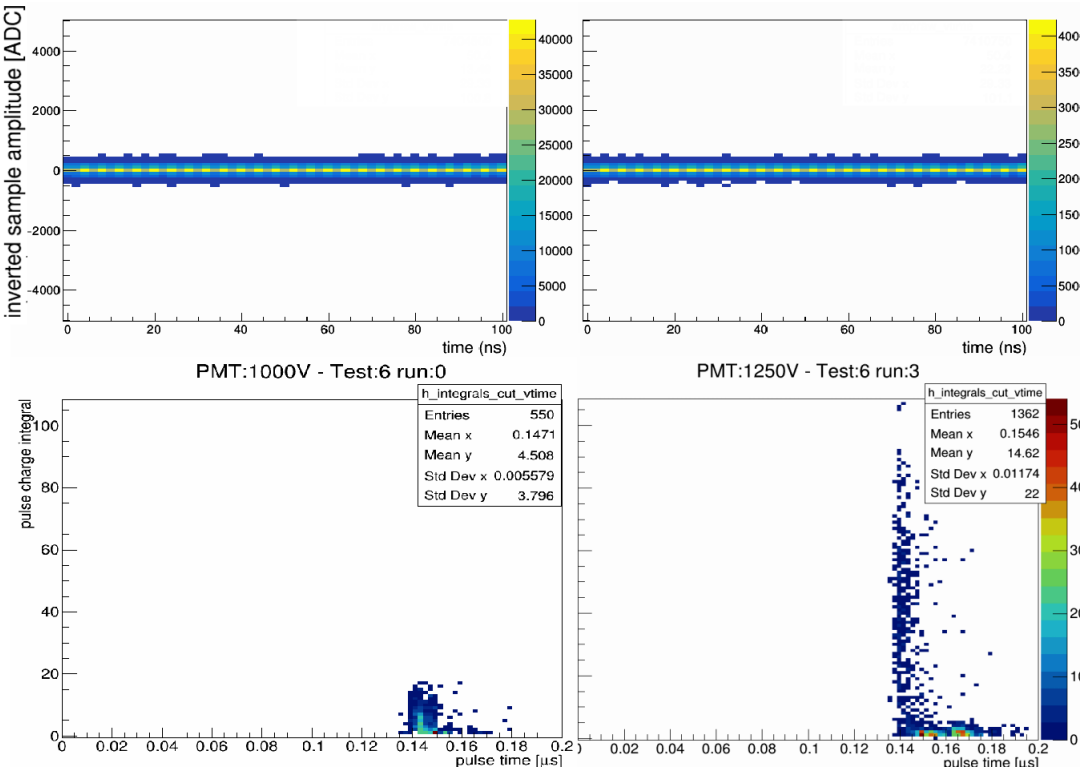

FIGURE B.2: Upper plot: 2D histogram of the baseline (amplitude vs. time) for approx. 30000 events for a PMT voltage of 1000V (on the left) and 1250 V (on the right). Bottom: Charge integrals of the pulses for a voltage of 1000V (left) and 1250 V (right).

The pulse finding threshold of the online analysis was set as 4 standard deviations from the mean baseline. The distribution of the pulse amplitudes of the visible LED pulsed in single-photon mode is shown in Figure B.3, (A). In (B) the pulses of 45000 recorded events that were identified by the pulse finder of the online analysis are shown versus arrival time.

To ensure that the PMT did not saturate when measuring TPB and check whether the pulses were being correctly integrated for the PMT and DAQ settings, some tests were done with TPB excited by the UV LED, as shown in Figure 3.1. The saturation of the pulses was less than 0.01% for the measurements of TPB at RT. The UV LED was also pulsed with a low voltage to produce single photons. The spectrum of the pulses detected by the super bialkali PMT in these measurements is shown in Figure 3.5 and described in Section 3.2.

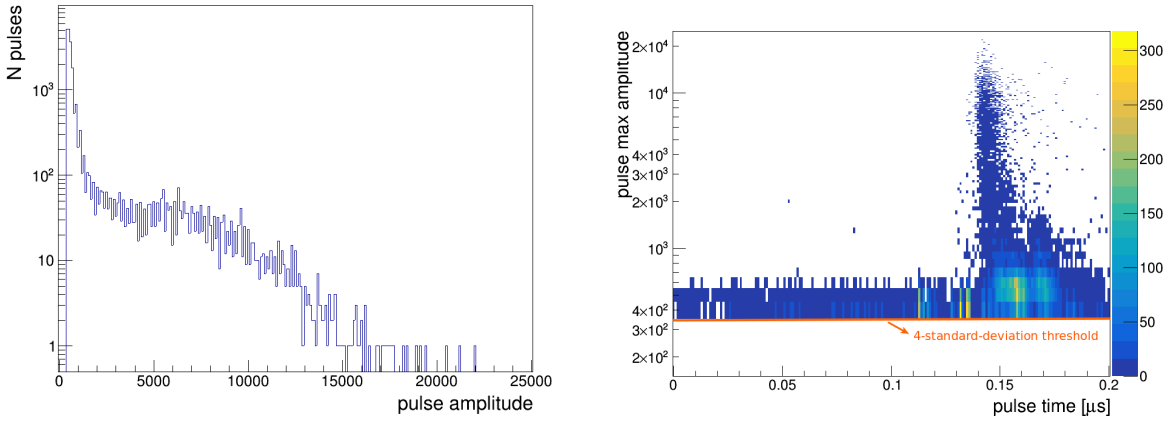

(A) (B)

FIGURE B.3: (A): Amplitude distribution of pulses (or samples) above the pulse finding threshold. (B): Pulse amplitude vs. pulse arrival time for 45000 events. The line in orange and the arrow indicate the pulse finding threshold.

B.2 Systematics, pulses and cuts

Stability investigation: Measurements at RT

Measurements of TPB at room temperature were done in the beginning of the cryostat run (at 300 K) and a long measurement was also taken at the end of the run (at 290 K). The 45000 events recorded at 300 K were divided into 20 sets of measurements and the mean values of the integrated ADC counts for each individual set was added to the histogram of Figure B.4 (A). Mean values (using the same number of events to calculate the average) of the measurements done at 290 K and for a shorter run at 286 K are also shown in the same histograms. The runs with more statistics (20 values or more of mean photon yield) agree within errors. The same is true for RPT, shown in (B).

Pulse arrival time distributions and average pulses at different temperatures

As an investigation of the dependence of the pulse arrival time on the temperature, the pulse arrival time distributions of each sample (RPT and TPB) were plotted at different temperatures (300 K, 210 K, 87 K and 4 K). These distributions are shown in Figure B.5 and Figure B.6. After applying the cuts, these distributions are roughly the same at different temperatures (see mean values in the statistic boxes).

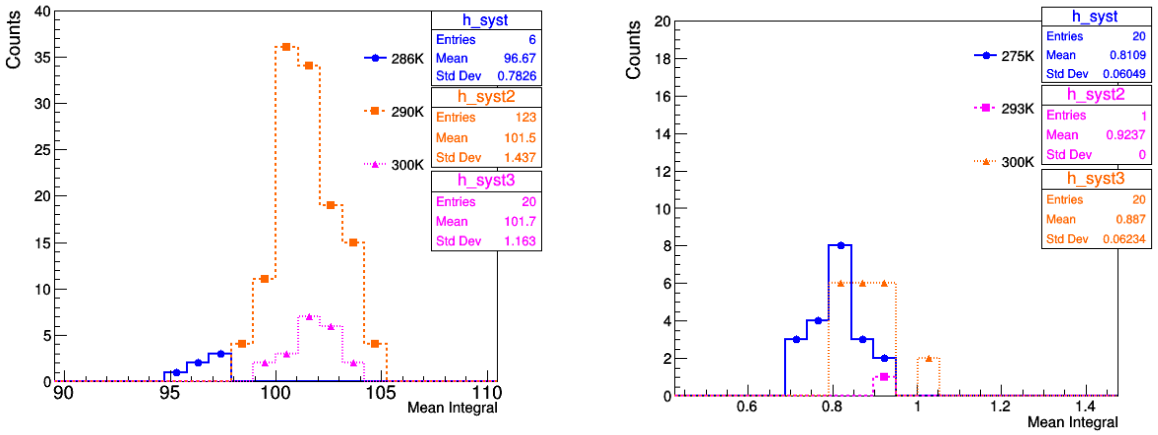

(A) (B)

FIGURE B.4: Mean values of photon yield (integrated ADC counts) of TPB (A) and RPT (B) at RT.

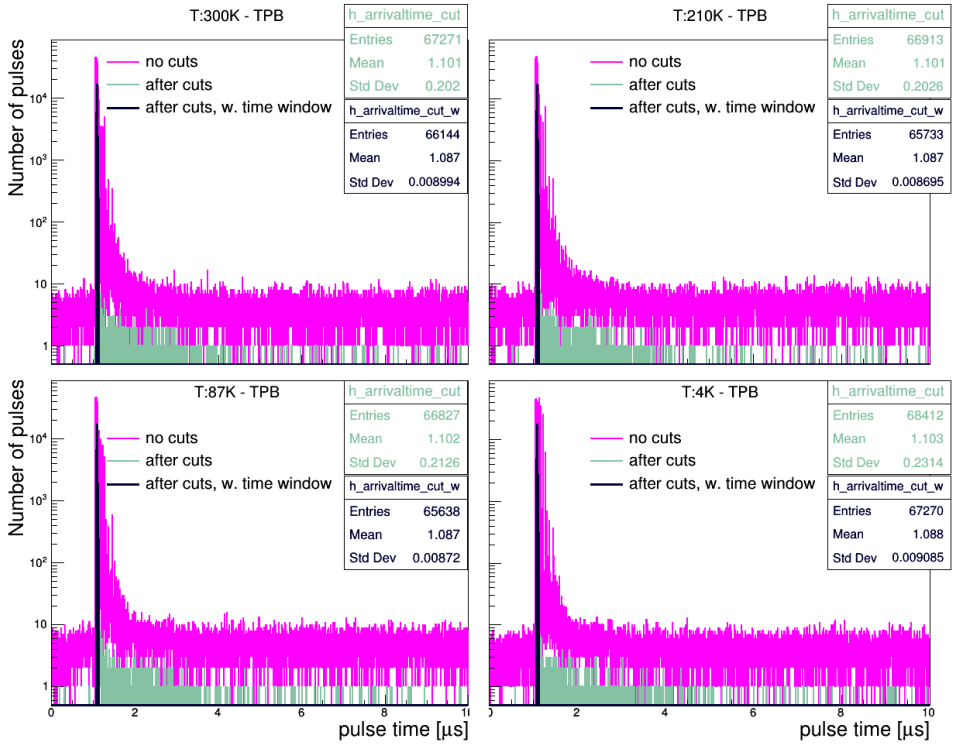

FIGURE B.5: Time distributions of the pulses detected in the measurements of TPB at 300 K, 210 K, 87 K and 4 K. All the pulses identified by the online analysis are show in magenta. In gray, only the ones that pass the cuts are shown. In black are the pulses after cuts and within the integration window (50ns after pre-trigger, from 1.07 to 1.12μs). They partially overlay the ones in gray.

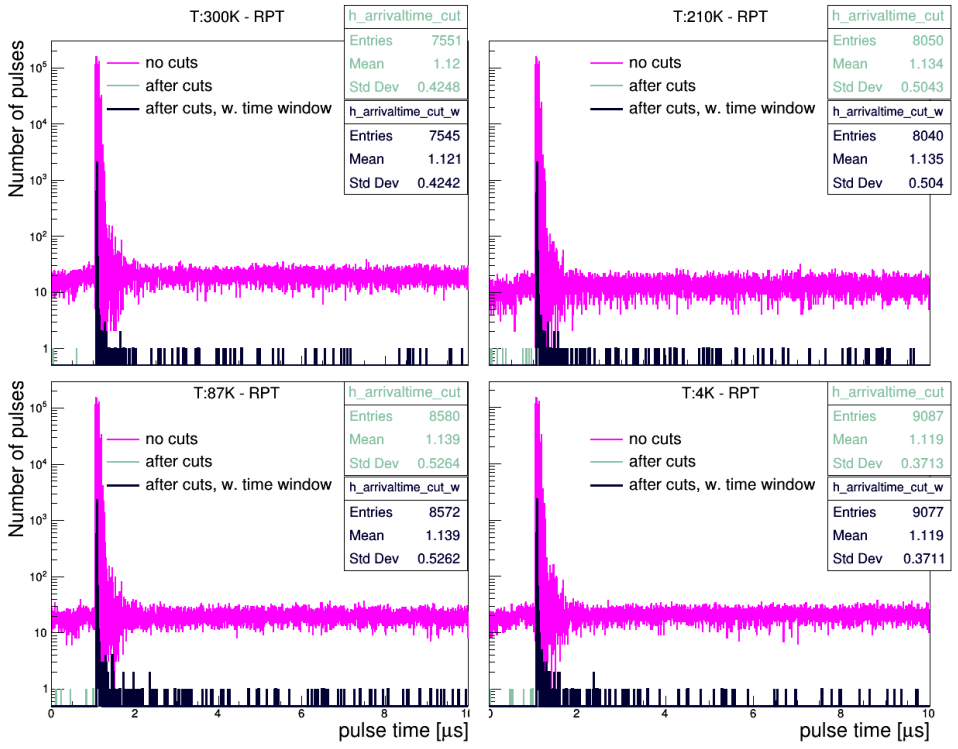

FIGURE B.6: Time distributions of the pulses detected in the measurements of RPT at 300 K, 210 K, 87 K and 4 K. Pulses before applying cuts in magenta and after cuts in gray. The pulses within the integration window are shown in black and partially overlay the ones in gray.

The average pulses (average light intensity as a function of time) of both RPT and TPB measured at 300 K, 210 K, 87 K and 4 K are shown in Figure B.7.

As discussed in Subsection 3.3.3, the amplitude of the average pulse of RPT increases in the first nanoseconds at lower temperatures. The parameters of the exponential fit of the average pulse of TPB measured at 87 K (Figure 3.11) are shown in Table B.1 and the fit function in (Equation B.1).

	parameter	value	error
first	p_0	181.34	0.07
exponential	p_1	-153.77	0.07
second	p_0	6.64	0.24
exponential	p_1	-1.43	0.13

TABLE B.1: Parameters of the exponential fit of the average pulse of TPB.

$$f(x) = exp(p_0 + p_1 * x) \tag{B.1}$$

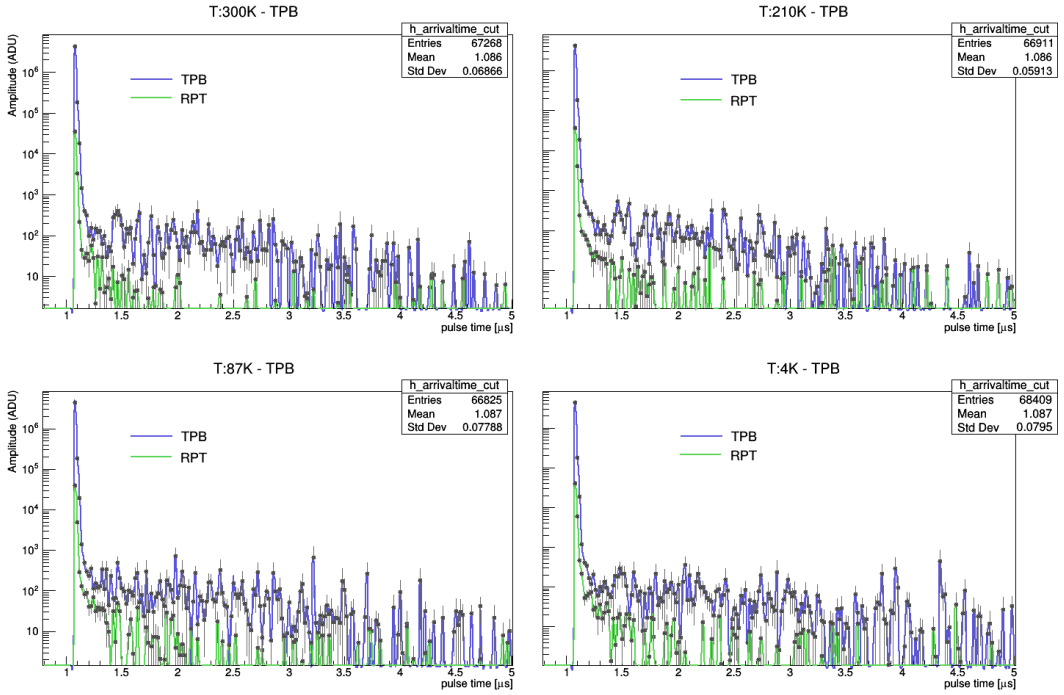

FIGURE B.7: Average pulses (after cuts) of TPB (blue) and RPT (green) measured at 300 K, 210 K, 87 K and 4 K.

Average pulses before and after cuts.

The average pulses of TPB and RPT are shown Figure B.8 before (dashed line) and after (solid line) cuts for 4 temperatures and for the first 300 ns after pretrigger. The effect of each cut on the average pulse of RPT is shown separately in Figure B.9.

As discussed in Subsection 3.3.1, the minimum pulse width requirement of 2 ns is able to cut the high amplitude noise around 1.05 µs (as shown in the left plot), but it is not able to cut the noise around 1.13 µs, which is then cut by the maximum amplitude threshold cut (shown on the right).

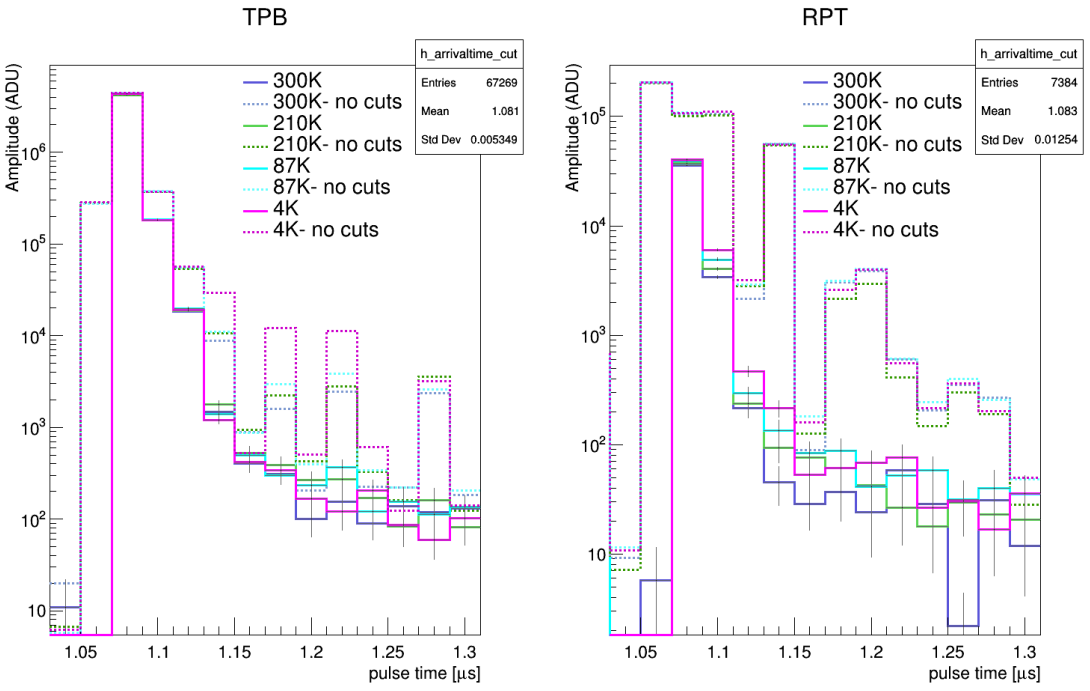

FIGURE B.8: Binned average pulses of TPB and RPT before (dashed line) and after (solid line) cuts measured at 300 K, 210 K, 87 K and 4 K.

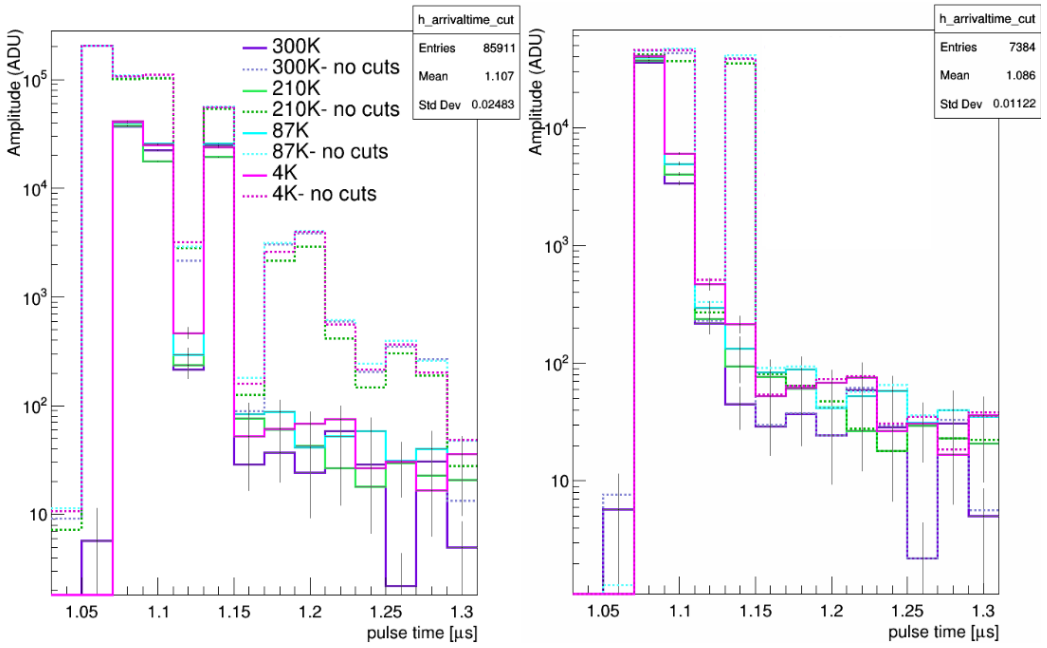

FIGURE B.9: Binned average pulse of RPT. In the left plot, the pulses are shown before cuts (dashed) and after pulse width cut (solid). In the plot on the right, the pulses are shown after pulse width cut, but before maximum amplitude cut (dashed) and after this cut (solid).

Appendix C

Appendix to the Chapter 5

C.1 Americium source characterization

Radioactivity measurements

The activity of this source was measured three times. Once with the FoPra germanium detector, once with the low background LoAx germanium detector and one more time with the same detector after encapsulation. The spectrum measured with the FoPra detector during a livetime of 88.8 s is shown in Figure C.1. Also shown are the background spectrum corrected for the livetime and the net spectrum corrected for the background.

In order to know the efficiency of this detector for the 59.54 keV gamma from Am-241, the calibration data of one previous measurement done with the same detector was used. In these calibration measurements, a Barium (Ba-133) and a Cobalt (Co-60) calibration sources were used. The spectrum of the Ba source is shown in Figure C.2. The gamma lines with energy 81 keV, 276.4 keV and 302.9 keV can be clearly seen in the net spectrum shown on the right. Of special interest is the 81 keV line. The efficiency was calculated for all the peaks of the Ba and Co sources that could be clearly seen in the spectra due to their higher branching ratios. The calibration efficiencies (not corrected for the geometry) are shown in figure Figure C.3.

Since the geometry of the measurement of the calibration sources and of the Am source was the same, no correction for the geometry was done. However, there is no calibration

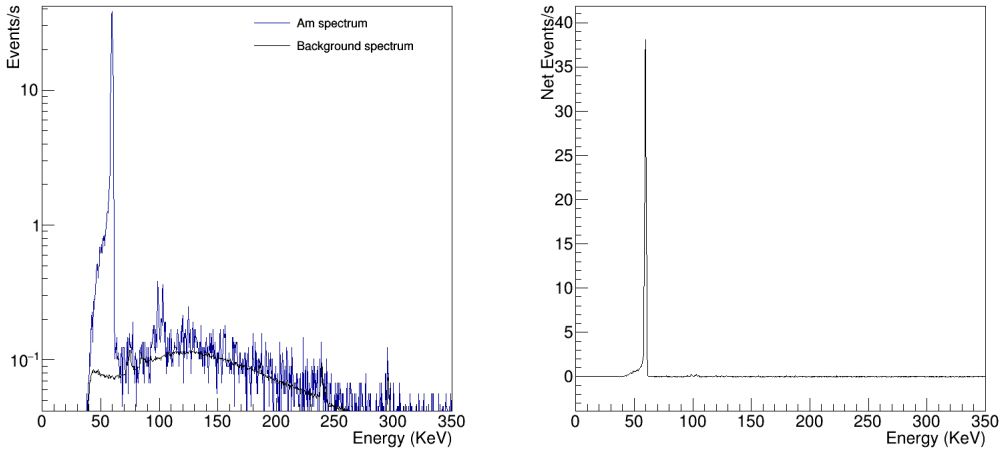

FIGURE C.1: Left: Spectrum of the Am-241 source measured by the FoPra germanium detector. Also shown is the background spectrum corrected for the livetime. Right: Net spectrum of the Am-241 source corrected for the background.

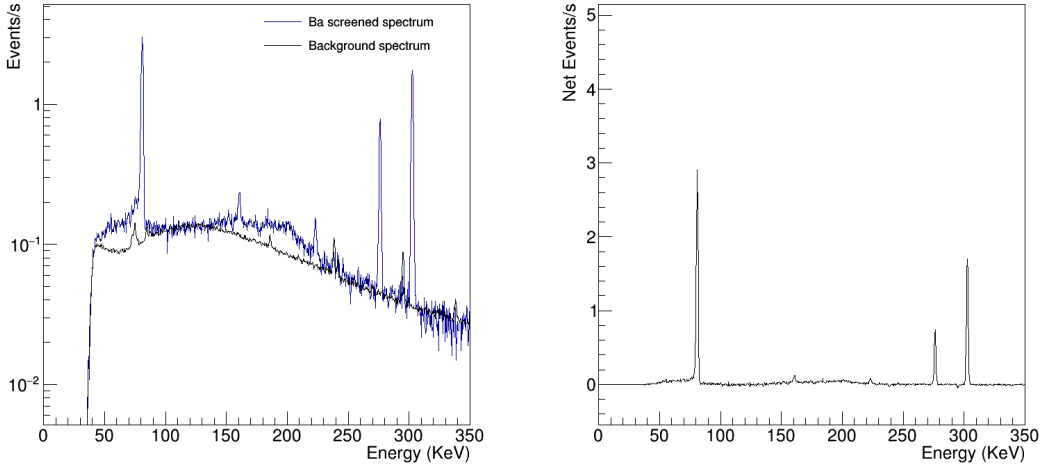

FIGURE C.2: Left: Spectrum of the Am-241 source measured by the FoPra germanium detector. Also shown is the background spectrum corrected for the livetime. Right: Net spectrum of the Am-241 source corrected for the background.

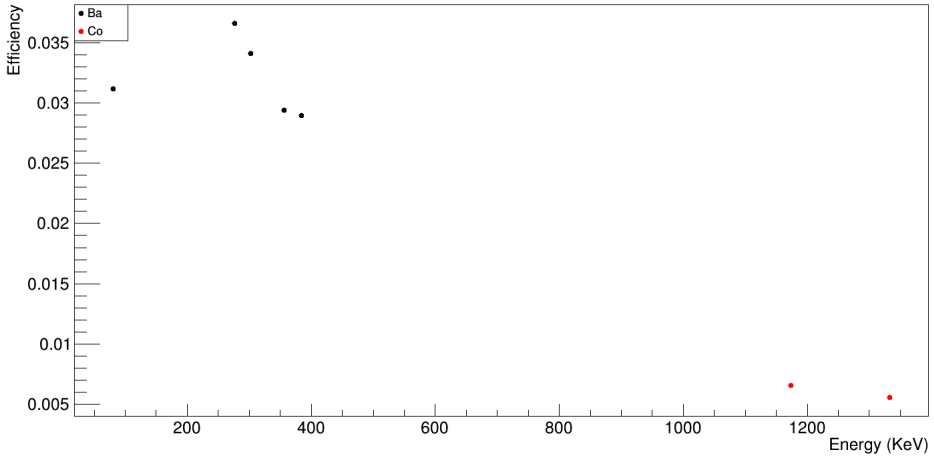

FIGURE C.3: Calibration Efficiency: Ratio between the detected and expected number of decays versus energy. This is valid for the geometry used to screen the calibration source.

data point at approx. 60 keV. The relation between efficiency and energy above approx. 200 keV is dominated by Compton scattering and can be fitted by an exponential. At lower energies outside the Compton dominated region, the efficiency is low due to the window of the germanium detector. As there is only one point at this region, no fit can be applied. I will therefore assume the same efficiency of the 81 keV gamma of the Barium calibration source and calculate an estimation of the activity of the Am-241 source. This results in the value of 16.56 kBq. This is probably an underestimated value, since the efficiency of the 59.54 keV gammas from Am-241 is lower than the efficiency of the 81 keV gamma from the Barium source. Furthermore, typical activities this source is 37 kBq [120].

We also measured the activity of this source with the low background LoAx germanium detector. This detector is also more suitable for this measurement, because its window is thinner than the one of the FoPra detector. The source was measured close and far from the detector. An Am-241 calibration source was also measured. The activity of this source is 347 kBq (measured in 2017). To avoid pile-up, the calibration source was measured in the far position. The far position measurements are compared and shown in Figure C.4.

The peaks were fitted, as shown in the insets of Figure C.4 and the integral of the fits were corrected for the background and then compared. This lead to the value of 24.28±0.11 kBq for the activity of the americium source. This value agrees with the underestimation of 16.56 kBq measured with the FoPra detector if the efficiency at 60 keV is 2.13% instead of 3.12%.

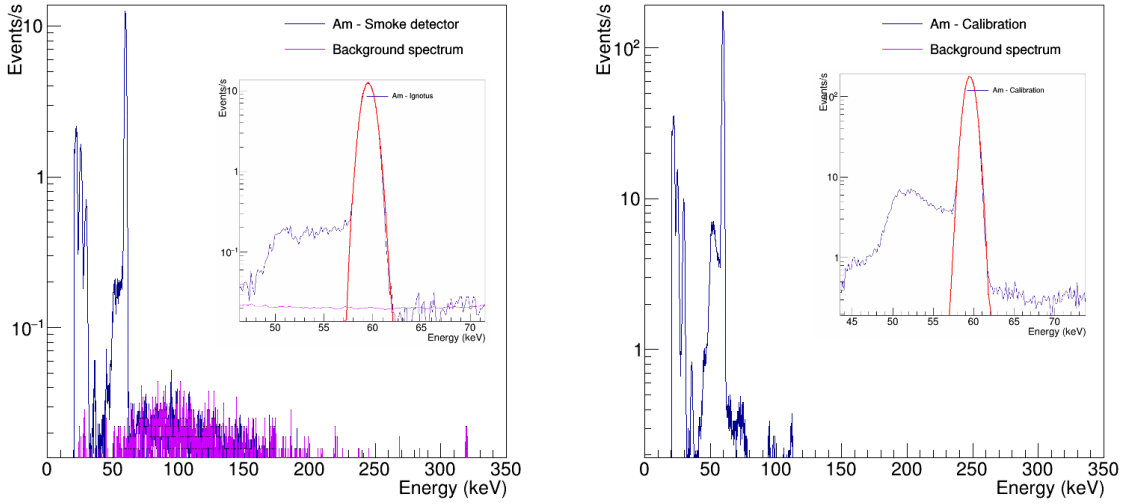

FIGURE C.4: Left: Spectrum of the Am-241 source measured by the LoAx germanium detector. Also shown is the background spectrum corrected for the livetime and the fit of the 59.54 keV peak in the inset. Right: Spectrum of the Am-241 source measured by the LoAx germanium detector. Fit of the 59.54 keV peak is shown in the inset. In this plot, the scale is 10x bigger and the background cannot be seen. Both sources were placed in the same position.

This value is also lower than the typical value of 37 kBq for this type of source [120]. This lower obtained value might be due self-absorption inside the source foil and surrounding material.

Attenuation of the 59.54 keV gamma in the LoAx entry window

We can also use the measurement of the calibration source, in order to estimate the attenuation of the entry window of the LoAx1 detector for a 60 keV gamma. The entrance window is a carbon fiber layer with a thickness of 1.06 mm [1]. Furthermore, there is a 0.3μm thick layer of boron. The distance between the far position and the window is 13 cm and the distance between the far position and the germanium detector is 13.5 cm. The radius of the germanium detector is 3.53 cm and the size of the source was taken to be 0.2 cm of radius and 0.5 cm thick. The solid angle correction is therefore 0.0185. Its geometry with relation to the detector is a very small cylinder shown in green in figure Figure C.5.

The detected rate is 1679 Hz. As the detection efficiency at this energy is dominated by the attenuation of the window, we can calculate the attenuation by dividing the rate of detected

[1] Information about the components and geometry of the detector was taken from the Geant4 simulation.

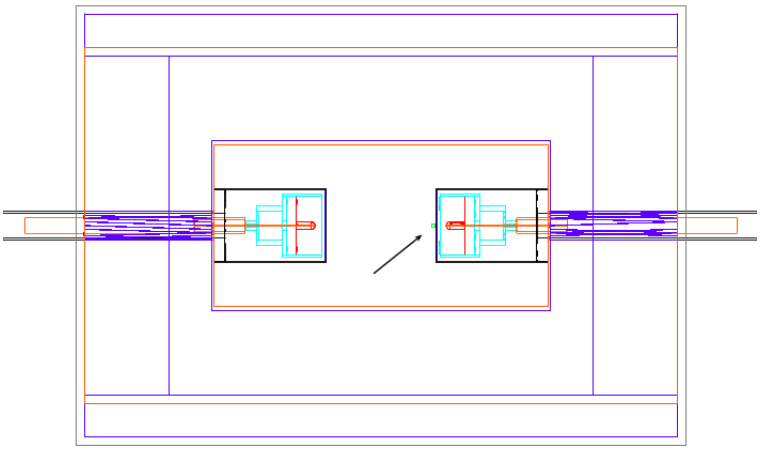

FIGURE C.5: Schematic of the LoAx Detector. The sample is a very small cylinder at the front of one detector and is shown in green, indicated by the arrow.

gammas by the activity of the source corrected for the solid angle factor and branching ratio. This leads to the value of 0.729±0.002. That is, approx. 27% of the 59.54 keV gammas are stopped by the window or do not fully deposit their energy in the germanium detector. A previous measurement of the detection efficiency of the LoAx1 detector for the 59.54 keV americium line had resulted in approx 31% efficiency [121] for the source placed 1 mm away from the top of the detector and not corrected for the solid angle. The correction of the value from [121] leads to an attenuation of 20%, which is similar to the value calculated above.

We can also use the measurement of the close non encapsulated source in order to cross-check the attenuation of the window at this energy. The distance between the close position and the window is negligible and the distance between the close position and the germanium detector is 0.5 cm. The solid angle correction is 0.43. the detected rate is 1593 Hz. The activity of the source was found to be 24.28±0.11 kBq by the far measurements. This leads to the value of 0.4249±0.0022 for the ratio of detected/expected number of counts. That is, approx. 58% of the gammas are stopped by the window or do not fully deposit their energy in the germanium detector. This value disagrees with the results presented in [121]. This could be due to uncertainties on the position of the source which leads to uncertainties in the solid angle correction. These uncertainties are more significant for the close measurement in comparison to the uncertainties of the far measurements.

Encapsulation of the source

In order to avoid contamination of the LAr in the cryostat by the source, the source was encapsulated with a thin layer of stainless steel. The source was measured again with the LoAx detector at the close and far positions. The spectra measured before and after the encapsulation of the source at the far position are shown in Figure C.6.

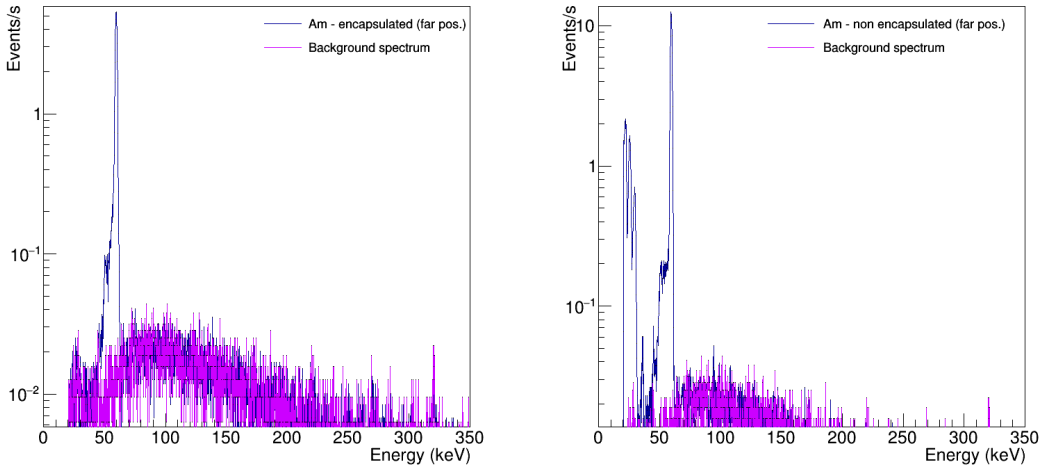

FIGURE C.6: Left: Spectrum of the Am-241 source measured with the LoAx germanium detector after encapsulation. Also shown in both plots is the background spectrum corrected for the livetime. Right: Spectrum of the Am-241 source measured with the LoAx germanium detector before encapsulation.

Both 59.54 keV peaks of the Figure C.6 are corrected for the background and integrated. The ratio of the integration values gives information about the attenuation of the gammas from the source by the encapsulation. The ratio for the far measurements is 0.4800±0.0032. That means that 52.00± 0.32% of the gammas are stopped by the stainless steel front window. The ratio of the close measurements is however lower, 0.4071±0.0015. This value means that, according to the close position measurement, 59.29±0.15% of the gammas are stopped by the front window of the encapsulation. Both spectra measured before and after the encapsulation of the source at the close position are shown in Figure C.7.

The disagreement between the measurements at close and far positions can be due to the fact that the encapsulation at the side part of the source is thicker and also due to the slightly further away positioning of the source in the close measurement, since the encapsulation is 1mm thick. The thickness of the stainless steel window can also be derived by the ratio

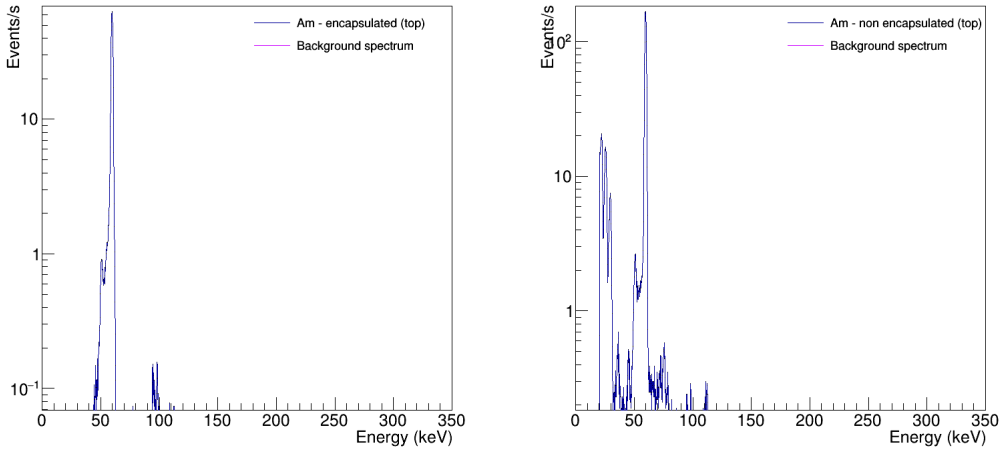

FIGURE C.7: Left: Spectrum of the Am-241 source measured with the LoAx germanium detector at close position after the encapsulation. Right: Spectrum of the Am-241 source measured with the LoAx germanium detector at close position before encapsulation. Background is very low in comparison to the signal and cannot be seen in the scale of the plot.

of intensities before and after encapsulation. We will calculate an approximation of it as a cross-check.

Estimation of the thickness of the stainless steel encapsulation layer

Stainless steel is composed mainly by iron, a minimum weight percentage of 10.5% of chromium and different amounts of carbon and in some cases molybdenum or nickel [122, 123]. We will consider here only the iron and chromium contents. The total attenuation length in stainless steel is calculated as shown in Equation C.1, which results from Equation 5.1.

$$\lambda_{att}^{total} = \frac{\lambda_{att}^{Fe} . \lambda_{att}^{Cr}}{\lambda_{att}^{Fe} + \lambda_{att}^{Cr}} \tag{C.1}$$

The attenuation lengths of a 59 keV gamma in Fe and Cr, λ_{att}^{Fe} and λ_{att}^{Cr}, are calculated as shown in Equation 5.2. The values of the mass attenuation coefficients for 59 keV are 1 cm^2/g in chromium and 1.26 cm^2/g in iron [116]. The density of stainless steel varies from 7.7 to 8 g/cm^3. We will use the value of 8 g/cm^3, which translates into 0.84 g/cm^3 of chromium and 7.16 g/cm^3 of iron. This leads to a total attenuation length of 1.014 mm. Now, we can use

Equation 5.1 to calculate the distance at which the intensity has dropped to 0.4800±0.0032 of its original value, as shown in Equation C.2.

$$\frac{I}{I_0} = e^{\frac{-d}{\lambda_{att}^{total}}} = 0.48 \tag{C.2}$$

Using this equation, we find the value of 0.744±0.007 mm for the thickness of the stainless steel front window. If we use the ratio given by the close measurement, it results in a thickness of 0.911±0.004mm. Therefore, both results are in good approximation to the nominal thickness of 1mm.

Event rate after encapsulation

The rate of the 59.54 keV gammas (main gamma emission) that exit the front window, R_{front}^{main} can be calculated by multiplying the activity of the source (corrected for the BR) before encapsulation by the fraction of gammas that go through the front window, as shown Equation C.3.

$$R_{front}^{main} = R_o \times BR_{main} \times F_{front} \times (1 - Att_{window}) \tag{C.3}$$

where R_o is the radioactivity of the source before encapsulation, BR_{main} is the branching ratio of the 59.54 keV gamma, F_{front} is the fraction of gammas that are emitted by the source in the direction of the front window and Att_{window} is the attenuation caused by the stainless steel front window, that is, the fraction of gammas stopped by the steel. The BR_{main} is 0.359 [124], F_{front} was taken to be equal to 0.5 and Att_{window} equal to 0.5929±0.0015. This results in a rate of 1.774±0.010 kHz. If we use the Att_{window} from the far measurement, this rate is 2.092±0.017 kHz. We will use this rate in order to calculate the pile-up probability, since it is more conservative

C.2 Active volume and threshold

To determine the optimal active volume and threshold, it is necessary to understand the minimum and maximum number of detected photons for the production of photons (gamma interaction) in different parts of the *AV*. This investigation is done in Figure C.8 to Figure C.11 for active volumes of radius ranging from 0.2 to 0.5 cm and number of detected photons calculated for the values of LY of 20 and 40 ph/keV.

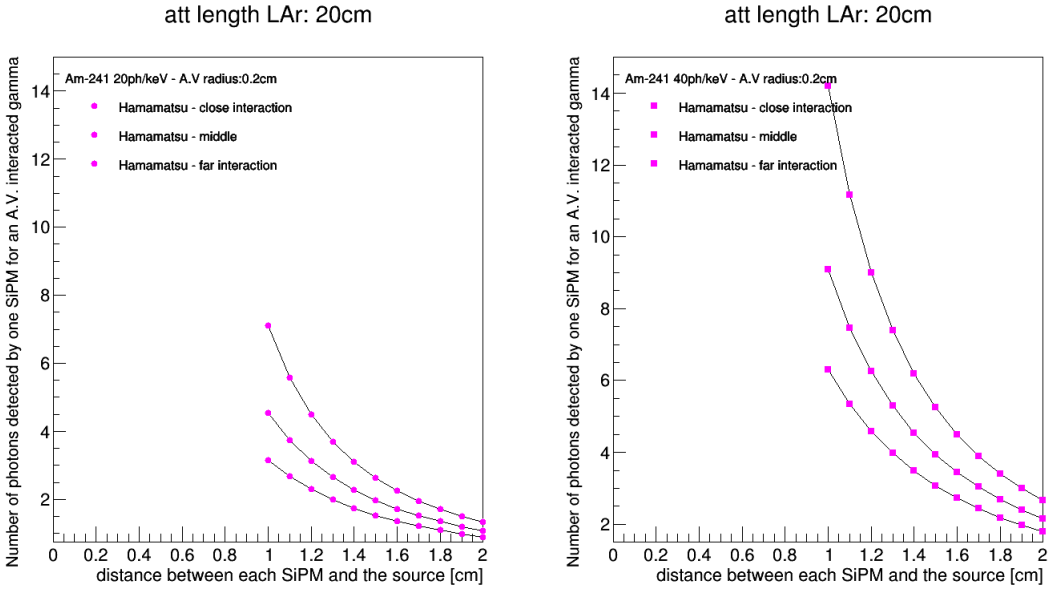

FIGURE C.8: Number of photons detected by one trigger SiPM for a gamma that interacted at the edges of the *AV* (close and far positions) and for a gamma that interacted at the center of the *AV*. The plot on the left shows these values for the LY in LAr equal to 20 ph/keV and the one on the right shows these values for LY=40ph/keV. The *AV* considered here has a radius of 0.2 cm.

The close interaction means that the gamma was emitted by the source in the direction of the SiPM and interacted at the edge of the *AV*. The far interaction means that the gamma was emitted in the opposite direction of the SiPM and interacted at the edge. The middle interaction means that the gamma interacted very close to the source, that is, at the center of the *AV*. These figures show that the minimum number of detected photons for a trigger SiPM placed 1 cm from the source and an *AV* radius of 0.5 cm is two. Therefore, for a 1 cm distant trigger SiPM, the minimum threshold of 2 photons can be set. Note that for an active volume of 0.2 cm radius a value of 3 photons could be set as threshold. As the *AV* of radius 0.5 cm is the one with the highest mean number of detected photons and still allows for the

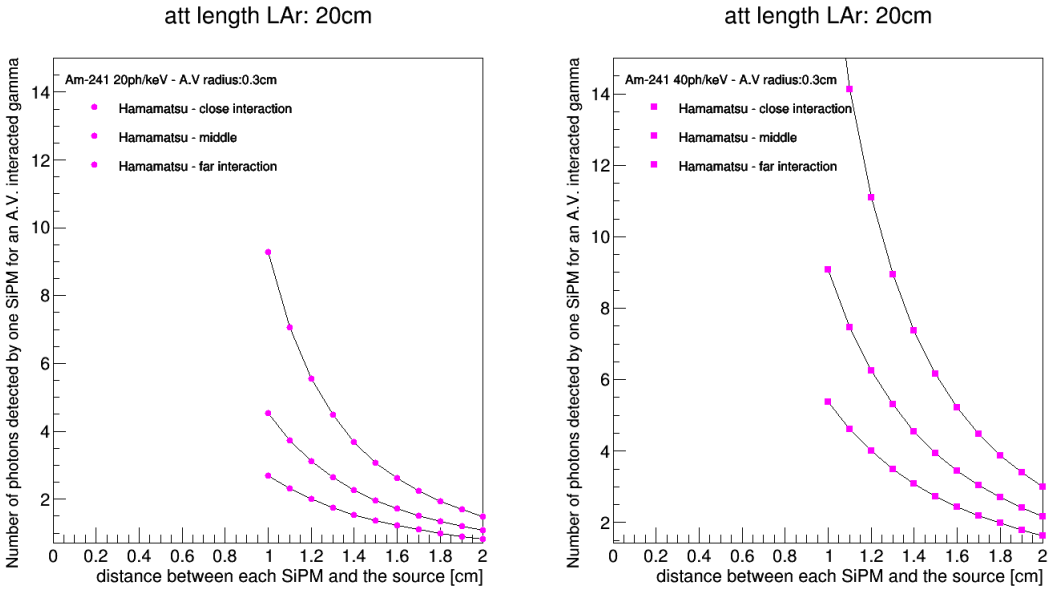

FIGURE C.9: Number of photons detected by one trigger SiPM for a gamma that interacted at the edges of the AV (close and far positions) and for a gamma that interacted at the center of the AV. The plot on the left shows these values for the LY in LAr equal to 20 ph/keV and the one on the right shows these values for LY=40ph/keV. The AV considered here has a radius of 0.3cm.

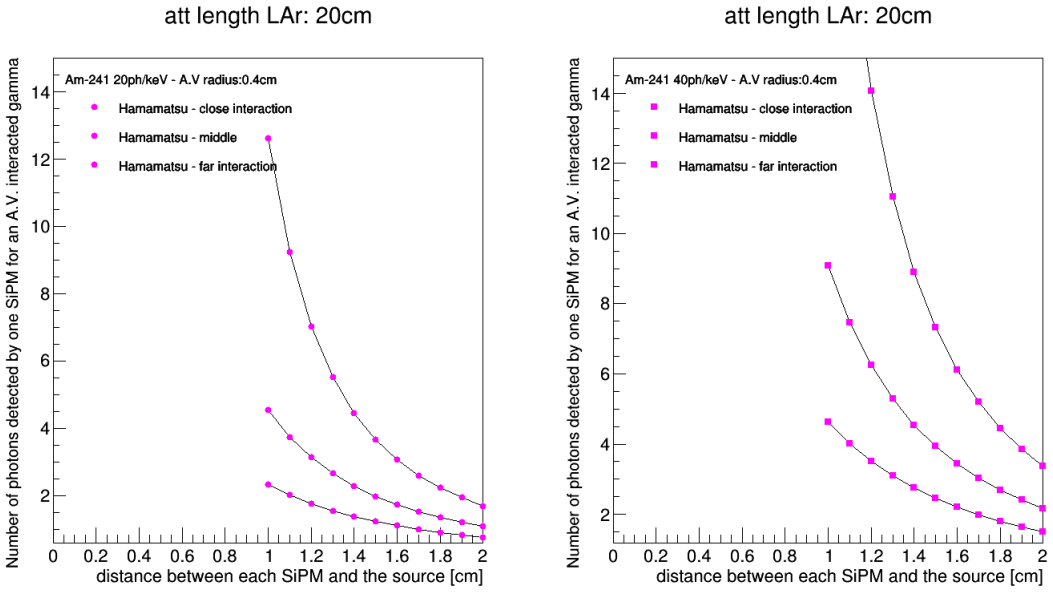

FIGURE C.10: Number of photons detected by one trigger SiPM for a gamma that interacted at the edges of the AV (close and far positions) and for a gamma that interacted at the center of the AV. The plot on the left shows these values for the LY in LAr equal to 20 ph/keV and the one on the right shows these values for LY=40ph/keV. The AV considered here has a radius of 0.4 cm.

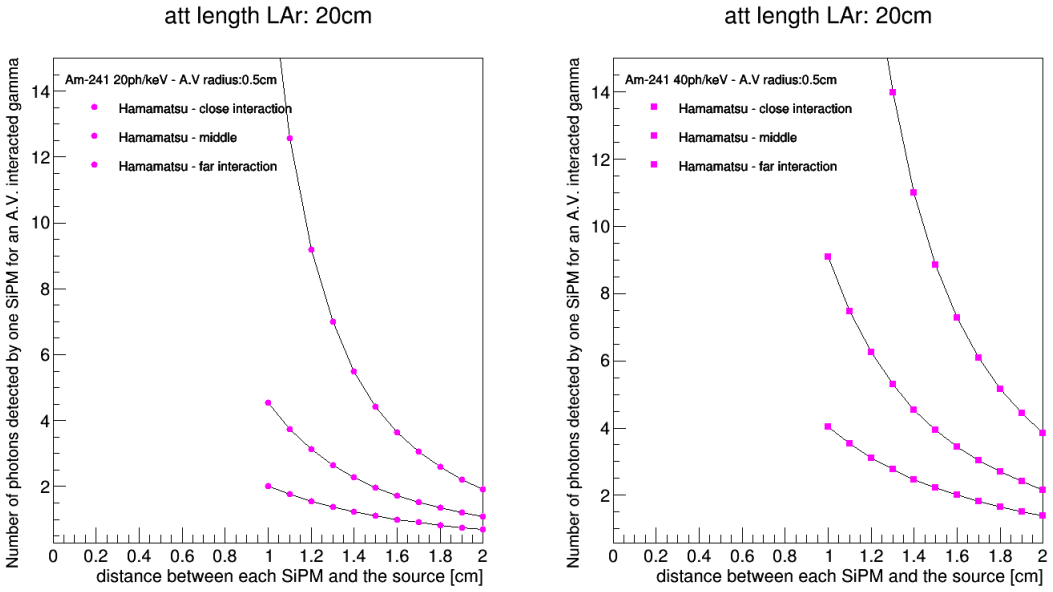

FIGURE C.11: Number of photons detected by one trigger SiPM for a gamma that interacted at the edges of the AV (close and far positions) and for a gamma that interacted at the center of the AV. The plot on the left shows these values for the LY in LAr equal to 20 ph/keV and the one on the right shows these values for LY=40ph/keV. The AV considered here has a radius of 0.5 cm.

detection of 2 photons in the far interaction position with relation to the SiPM, this will be considered as the optimal radius of the AV.

C.3 Next Steps

A more sophisticated 3D simulation is necessary for a better estimation of the relation between the attenuation length and the number of detected photons. This simulation, should also take into account: i) the reflectivity of the cryostat, ii) the geometry of the far SiPM arrays and iii) The effect of dark rate and background on the measurements. This simulation could provide a better estimation of the number of photons detected by the SiPMs. It is also necessary to determine the total charge and charge distribution pattern for the chosen AV and to check the probability that an event that does not happen in the AV is tagged as an event within the AV.

Bibliography

[1] P. A. Oesch et al. A remarkably luminous galaxy at z = 11.1 measured with Hubble space telescope Grism spectroscopy. *The Astrophysical Journal. 819 (2):129*, 2016. arXiv:1603.00461.

[2] Archive of the Nasa website (accessed in 2018). asd.gsfc.nasa.gov/archive.

[3] The IceCube Collaboration. Neutrino emission from the direction of the blazar TXS 0506+056 prior to the IceCube-170922A alert. *Science: Vol. 361, Issue 6398, pp. 147-151*, 2018.

[4] The IceCube Collaboration. Evidence for high-energy extraterrestrial neutrinos at the IceCube detector. *Science: Vol. 342, Issue 6161, 1242856*, 2013.

[5] R. Bernabei et al. Final model independent result of DAMA/LIBRA-phase1. *Eur. Phys. J. C 73 2648*, 2013. arXiv:1308.5109.

[6] The COSINE-100 Collaboration. An experiment to search for dark-matter interactions using sodium iodide detectors. *Nature volume 564, pages 83-86*, 2018.

[7] Periodic table website (accessed in 2018):. periodictable.com/Items/080.20/index.html.

[8] B Broerman; M.G. Boulay; T.Pollmann et. al. Application of the TPB Wavelength Shifter to the DEAP-3600 Spherical Acrylic Vessel Inner Surface. *Journal of Instrumentation, V. 12*, 2017. arXiv:1704.01882.

[9] Garry W. Angus et al. Can MOND take a bullet? Analytical comparisons of three versions of MOND beyond spherical symmetry. *Mon. Not. Roy .Astron. Soc. 371:138*, 2006. arXiv:astro-ph/0606216v1.

[10] Douglas Clowe et al. Weak lensing mass reconstruction of the interacting cluster 1E0657-558: Direct evidence for the existence of dark matter. *Astrophys. J. 604:596-603*, 2004. arXiv:astro-ph/0312273.

[11] M. Markevitch et al. Direct constraints on the dark matter self-interaction cross-section from the merging galaxy cluster 1E0657-56. *Astrophys. J. 606:819-824*, 2004. arXiv:astro-ph/0309303.

[12] Sibel Boan et al. GW170817 falsifies dark matter emulators. *Phys. Rev. D 97, 041501*, 2018. arXiv:1710.06168.

[13] P. Tisserand et al. Limits on the Macho content of the galactic halo from the EROS-2 survey of the magellanic clouds. *Astron. Astrophys. 469:387-404*, 2007. arXiv:0607207.

[14] Simeon Bird et al. Did LIGO detect dark matter? *Phys. Rev. Lett. 116, 201301*, 2016. arXiv:1603.00464.

[15] Miguel Zumalacarregui and Uros Seljak. Limits on stellar-mass compact objects as dark matter from gravitational lensing of type Ia supernovae. *Phys. Rev. Lett. 121, 141101*, 2018. arXiv:1712.02240.

[16] Juan Garcia-Bellido et al. LIGO lo(g)normal MACHO: Primordial black holes survive SN lensing constraints. *CERN-TH-2017-271, IFT-UAM/CSIC-17-123*, 2017. arXiv:1712.06574.

[17] E.-K. Park. Contribution to the report on the direct detection and study of dark matter, page 59, 2007. from the High Energy Physics Advisory Panel's website (accessed in 2018). science.energy.gov/hep/hepap/reports/.

[18] Esra Bulbul et al. Detection of an unidentified emission line in the stacked x-ray spectrum of galaxy clusters. *The American Astronomical Society*, 2014. arXiv:1402.2301.

[19] Kaixuan Ni. Recent results from dark matter direct detection experiments. Talk presented at CIPANP - Thirteenth Conference on the Intersections of Particle and Nuclear Physics, 2018. conferences.lbl.gov/event/137/.

[20] P. Agnes et al. (The DarkSide Collaboration). Low-mass dark matter search with the DarkSide-50 experiment. *Phys. Rev. Lett. 121, 081307*, 2018. arXiv:1802.06994.

[21] P. Agnes et al. (The DarkSide Collaboration). Constraints on Sub-GeV Dark Matter-Electron Scattering from the DarkSide-50 Experiment. *Phys. Rev. Lett. 121, 111303*, 2018. arXiv:1802.06998.

[22] M. Kobayashi et al. (The XMASS Collaboration). Search for sub-GeV dark matter by annual modulation using XMASS-I detector. 2018. arXiv:1808.06177.

[23] K. M. Zurek. Asymmetric dark matter: Theories, signatures, and constraints. *Invited Review for Physics Reports*, 2013. arxiv:1308.0338.

[24] Alexander Kusenko and Mikhail Shaposhnikov. Supersymmetric Q-balls as dark matter. *Physics Letters B 418:46-54*, 1998. arxiv:9709492.

[25] Edward W. Kolb and Andrew J. Long. Superheavy dark matter through higgs portal operators. *Phys. Rev. D 96, 103540*, 2017. arxiv:1708.04293.

[26] List of neutrino experiments - neutrino unbound website (accessed in 2019). nu.to.infn.it/exp/.

[27] The Borexino collaboration. Comprehensive measurement of pp-chain solar neutrinos. *Nature volume 562, pages 505-510*, 2018. doi:10.1038/s41586-018-0624-y.

[28] S. Andringa et al. (SNO+ Collaboration). Current status and future prospects of the SNO+ Experiment. *Advances in High Energy Physics, article ID 6194250*, 2016. DOI:10.1155/2016/6194250.

[29] Agnese Giaz. Status and perspectives of the JUNO experiment. 2018. arXiv:1804.03575.

[30] The IceCube Collaboration. The IceCube Data Acquisition System: signal capture, digitization, and timestamping. *Nucl. Instrum. Meth. A 601:294-316*, 2009. arXiv:0810.4930.

[31] DUNE Collaboration: R. Acciarri et al. Long-baseline neutrino facility (LBNF) and Deep Underground Neutrino Experiment (DUNE) conceptual design report v. 2: The physics program for DUNE at LBNF. 2015. arXiv:1512.06148v2.

[32] D. Akimov et al. Observation of coherent elastic neutrino-nucleus scattering. *Science 03 Aug*, 2017. DOI: 10.1126/science.aao0990 .

[33] Pietro Antonioli et al. SNEWS: the supernova early warning system. *New Journal of Physics, Volume 6*, 2004.

[34] D. D. Stancil et al. Demonstration of communication using neutrinos. *Mod. Phys. Lett. A 27 1250077*, 2012. arxiv:1203.2847.

[35] M. Agostini et al. (GERDA collaboration). Background free search for neutrinoless double beta decay with GERDA Phase II. *Nature, Volume 544, Number 7648, pp5-132*, 2017. arxiv:1703.00570.

[36] Teresa Marrodan Undagoitia and Ludwig Rauch. Dark matter direct-detection experiments. 2017. arXiv:1509.08767.

[37] The ArDM (argon dark matter) Experiment website. section: Scintillation and ionisation detection methods (accessed in 2018). darkmatter.ethz.ch/.

[38] Doke et al. Absolute scintillation yields in liquid argon and xenon for various particles. *Jpn. J. Appl. Phys. 41 1538*, 2002.

[39] WARP collaboration. First results from a dark matter search with liquid argon at 87 K in the Gran Sasso Underground Laboratory. *Astr. Phys 28, 495*, 2008.

[40] Davide Franco. DarkSide-50. Talk given in Planck 2014.

[41] P. Agnes et al. (the DarkSide collaboration). DarkSide-50 532-day dark matter search with low-radioactivity argon. *Phys. Rev. D 98, 102006*, 2018. arXiv:1802.07198.

[42] M. Hoffman et al. Ion-beam excitation of liquid argon. *Eur. Phys. J. C*, 2013. arXiv:1511.07721.

[43] J.Calvo et al. Measurement of the attenuation length of argon scintillation light in the ArDM LAr TPC. *Prepared for submission to JCAP*. arXiv:1611.02481v1 .

[44] N. Ishida et al. Attenuation length measurements of scintillation light in liquid rare gases and their mixtures using an improved reflection suppresser. *Nuclear Instruments and Methods in Physics Research A 384, p.380-386*, 1997.

[45] A. Neumeier et al. Attenuation of vacuum ultraviolet light in pure and xenon-doped liquid argon - an approach to an assignment of the near-infrared emission from the mixture. *EPL (2015)*. arXiv:1511.07725.

[46] P. Benetti et al. Measurement of the specific activity of Ar-39 in natural argon. *Nuclear Instruments and Methods in Physics Research Section A: Accelerators, Spectrometers, Detectors and Associated Equipment 574 (1) 83-88*, 2007. arXiv:astro-ph/060313.

[47] J. Xu et al. A study of the residual 39Ar content in argon from underground sources. *Astroparticle Physics, Volume 66, p. 53-60*, 2015. arXiv:1204.6011.

[48] ArDM Collaboration. The ArDM Liquid Argon Time Projection Chamber at the Canfranc Underground Laboratory: a ton-scale detector for Dark Matter Searches. 2016. arXiv:1612.06375.

[49] R. Ajaj et al. (DEAP collaboration). Search for dark matter with a 231-day exposure of liquid argon using DEAP-3600 at SNOLAB. 2019. arXiv:1902.04048.

[50] R. Acciarri et al. (MicroBooNE Collaboration). Design and construction of the MicroBooNE detector. arXiv:1612.05824.

[51] JuiJen (Ryan)Wang. MiniCLEAN Dark Matter Experiment. *Doctor thesis*, 2018. arXiv:1711.02117.

[52] B. Abi et al. (ProtoDUNE collaboration). The single-phase ProtoDUNE technical design report. 2017. arXiv:1706.07081.

[53] T.Bode et al. Optical fiber read-out for liquid argon scintillation light. 2016. arXiv:1606.04254 .

[54] C. Benson et al. Measurements of the intrinsic quantum efficiency and absorption length of tetraphenyl butadiene thin films in the vacuum ultraviolet regime. *Eur. Phys. J. C 78:329*, 2018. arXiv:1709.05002v2.

[55] C.H. Lally et al. UV quantum efficiencies of organic fluors. *Nuclear Instruments and Methods in Physics Research B 117 421-427*, 1996.

[56] Alexander Neumeier. Optical properties of liquid noble gas scintillators. *Doctor thesis*, 2015.

[57] Carlos H. Faham. Prototype, surface commissioning and photomultiplier tube characterization for the large underground xenon (LUX) direct dark matter search experiment. *Doctor Thesis*, 2014.

[58] P.A. Amaudruz et al. (DEAP collaboration). Design and construction of the DEAP-3600 dark matter detector. *submitted to Astroparticle Physics*, 2018. arXiv:1712.01982.

[59] DEAP collaboration archive.

[60] Ocean optics datasheet.

[61] B. Majorovits et al. PEN as self-vetoing structural material. *AIP Conference Proceedings 1921, 090001 (2018)*. doi: 10.1063/1.5019011.

[62] K. Boudjemline et al. The calibration of the Sudbury Neutrino Observatory using uniformly distributed radioactive sources. *Nuclear Instruments and Methods A620:171-181*, 2010. arXiv:0912.2991.

[63] Wang YuanQing et al. Application of an acrylic vessel supported by a stainless-steel truss for the JUNO central detector. *Science China Technological sciences. Vol.57 No.12: 2523-2529*, 2014.

[64] LUX Collaboration. Calibration, event reconstruction, data analysis, and limit calculation for the LUX dark matter experiment. *Phys.Rev. D97 (2018) no.10 102008.* arXiv:1712.05696.

[65] E. Aprile et al. (Xenon Collaboration). Physics reach of the XENON1T dark matter experiment. *JCAP04(2016)027*, 2016. arXiv:1512.07501.

[66] Aigars Piruska et al. The autofluorescence of plastic materials and chips measured under laser irradiation. *Lab Chip, 5, 1348-1354*, 2005. DOI:10.1039/b508288a.

[67] Kenneth R. Hawkins and Paul Yager. Nonlinear decrease of background fluorescence in polymer thin-films - a survey of materials and how they can complicate fluorescence detection in mtas. *Lab Chip, 2003, 3, 248-252.* DOI:10.1039/b307772c.

[68] Shawn D. Llopis; Wieslaw Stryjewski and Steven A. Soper. Near-infrared time-resolved fluorescence lifetime determinations in poly(methylmethacrylate) microchip electrophoresis devices. *Electrophoresis 2004, 25, 3810-3819.* DOI:10.1002/elps.200406054.

[69] Hidetoshi Miyashita et al. Autofluorescence of electrophoresis chip grooved by excimer laser. *JLMN-Journal of Laser Micro/Nanoengineering Vol.3, No.2, 2008.*

[70] Travis D. Boone et al. Plastic advances - microfluid devices. *Analytical Chemistry, February, 2002.*

[71] Bo Lu et al. A study of the autofluorescence of parylene materials for mtas applications. *Lab Chip, 2010, 10, 1826-1834.* DOI:10.1039/b924855b.

[72] Hamed Shadpour et al. Physiochemical properties of various polymer substrates and their effects on microchip electrophoresis performance. *Journal of Chromatography A, 1111 (2006) 238-251.*

[73] Yann Molard et. al. Red-NIR Luminescent Hybrid Poly(methyl methacrylate) Containing Covalently Linked Octahedral Rhenium Metallic Clusters. *Chem. Eur. J. 2010, 16, 5613 - 5619.*

[74] W.E. Graves et al. Temperature dependence of phosphorescence characteristics of aromatic hydrocarbons in poly(methylmethacrylate). *The Journal of Chemical Physics 56, 1309*, 1972. DOI:10.1063/1.1677363.

[75] Victor F. Tarasenko et al. Luminescence of polymethyl methacrylate excited by a runaway electron beam and by a KrCl excilamp. *IEEE Transactions in Plasma Science, Vol. 45, N.1*, 2017.

[76] Tsung-Yao Chang et al. Fully automated cellular-resolution vertebrate screening platform with parallel animal processing. *Lab Chip. 2012 February 21; 12(4): 711-716.* DOI:10.1039/c1lc20849g.

[77] V.F. Gachkovskii et al. Dependence of the fluorescence intensity of polytetrafluoroethylene on the conditions of synthesis and molecular weight. *Sertya Khimieheskmra, No. 11, pp. 2453-2456, November*, 1968.

[78] Ping-Shine Shaw et al. Measurement of the ultraviolet-induced fluorescence yield from integrating spheres. *Metrologia 46 S191*, 2009. DOI:10.1088/0026-1394/46/4/S11.

[79] Ping-Shine Shaw et al. Ultraviolet characterization of integrating spheres. *Applied Optics*, 2007. DOI:10.1364/AO.46.005119.

[80] A. Charles and R.G. Partidge. The identification of luminescent centres in polyethylene and other polymeters. 1964.

[81] E. Peik. Long-lasting photoluminescence in polymers. *Journal of Physics D: Applied Physics, Volume 40, Number 11*, 2007.

[82] Frank Barkusky et al. Direct structuring of solids by EUV radiation from a table-top laser produced plasma source. *Proc. of SPIE Vol. 7361 73610D-1.*

[83] Advanced Optics SCHOTT AG. Tie-36: Fluorescence of optical glass. 2010.

[84] Xinjie Fu et al. Radiation induced color centers in silica glasses of different oh content. *Nuclear Instruments and Methods in Physics Research Section B: Beam Interactions with Materials and Atoms. Volume 330, 1 July 2014, Pages 7-10.* DOI:10.1016/j.nimb.2014.03.011.

[85] Ricardo Elgul Samad et al. Production of color centers in PMMA by ultrashort laser pulses. *Radiation Physics and Chemistry 79 (2010) 355-357.*

[86] F. Neves et al. Measurement of the absolute reflectance of polytetrafluoroethylene (PTFE) immersed in liquid xenon. 2016. arXiv:1612.07965.

[87] P. Sorensen and K. Kamdin. Two distinct components of the delayed single electron background signals in liquid xenon emission detectors. *2018 JINST 13 P02032.* arXiv:1711.07025.

[88] Private communication with LUX collaborator Francisco Neves.

[89] Peter Sperfeld et al. Analysis and reduction of fluorescence on PTFE-coated integrating spheres. *Poster presented at NEWRAD - the 11th International Conference on New Developments and Applications in Optical Radiometry*, 2011.

[90] V. N. Rai et al. Optical properties (UV-Vis AND FTIR) of gamma irradiated polymethyl methacrylate (PMMA).

[91] Renhua Na et al. Autofluorescence spectrum of skin: component bands and body site variations. *Skin Research and Technology 2000; 6: 112-117.* Copyright C Munksgaard 2000.

[92] Ocean Optics QE65000 data sheet.

[93] M. R. Sharpe and D. Irish. Stray light in diffraction grating monochromators. *Optica Acta: International Journal of Optics, 25:9, 861-893*, 1978. DOI: 10.1080/713819858.

[94] N. Anderson and T. Erdogan. Spectral modelling in fluorescence microscopy. *Semrock white papers series.*

[95] Turan Erdogan et al. Optical filters impact fluorescence fidelity. *BioPhotonics*, 2003.

[96] Brasseur G. and Jacob D. Formulations of radiative, chemical, and aerosol rates. *Cambridge: Cambridge University Press. p. 205-252*, 2017. doi:10.1017/9781316544754.006.

[97] Private communication with professor Jean-Franois Gal from University of Nice Sophia Antipolis.

[98] P.C.F. Di Stefano et al. Counting photons at low temperature with a streaming time to digital converter. *Nucl. Instr. Meth. Phys. Res. A, vol 700, pp 40-52*, 2013.

[99] M. Clark et al. Particle detection at cryogenic temperatures with undoped CsI. *Nuclear Inst. and Methods in Physics Research, A 901 6-13*, 2018. "arXiv:1709.04020".

[100] Hamamatsu R6095 Bialkali Photocathode datasheet.

[101] J.S. Kaputinsky et al. A fast timing light pulser for scintillation detectors. *Nuclear Instruments and Methods in Physics Research A241 612-613*, 1985.

[102] J .M . Flournoy et al. Substituted tetraphenylbutadienes as fast scintillator solutes. *Nuclear Instruments and Methods in Physics Research A 351, 349-35*, 1994.

[103] E. Segreto. Evidence of delayed light emission of tetraphenyl-butadiene excited by liquid-argon scintillation light. *Physical Review C 91, 035503*, 2015.

[104] R. Francini et al. VUV-Vis optical characterization of tetraphenyl-butadiene films on glass and specular reflector substrates from room to liquid argon temperature. *2013 JINST 8 P09006.*

[105] H. Nakamura et al. Evidence of deep-blue photon emission at high efficiency by common plastic. *EPL (Europhysics Letters), Volume 95, Number 2*, 2011.

[106] CUORE collaboration. The projected background for the CUORE experiment. *Eur. Phys. J. C 77:543*, 2017. arXiv:1704.08970.

[107] M. Kuzniak et al. Polyethylene naphthalate film as a wavelength shifter in liquid argon detectors. *Preprint submitted to Eur. Phys. J. C. DOI: 10.1140/epjc/s10052-019-6810-8*, 2019. arXiv:1806.04020v2.

[108] I. Ouchi et al. Features of fluorescence spectra of Polyethylene 2,6-Naphthalate films. *Journal of Applied Polymer Science, Vol. 105, 114-121*, 2007.

[109] D. Mary et al. Understanding optical emissions from electrically stressed insulating polymers: electroluminescence in poly(ethylene terephthalate) and poly(ethylene 2,6-naphthalate) films. *J. Phys. D: Appl. Phys. 30 171-184*, 1997.

[110] V.M. Gehman et al. Fluorescence efficiency and visible re-emission spectrum of tetraphenyl butadiene films at extreme ultraviolet wavelengths. *Nucl. Instrum. Methods A 654, 116-1211*, 2011. arXiv:1104.3259v2.

[111] D.N.McKinsey et al. Fluorescence efficiencies of thin scintillating films in the extreme ultraviolet spectral region. *Nucl. Instrum. Methods B, Volume 132, Issue 3, Pages 351-358A 654, 116-1211*, 1997.

[112] D. Mary et al. UV-induced degradation of poly(ethy1ene naphthalate) films from the standpoint of electrical and luminescence properties. *Annual Report Conference on Electrical Insulation and Dielectric Phenomena*, 2001.

[113] A. Neumeier et al. Attenuation of vacuum ultraviolet light in liquid argon. *Eur. Phys. J. C*, 2012. arXiv:1511.07724v1.

[114] Birgit Schneider. Analysis of the light attenuation measurement in liquid argon in the GERDA cryostat. *International School of Nuclear Physics - September 2017.*

[115] ASTAR website: Stopping power and range tables for alpha particles (accessed in 2018). physics.nist.gov/PhysRefData/Star/Text/ASTAR.html.

[116] NIST website: Attenuation coefficients and scattering table (accessed in 2018). physics.nist.gov/PhysRefData/FFast/html/form.html.

[117] R.B. Firestone et al. 8th edition of the table of isotopes: 1999 update (accessed in 2018). application.wiley-vch.de.

[118] C. E. Aalseth (DarkSide 20k Collaboration). DarkSide-20k: a 20 tonne two-phase LAr TPC for direct dark matter detection at LNGS. *Eur. Phys. J. Plus 133: 131*, 2017. arXiv:1707.08145.

[119] J Aalbers et al. (Xenon Collaboration). DARWIN: towards the ultimate dark matter detector. *JCAP 1611 (2016) no.11*, 2017. arXiv:1606.07001.

[120] Eric Eason. Americium smoke detectors. from stanford.edu website (acessed in 2018). *Submitted as coursework for Physics 241, Stanford University, Winter 2011.* large.stanford.edu/courses/2011/ph241/eason1/.

[121] T. Mannel. Low-level radioactivity techniques for the neutrino-oscillation experiment double chooz. *Master Thesis, Technical University of Munich*, November, 2013.

[122] The stainless steel family. ISSF - International Stainless Steel Forum. website accessed in 2018. www.worldstainless.org.

[123] Stainless steel analysis: Material interface website (accessed in 2018). materialinterface.com/stainless-steel-analysis/.

[124] Table of radioactive isotopes from the nuclear data website (accessed in 2018). nucleardata.nuclear.lu.se.